Commissioning of the LHCb VELO Detector and the Performance of Irradiated VELO Sensors in a Proton Testbeam

Abdirizack Noor
University of Liverpool

Thesis submitted in accordance with the requirements of The University of Liverpool for the degree of Doctor of Philosophy

Abstract

The Large Hadron Collider (LHC) is a proton proton collider at the European Organisation for Nuclear Research (CERN). The LHCb experiment is one of four experiments at the LHC. It will exploit the copious amounts of $b\overline{b}$ pairs produced to make precision measurements of the properties of B-mesons. The real time identification of B-mesons is provided by the Vertex Locator (VELO), which is a silicon microstrip tracking and vertexing detector at the LHCb experiment.

Due to the close proximity of the VELO to the interaction point, it operates in a harsh non-uniform radiation environment. To understand the effects of radiation damage on VELO sensors, a VELO RR module was irradiated to a fluence equal to ~ 6 years of running at nominal conditions at the innermost radius of the VELO sensors. The module was investigated in a 120 GeV proton testbeam at the MTEST facility at FERMILAB. Due to the arrangement of the VELO sensors the irradiation will be non-uniform, which can create a transverse electric field in the silicon sensors. The transverse electric field can cause a shift in the cluster reconstruction position. The effect of the transverse electric field on the cluster reconstruction position are presented and shown to be . An estimated resolution of non-uniformly irradiated VELO R-sensors is made and measured to be $\sim 10\mu$m for both the *n-in-n* and *n-in-p* sensors in the RR module.

Declaration

This dissertation is the result of my own work, except where explicit reference is made to the work of others, and has not been submitted for another qualification to this or any other university. This dissertation does not exceed the word limit for the respective Degree Committee.

Abdi Noor

Acknowledgements

I would like to thank Themis Bowcock and Phil Allport for giving me the opportunity to pursue a PhD at Liverpool, and the Science and Technology Facilities Ccouncil for funding me. I would also like to thank the members of the Liverpool LHCb group for welcoming me into the group, I couldn't have asked for a better group of people to work with in particular Gianluigi Casse, Tony Affolder, Mark Tobin, Torkjell Huse, Kurt Rinnert, Karol Hennessy, David Hutchroft and Girish Patel.I would like to thank the members of LHCb VELO group at CERN particularly Olaf Behrendt, Aras Papadelis, Jan Buytaert, Eduardo Rodrigues, Chris Parkes, and JC Wang.

Contents

Chapter 1

Introduction

High energy physics (HEP) is the study of the most fundamental laws of the universe. The most successful theory in HEP for the past 50 years has been the Standard Model (SM). The Standard Model successfully describes the most fundamental particles and their interactions. However the Standard Model does not incorporate the theory of gravity or account for the mass of the neutrino. The origin of the masses of the W and Z bosons, and fermions has been accounted for by the existence of the Higgs mechanism but, the existence of the associated Higgs boson has not been established.

The Large Hadron Collider, at The European Centre for Nuclear Physics (CERN) is exploring signatures of new physics. The LHC does this by colliding counter rotating beams of protons to recreate conditions close to those of the early universe. One of the main goals of the LHC will be the discovery of the Higgs boson. To achieve this the LHC will collide the protons at a world record centre of mass energy of 14 TeV. Two of the four experiments at the LHC (ATLAS and CMS) are designed to study the decays of the Higgs boson, and ultimately make a measurement of its mass. Alongside these general purpose detectors are two specialised detectors ALICE and LHCb. ALICE studies a new phase of matter, known as quark gluon plasma. LHCb studies CP-violation in the B-sector, allowing us to understand why there is more matter than antimatter in the universe.

For the study of physics processes with rare decays and low cross sections, high luminosities are required. High luminosity comes at a price; high particle density. The high particle density leads to radiation damage in the detectors. In order not to compromise the physics, the detectors are required to be radiation hard. The radiation damage is dependent on the proximity to the interaction point, and is highest at the innermost regions of the LHC experiments. The innermost regions of the LHC experiments are

used for accurate tracking of charged particles, and at the LHC this is performed by the use of pixel and silicon strip sensors. Silicon has been used since the 1970's as a sensor material due to its superb energy and position resolution. The rapid growth in the use of semiconductors in HEP, is due to the requirement for very fast and precise position measurements that are required for the measurement of very rare and short lived particles.

The LHCb Vertex Detector (VELO) is the silicon strip tracking and vertexing detector for the LHCb experiment. The VELO utilises silicon sensors to provide precise tracking and vertexing information. The VELO detector is the detector most affected by radiation damage at the LHC, due to its very close proximity to the interaction region (~ 8 mm). In order to survive the extreme radiation environment the VELO sensors are made using radiation hard technology. However, the sensors will be required to perform in this harsh environment for ~ 10 years, and will ultimately undergo some degradation of performance. To understand the level of degradation of the sensors and the effects on the sensor performance irradiated VELO sensors were investigated in a proton testbeam. Two key measurements are made on the performance of the irradiated VELO sensor and presented in this thesis.

Chapter 2

Theoretical Context

Particle physics looks to explain how the fundamental constituents of matter interact with each other. Physicists have constructed a mathematical model to explain what is seen in experiment. This model is known as the Standard Model and has proved very successful in describing and predicting certain properties of the universe. This section will discuss the properties of particles in the Standard Model, it will start in general terms and then cover the formalism used to describe particles, for greater details see [1–3].

2.1 The Fundamental Particles and Forces

The Standard Model of Particle Physics (SM), is a theoretical framework that summarises our current knowledge of the fundamental forces of nature, with the exception of gravity, and their interactions. The three fundamental forces described in the Standard Model are the Electromagnetic, Weak and Strong forces. In the Standard Model matter is made of point like spin 1/2 fermions; the leptons and the quarks. The different interactions are mediated by spin-1 bosons. Every particle has an anti-particle partner with the same mass and spin, but with opposite charge and quantum numbers.

2.1.1 Fermions

Fermions are point like particles with half integer spin. The fermions can be subdivided into leptons and quarks. There are six leptons, each having a corresponding antiparticle. The leptons are themselves subdivided into three generations, with members of the higher

generations having larger mass than those in the lower generations. The members of the lepton generations are: the electron (e^-) and the electron neutrino (ν_e), the muon (μ^-) and the muon neutrino (ν_μ), and finally the tau (τ) and the tau neutrino (ν_τ). The quarks like the leptons are also subdivided into three generations. The members of the quark generations are: up (u) and down (d), charm (c) and strange (s), and finally top (t) and bottom (b). These six quarks carry a colour quantum number, which can be red, green or blue. This makes a total of eighteen quarks and eighteen anti-quarks. Quarks are never seen as free particles, they are always confined in colourless combinations as mesons (quark and anti-quark) or baryons (three quarks or three anti-quarks). The properties of the quarks and leptons are summarised in Table 2.1 and Table 2.2.

Generation	Lepton	Mass (MeV/c^2)	Spin	Q/e
1	e^-	0.510998928(11)	1/2	-1
	ν_e	<0.002 (CL=95%)	1/2	0
2	μ^-	105.6587315(35)	1/2	-1
	ν_μ	<0.19 (CL=90%)	1/2	0
3	τ	1776.82(16)	1/2	-1
	ν_τ	<18.2 (CL=95%)	1/2	0

Table 2.1: The Leptons in the Standard Model [3]

Generation	Quark	Mass (MeV/c^2)	Spin	Q/e
1	u	$2.3^{+0.7}_{-0.5}$	1/2	2/3
	d	$4.8^{+0.7}_{-0.3}$	1/2	-1/3
2	c	1275 ± 25	1/2	2/3
	s	95 ± 5	1/2	-1/3
3	t	173500+600+800	1/2	2/3
	b	4.18 ± 0.03	1/2	-1/3

Table 2.2: The Quarks in the Standard Model [3]

2.1.2 Bosons

In the Standard Model the Electromagnetic, Strong and Weak forces are mediated by spin-1 bosons. The leptons only participate in the Electromagnetic and Weak interactions which are mediated by the photon (γ) and the massive gauge bosons $W^{\pm}$ and Z. The quarks participate in Electromagnetic and Weak interactions, and also interact via the strong force which is mediated by the gluons (g). There are eight massless gluons, which also carry a colour charge. The properties of the bosons are shown in Table 2.3.

Force	Particle	Mass (GeV/c^2)	Spin	Q/e
Electromagnetism	γ	$<1 \times 10^{-27}$	1	0
Weak Nuclear	$W^{\pm}$	80.385 ± 0.015	1	± 1
	Z	91.1876 ± 0.021	1	0
Strong Nuclear	g	0	1	0
Mass	H	>115.5(CL=95%)	0	0

Table 2.3: The Bosons in the Standard Model

2.2 Mathematical Framework

Mathematically, the Standard Model is a quantum field theory in which the electro-weak and strong interactions are discussed in terms of gauge theories. A gauge theory is invariant under a set of local transformations, these are transformations in which the parameters are space-time dependent. The Standard Model is said to be a theory in which the electro-weak theory and Quantum Chromodynamics are unified into a structure denoted by the gauge groups SU(3)⊗SU(2)⊗U(1). Three gauge theories will be discussed in this section; Quantum Electrodynamics, Quantum Chromodynamics and the Electro-weak theory.

2.2.1 Quantum Electrodynamics

Quantum Electrodynamics (QED), is the quantum field theory that describes electromagnetic interactions. The Lagrangian form of the Dirac equation for a free particle of mass m and spin 1/2 is given by

$$\mathcal{L} = \bar{\psi}(i\gamma^{\mu}\partial_{\mu} - m)\psi \tag{2.1}$$

where ψ is the wave function of the fermion,and γ and μ are the gamma matrices. ∂_{μ} is the partial derivative with respect to μ. The Lagrangian is invariant under global phase transformations, but not invariant under local phase transformations. To enable gauge invariance an additional term must be added to the Lagrangian. The term introduced to achieve this is A_{μ}, this term transforms under local gauge invariance as

$$A_{\mu} \rightarrow A_{\mu} - \frac{1}{e}\partial_{\mu}\theta \tag{2.2}$$

The propagation of the field A_{μ} is described by the addition of a kinetic term, $1/4F_{\mu\nu}F^{\mu\nu}$, that does not break the invariance of the QED Lagrangian under gauge transformations. The field strength tensor,$F_{\mu\nu}$, is given by

$$F_{\mu\nu} \equiv \partial_{\mu}A_{\nu} - \partial_{\nu}A_{\mu} \tag{2.3}$$

By defining the covariant derivative, D_{μ} as:

$$D_{\mu} \equiv \partial_{\mu} + ieA_{\mu} \tag{2.4}$$

The resulting QED Lagrangian density is given by:

$$\mathcal{L} = \bar{\psi}(i\gamma^{\mu}D_{\mu} - m)\psi - \frac{1}{4}F_{\mu\nu}F^{\mu\nu} \tag{2.5}$$

The application of a local U(1) gauge transformation yields the vector field A_{μ}, which is the propagator of the electromagnetic force, the photon.

2.2.2 Quantum Chromodynamics

Quantum Chromodynamics (QCD) is a non-abelian gauge theory that describes the strong interaction. QCD is based on the application of the gauge invariance associated with the $SU(3)_C$ symmetry group, where the C denotes the colour quantum number, and requires eight massless gauge fields known as gluons. The gluons are the propagators of the strong force. Gluons carry a colour charge, which means that they are able to couple to each other. The Lagrangian density for QCD is constructed analogously to that of QED. The complete expression for the QCD Lagrangian density is given by

$$\mathcal{L} = \sum_f \bar{q}_f(x)(i\gamma_\mu D^\mu - m_f)q_f(x) - \frac{1}{4}F^a_{\mu\nu}(x)F^{\mu\nu}_a(x) \tag{2.6}$$

It is written in terms of quark fields, $q(x)$ and is summed over the quark flavours, f. The mass of a quark with flavour, f, is denoted by the term m_f. The covariant derivative, D^μ is defined as

$$D^\mu q = \left(\delta_\mu - ig_s\left(\frac{\lambda_a}{2}\right)A_\mu\right)q$$

where g_s is the strong coupling constant, A^a represents the eight gluon fields and $\frac{\lambda_a}{2}$ denotes the SU(3) generators.

The kinetic term $\frac{1}{4}F^a_{\mu\nu}(x)F^{\mu\nu}_a(x)$ contains the field strength tensor, $F^a_{\mu\nu}(x)$, of the gluon field, A^a, which is defined by Equation 2.7.

$$F^a_{\mu\nu}(x) = \delta_\mu A^a_\nu - \delta_\nu A^a_\mu - \sqrt{4\pi\alpha_s}\cdot f^{abc}A^b_\mu A^c_\nu \tag{2.7}$$

The term f^{abc} are the structure functions for the $SU(3)_C$ algebra, where the indices a, b, c run from one to eight. The strong coupling constant, α_s is given by

$$\alpha_s = \frac{g_s^2}{4\pi} \tag{2.8}$$

where g_s is the gauge coupling constant. α_s is referred to as a constant but varies as a function of the energy, known as the running of the coupling constant. At high energies or small distances the strong force reduces and quarks can be considered free particles. As quarks are pulled apart the binding energy between them increases until the point when it is energetically favourable to create a quark-antiquark pair.

2.2.3 Electroweak Theory

The Electro-Weak gauge theory is a unified theory of the electromagnetic and weak interactions. It uses $SU(2)\otimes U(1)_Y$ group to describe the interactions. Weak hypercharge, Y, is related to the charge, Q, and the third component of isospin, I_3, by

$$Q = I_3 + \frac{Y}{2} \tag{2.9}$$

Electro-weak interactions propagate using four gauge fields B_μ, W_μ^1, W_μ^2 and W_μ^3. B_μ is required to maintain invariance under electromagnetic transformations, while the W_μ^1, W_μ^2 and W_μ^3 are required to maintain invariance under weak transformations.

The weak interaction violates parity, meaning that the helicity H of a fermion is not conserved. This in turn means that there is no symmetry between left-handed (H=-1) and right-handed (H=+1) fermions. Thus, the Dirac field of a fermion can be separated into left-handed and right-handed components, with each generation of leptons and quarks represented by left-handed doublets and right-handed singlets. This grouping is illustrated by considering the first generation of fermions and is represented as

$$q_L \equiv \begin{pmatrix} u_L \\ d_L \end{pmatrix}; u_R,\ d_R \qquad l \equiv \begin{pmatrix} e_L \\ \nu_L \end{pmatrix}; e_R \tag{2.10}$$

The subscript L and R refer to left-handed and right-handed fermions, respectively. It should be noted that there is no right-handed neutrino present in the Standard Model and that neutrinos are also considered massless. Though neutrinos have been found to have mass this is not contained in the traditional Standard Model. To explain the presence of only left-handed neutrinos a number of theories are being tested.

The Standard Model also requires that gauge fields are massless, from experiment it has been shown that both the W and Z bosons are massive. To introduce mass to these fields and to fermions the Higgs mechanism has been postulated. This uses a scalar field called the Higgs field which breaks electro-weak symmetry and through a mechanism known as spontaneous symmetry breaking (SSB), where an arbitrary choice is made for a solution from a possible infinite number of ground states.

The Higgs mechanism results in a physically observable mass being associated with the four fields, they are a combination of more than one of these fields and these can be seen in equation (2.11),equation (2.12) and equation (2.13).

$$W_{\mu}^{\pm} = \frac{1}{\sqrt{2}} \left(W_{\mu}^{1} \mp W_{\mu}^{2} \right) \tag{2.11}$$

$$\begin{pmatrix} Z_{\mu} \\ A_{\mu} \end{pmatrix} = \begin{pmatrix} \cos\theta_{\mathrm{W}} & -\sin\theta_{\mathrm{W}} \\ \sin\theta_{\mathrm{W}} & \cos\theta_{\mathrm{W}} \end{pmatrix} \begin{pmatrix} W_{\mu}^{3} \\ B_{\mu} \end{pmatrix}$$

$$Z_{\mu}^{0} = W_{\mu}^{3}\cos\theta_{\mathrm{W}} - \mathrm{B}_{\mu}\sin\theta_{\mathrm{W}} \tag{2.12}$$

$$A_{\mu} = W_{\mu}^{3}\cos\theta_{\mathrm{W}} + \mathrm{B}_{\mu}\sin\theta_{\mathrm{W}} \tag{2.13}$$

The full electro-weak Lagrangian contains three components describing fermion interactions ($L_{Fermions}$), boson interactions (L_{Bosons}) and the Higgs mechanism (L_{Higgs}):

$$L_{EW} = L_{Bosons} + L_{Fermions} + L_{Higgs} \tag{2.14}$$

The first term describes the interactions between the massless gauge bosons and is given below:

$$L_{Bosons} = -\frac{1}{4}W^i_{\mu\nu}W^{i\mu\nu} - \frac{1}{4}B_{\mu\nu}B^{\mu\nu} \tag{2.15}$$

with the $W^i_{\mu\nu}$ and $B^{\mu\nu}$ the field tensors given by:

$$W^i_{\mu\nu} = \partial_\nu W^i_\mu - \partial_\mu W^i_\nu - g_2\epsilon^{ijk}W^j_\mu W^k_\nu$$

$$B_{\mu\nu} = \partial_\nu B_\mu - \partial_\mu B_\nu$$

Where g_2 is the weak isospin coupling constant and the indices i, j, k run from 1 to 3. The second term from equation 2.14 describes the coupling of fermions to the massless gauge boson mediators (W^1, W^2, W^3 and B).

$$L_{Fermions} = \overline{\Psi}_L\gamma_\mu D^L_\mu \Psi_L + \overline{\Psi}_R\gamma_\mu D^R_\mu \Psi_R \tag{2.16}$$

with the covariant derivatives defined by:

$$D^L_\mu = \left(\partial_\mu - ig_2\frac{\sigma^i}{2}W^i_\mu - ig_1\overline{Y}2B_\mu\right) \tag{2.17}$$

$$D^R_\mu = \left(\partial_\mu - ig_1\frac{Y}{2}B_\mu\right) \tag{2.18}$$

Here g_1 is the weak hypercharge coupling. The final term in equation 2.14 comes from the addition of the Higgs field and has the form:

$$L_{Higgs} = \left(D_\mu^L \phi\right)^\dagger \left(D_\mu^L \phi\right) - V(\phi) - g_f \bar{\psi} \phi \psi \tag{2.19}$$

where $V(\phi)$ is the scalar potential of the Higgs field. The first term is the interaction between the Higgs field and the gauge boson mediators and the last term comes from the Yukawa coupling between the fermions and the Higgs field giving rise to mass terms for the fermions.

2.3 CP Violation and The CKM Matrix

CP symmetry is the combination of charge conjugation (C), the transformation of a particle to its anti particle by changing the sign of its charge, and Parity (P) which is the inversion of the space coordinates, creating a mirror of the physical system. With the conservation of CP, particles and anti particles would be expected to behave in exactly the same way. As the universe demonstrates there is an imbalance in the amount of matter and antimatter, CP violation (CPV) can be used to explain some of this imbalance. CPV has previously been observed in the neutral kaon system [4].

CP violation can occur through three mechanisms in the B meson system: in the mixing, in the decay and in the interference between mixing and decay. The Cabbibo-Kobayashi-Maskawa (CKM) matrix describes mathematically the rotation between the weak eigenstates (d, s, b) and mass eigenstates (d′, s′, b′) of quarks and parameterises mixing between the three quark generations. This relation is shown in Equation 2.20. Each element corresponds to the possible quark transitions and represents the strength of weak charged current coupling between the quark flavours. The element V_{ij} represents the coupling of the i^{th} up-type quark to the j^{th} down-type quark. Experimental observations show that charged weak transitions between quarks of the same generation are common, whereas transitions between different quark generations are rare. Thus meaning that the diagonal terms of the CKM matrix are empirically close to one whilst the off-diagonal terms are small.

$$\begin{pmatrix} d' \\ s' \\ b' \end{pmatrix} = V_{CKM} \begin{pmatrix} d \\ s \\ b \end{pmatrix} = \begin{pmatrix} V_{ud} & V_{us} & V_{ub} \\ V_{cd} & V_{cs} & V_{cb} \\ V_{td} & V_{ts} & V_{tb} \end{pmatrix} \begin{pmatrix} d \\ s \\ b \end{pmatrix} \tag{2.20}$$

The CKM matrix is an 3×3 unitary matrix. The nine complex elements yield eighteen parameters, nine of which are unitarity constraints; six orthogonality and three normalisation. Of the nine remaining free parameters five are arbitrary phases associated with the six quark fields, and so can be discarded. Thus leaving four independent parameters which describe the CKM matrix; three Euler angles associated with the rotation in 3-dimensional space and one complex phase, δ. This phase enters the CKM matrix in the form:

$$e^{i(\omega t+\delta)} \tag{2.21}$$

This is not invariant under T violation and equivalently under CP violation. Therefore, it is through this complex phase that CP violation is introduced into the Standard Model.

2.4 Summary

Both QCD and the Electro-Weak theory are important in understanding and describing the physics at the LHC. The relevance of QCD arises from the strong interactions between protons, which result in $b\bar{b}$ production. QCD describes the momentum of the partons (quarks and gluons) produced from the proton-proton collisions using parton density functions. These describe the probability of a parton carrying a certain fraction of the momentum of the proton. The decay of the particles containing the b quarks is described by the Electro-Weak theory. LHCb is a dedicated b-physics experiment at the LHC. LHCb tests the Standard Model understanding of CP violation by measuring the decay of B-mesons to various nal and extracting the values for the element of the CKM

matrix. The production of b-particles is described in Chapter 4, as well as how LHCb has been designed to study them.

Chapter 3

The Use of Silicon Microstrip Sensors as Vertex Detectors

3.1 Introduction

Silicon detectors were first used as precision position measurement devices in high energy physics, in the early 1970's. These early devices were used as vertex detectors in fixed target experiments, to make lifetime measurements of the recently discovered charmed particles. These particles had lifetimes in the picosecond range, and required spatial resolutions of a few 10 μm to resolve the production vertex from the decay vertex. Bubble chambers and emulsions could achieve such resolutions but could not cope with the large data rates. Gaseous detectors were fast enough, but could not achieve the required resolution. The breakthrough in using silicon, came with the development of planar technology that allowed the construction of high quality silicon detectors [5]. Following the successful application of silicon sensors in fixed target experiments, they were also utilised in colliding beam experiments. All of the detectors at LEP, used silicon vertex detectors as well as those at the TEVATRON and B-factories.

Originally silicon detectors were exclusively used for vertexing, where measuring the track direction close to the interaction point is the objective. This meant that the silicon detector systems used in vertexing could be compact, and in some cases only required a few silicon sensors. This is not the case for tracking detectors, where good momentum resolution requires a large lever arm and several measurements along the track trajectory. This means that tracking detectors need to be large which initially excluded silicon detectors for reasons of cost. However, for high rate environments like

at the LHC gaseous are limited in usage close to the interaction point due high particle flux, which causes high occupancy and radiation damage. Silicon detectors, however, can still be operated under such conditions. The superior position resolution of silicon sensors makes it possible to achieve the same momentum resolution with a more compact device, leading to an overall reduction of the detector system.

The LHC experiments ATLAS, CMS, and ALICE use silicon pixel detectors for vertexing and silicon strip sensors for tracking. At LHCb, silicon strip sensors are used for both vertexing and tracking.

This chapter summarises some basic concepts in semiconductor physics relevant to silicon microstrip sensors. The topics discussed in this chapter are well documented elsewhere, for greater detail see references [6–10].

3.2 Semiconductor Basics

3.2.1 Pure Silicon

Silicon is a semiconductor, it forms a diamond like crystal structure. Silicon is a group IV element, and as such has four valence electrons. The Pauli exclusion principle prohibits the electrons bound to atoms or molecules from occupying the same energy level. In a solid, this leads to the discrete atomic energy levels being smeared into bands of energy states. In the valence band, the electrons are bound to a single nucleus and form the covalent bonds which exist between a silicon atom and its four neighbouring atoms. In the conduction band, which lies above the valence band, electrons are free to move about the crystal. Between the valance and conduction bands there lies a region with no allowed energy states, this region is referred to as the forbidden gap. The width of this bandgap determines whether a material is a conductor or a insulator. In an insulator the bandgap is >5 eV, so it is unlikely that an electron can be thermally excited from the valence band to the conduction band. In conductors the conduction band and valence band overlap, allowing the electrons to move freely. In a semiconductor like silicon the bandgap is ~ 1 eV, and at room temperature electrons can have enough energy to move into the conduction band, leaving behind a positively charged hole in the valence band. A neighbouring electron can fill this hole, which in turn creates a new hole. In this manner the hole can move around the crystal, effectively acting as a positive charge. The electrons can also move around the crystal carrying charge. The electron concentration

in the conduction band n, and the hole concentration in the valence band p are given by:

$$n = N_C e^{\left(-\frac{E_C - E_F}{kT}\right)} \tag{3.1}$$

$$p = N_V e^{\left(-\frac{E_F - E_V}{kT}\right)} \tag{3.2}$$

where E_V and E_C are the energies of the valence and conduction bands. k is Boltzmans constant, and T is the temperature. N_C and N_V are the effective density of states in the conduction and valence bands. E_F is the Fermi level which is the energy at which the occupation probability of a state is 0.5 it is given by:

$$E_F = \frac{E_C + E_V}{2} + \frac{kT}{2} \ln\left(\frac{N_V}{N_C}\right) \tag{3.3}$$

For intrinsic silicon the Fermi level is very close to the middle of the bandgap. At thermal equilibrium, the product between the charge carrier densities is always constant and is given by:

$$np = n_i^2 \tag{3.4}$$

where n_i is the intrinsic carrier concentration, the carrier concentration of pure silicon and is given by:

$$n_i = \sqrt{N_C N_V} e^{\left(-\frac{E_g}{2kT}\right)} \tag{3.5}$$

where E_g is the bandgap energy ($E_C - E_V$). The value for n_i of silicon at room temperature ($\sim$300K) is 1.45×10^{10} per cm^3.

3.2.2 Doped Silicon

The number of free moving electrons or holes in the crystal can be altered by adding impurities, this is known as doping. For example, when a group V atom like phosphorous (P) is added substitutionally to the silicon crystal lattice, it can donate its fifth electron to the conduction band. This creates a hole in the valence band without a corresponding electron in the conduction band. Similarly, when a group III atom like boron (B) is introduced into the crystal structure, it can accept an electron from a neighbouring silicon atom so that it may have a complete set of four electrons and bond covalently with its four nearest silicon atoms. Again this electron is not balanced by a hole in the valence band. Electron giving impurities are known as donors, and electron absorbing impurities are known as acceptors. By adding such impurities it is possible to create an excess of one carrier type. If the doping concentration is larger than the intrinsic carrier concentration, the carrier type introduced by doping dominates. Doping with a significantly higher number of donors makes the material n-type, and $n \sim N_D$ where N_D is the concentration of donor atoms. Similarly, adding a significantly higher number of acceptors makes the material p-type and $p \sim N_A$ where N_A is the concentration of acceptor atoms.

Doping introduces energy states in the forbidden bandgap. The energy states introduced by group III and group V elements are known as shallow levels, as the are very close to the conduction and valence bands. The energy gap between the conduction band and the shallow donor level is so small that at room temperature all the dopants are ionised. This is also the case for the shallow acceptor levels and the valence band. In the case of donors, the Fermi level is then becomes:

$$E_C - E_F = kT \ln\left(\frac{N_C}{N_D}\right) \tag{3.6}$$

Similarly for acceptors the Fermi level become:

$$E_F - E_V = kT \ln\left(\frac{N_V}{N_A}\right) \tag{3.7}$$

The Fermi level adjusts when the semiconductor is doped. If the impurities are n-type the Fermi level moves closer to the conduction band. Similarly, if the impurities are p-type the Fermi level moves closer to the valence band.

The charge carriers in silicon have a thermal velocity of the order of 10^4 ms^{-1}. In the presence of an electric field $\underline{E}$, the carriers have a drift velocity $\underline{v}$. The carrier drift velocity is given by:

$$\underline{v} = \mu \underline{E} \tag{3.8}$$

where μ is the carrier mobility. The carrier mobility is dependant on the carrier, and for silicon μ_e is 1350 V cm^{-1} s^{-2} and μ_h is 450 V cm^{-1} s^{-2}. The drift velocity of holes in silicon saturates at an electric field of around 10^5 V cm^{-1} at a velocity of 10^5 ms^{-1}. For electrons the maximum drift velocity is around 2×10^5 ms^{-1}, at an electric field of 4×10^3 V cm^{-1} [9].

The resistivity ρ is defined as the constant of proportionality between the electric field and the current density, J:

$$\underline{E} = \rho \underline{J} \tag{3.9}$$

its reciprocal is the conductivity σ. For a semiconductor with both electrons and holes as carriers:

$$\rho = \frac{1}{\sigma} = \frac{1}{q\left(\mu_n n + \mu_p p\right)} \tag{3.10}$$

if the semiconductor is doped, for example n-type then:

$$\rho \sim \frac{1}{q \mu_n n} \tag{3.11}$$

3.2.3 The *p-n* Junction Diode

The p-n junction is formed when a piece of n-type silicon comes in contact with a piece of p-type silicon. When the impurity concentration in a semiconductor changes abruptly from acceptor impurities N_A to donor impurities N_D an abrupt junction is obtained. The formation of the p-n junction causes a distortion of the band structure across the junction. The gradient of carriers across the junction causes diffusion of holes into the n-type region, and electrons into the p-type region. This results in unbalanced fixed positive ions in the n-type silicon, and unbalanced fixed negative ions in the p-type silicon. The unbalanced fixed charge regions constitute the space charge region (SCR), and as a result a voltage drop appears across the junction; which causes an electric field to appear across the junction. This electric field causes a drift of carriers across the junction, which is in the opposite direction to the diffusion of carriers across the junction. An equilibrium is reached when the built in potential difference (V_{bi}) prevents further charge transfer across the junction. The value for V_{bi} in silicon is about 0.6 V. The SCR contains very few free charge carriers and is referred to as the depletion zone. Figure 3.1 shows a p-n junction at thermal equilibrium. At thermal equilibrium the width of the depletion region for a double sided abrupt junction can be found by solving the 1D Poisson equation for the electric field in Figure 3.1, and is found to be:

$$W = \sqrt{\frac{2\epsilon}{q}\left(\frac{N_A + N_D}{N_A N_D}\right) V_{bi}} \tag{3.12}$$

where q is the electronic charge and ϵ is the permittivity of silicon. If the doping density is higher on one side, a one sided junction is obtained. For example if we have p^+n junction, where the p^+ indicates that the p-type sided is more heavily doped then $N_A >> N_D$ and the width of the depletion zone for this one sided junction is given by:

$$W = \sqrt{\frac{2\epsilon V_{bi}}{qN_{eff}}} \tag{3.13}$$

where $N_{eff} (= |N_D - N_A|)$ is the effective doping concentration of the less heavily doped (n-type) region.

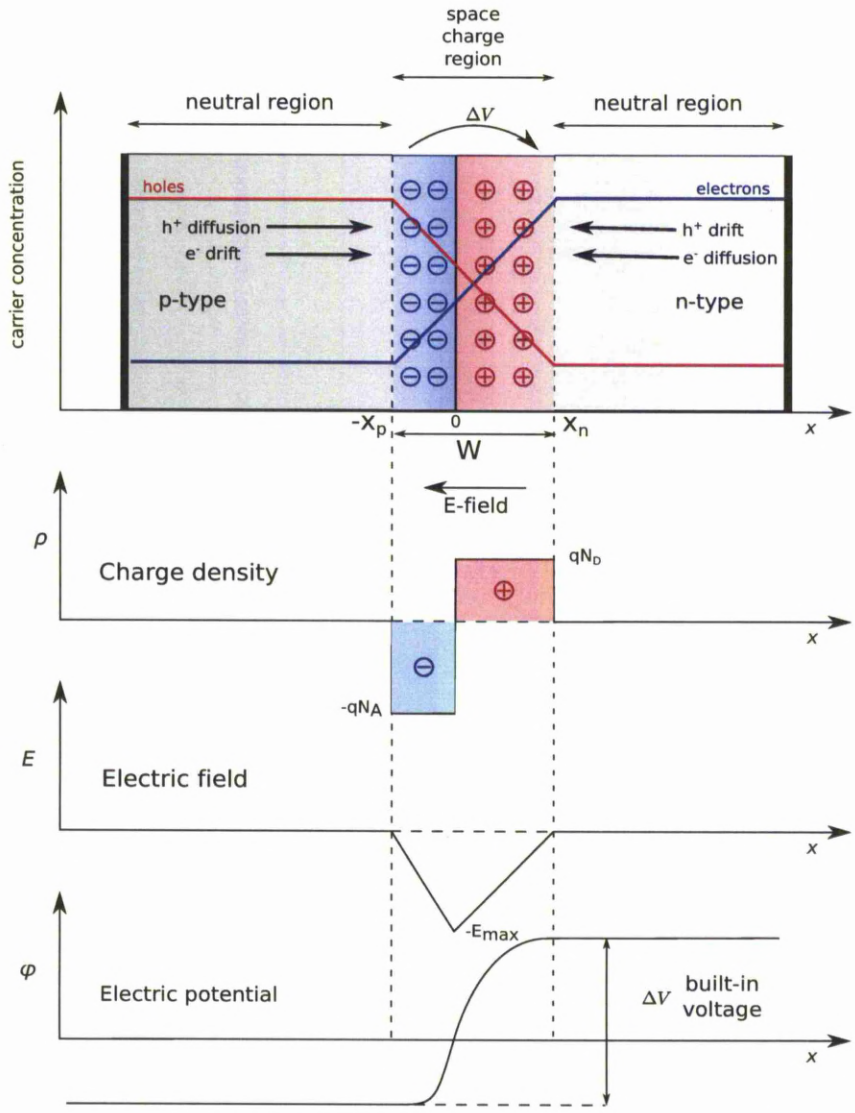

Figure 3.1: A forward biased p-n junction. (b) The IV characteristics of a silicon diode.

Applying an external potential to the junction produces current-voltage characteristics as shown in Figure 3.2. If the potential is the same polarity of V_{bi}, it is said to be in reverse bias, and the depletion region grows but the current remains very low. If the potential has the opposite polarity to V_{bi}, the junction is said to be in forward bias. In forward bias, when the applied external voltage compensates V_{bi}, the current rapidly increases as the diffusion current greatly exceeds the drift current. At this point the current increases dramatically due to avalanche breakdown. Silicon sensors are designed to

be operated in reverse bias, and for an applied voltage V>-V_{bi} the width of the depletion zone becomes:

$$W = \sqrt{\frac{2\epsilon\,(V_{bi} + V)}{qN_{eff}}} \tag{3.14}$$

Typically $V >> V_{bi}$, and V_{bi} is neglected, giving the width of the depletion region as

$$W = \sqrt{\frac{2\epsilon V}{qN_{eff}}} \tag{3.15}$$

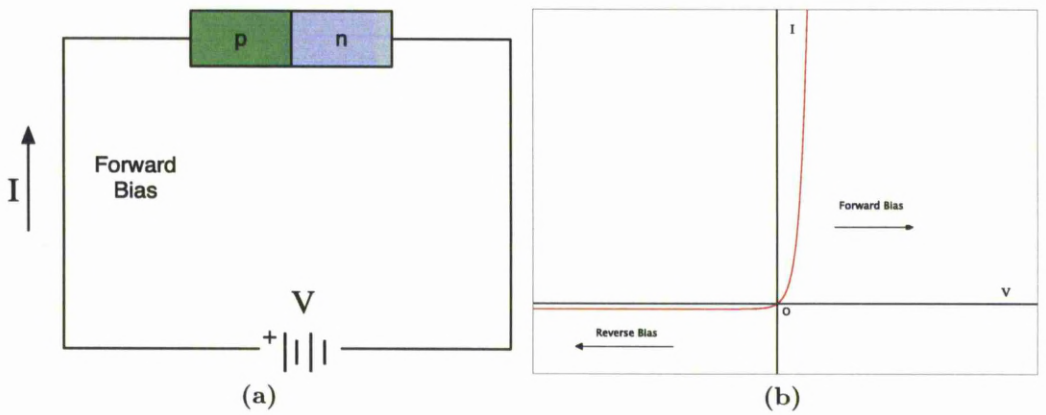

Figure 3.2: (a) A forward biased p-n junction. (b) The IV characteristics of a silicon diode.

The voltage required to fully deplete the diode is known as the depletion voltage V_{FD}, and is given by:

$$V_D = \frac{q}{2\epsilon}|N_{eff}|d^2 \tag{3.16}$$

where d is the diode thickness, at V_{FD} the width of the depletion region(W) is equal to the diode thickness (d).

The depletion layer is free of mobile charge carriers, and can be treated as a dielectric with a capacitance C. So the p-n junction diode can be regarded as a voltage dependant capacitor when operated in reverse bias. The capacitance of the diode is given by:

$$C = \frac{dQ}{dV} = \frac{\epsilon}{W}A = \sqrt{\frac{\epsilon q|N_{eff}|}{2V}}A \tag{3.17}$$

where A is the area of the diode. As the bias voltage is increased the effective carrier concentration (N_{eff}) decreases since the diode is becoming increasingly depleted of free charge carriers. The capacitance of the sensor decreases as the bias voltage is increased. At full depletion, depletion zone extends across the entire diode thickness, $W = d$, and the capacitance saturates. Plotting $1/C^2$ of a diode as a function of voltage, gives a linear line until V_{FD} is reached at which point it plateaus. The voltage at which point the slope plateaus is V_{FD}, and the slope of the linear region can be used to calculate N_{eff}.

A p-n diode operated in reverse bias is said to be strongly rectifying, since it allows the flow of current in only one direction. However, in practise there is a reverse or leakage current that flows through the diode. The leakage current has several components, namely; the diffusion current through the barrier, generation currents in the space charge region, surface currents at the Si/SiO_2 interface, and currents associated with the edges of the device. For an ideal device at low bias the diffusion current will dominate, but for real devises this is rarely the case and the generation current dominates. The generation current arises from electron-hole pair generation in the space charge region due to thermal excitations of electrons from the valence band to the conduction band. Thermally generated electron-hole pairs in the undepleted region do not contribute to the current, since due to the lack of an electric field they recombine. The generation current is given by:

$$J_g = \frac{qn_iW}{2\tau} \propto \sqrt{V_{bias}} \tag{3.18}$$

where τ is the carrier lifetime in the space charge region. The generation current is proportional to $\sqrt{V_{bias}}$, due to the bias dependence of the depletion region. Due to the

temperature dependence of n_i and τ the generation current has a temperature dependence given by:

$$J_g \propto \frac{n_i}{\tau} \propto T^2 e^{\left(-\frac{E_g}{2kT}\right)} \tag{3.19}$$

3.3 Microstrip Sensors

Silicon strip sensors used in high energy physics are based on the p-n diode. The basic principle of operation is that a depleted sensor can collect charge deposited by an ionising particle. This is due to the depletion region. It is this region which is suited to the detection of radiation, and acts as an ionisation chamber. Radiation incident in this region ionises the silicon and the resultant charge will be accelerated under the electric field to produce a measurable signal. Segmenting one side of the diode, will form discrete p-n junctions, and allow position measurements. The segmentation can be done as strip or pixels.

A segmented p-*in*-n sensor consists of a lightly doped n-type bulk, heavily doped p-type implanted strips, and is shown in Figure 3.3. On top of each of the implanted electrodes is a strip of metallisation (usually aluminium) to which the readout electronics can be bonded. Connecting the readout electronics to the implants can be done in two ways. A DC coupled sensor has the front-end electronics bonded directly to the aluminium. In an AC coupled device, the aluminium strips and the implants are separated by a thin insulating dielectric layer of silicon dioxide ($Si0_2$) or silicon nitride (S_3N_4). The dielectric layer prevents the large DC input from thermally generated leakage current from flowing through to the readout electronics. For AC coupled sensors there needs to be a way to connect the diode strips to a common bias line in order to apply the bias voltage. This can be done by connecting all strips to a common bias line with a high resistance. The resistors are integrated into the sensor by the deposition of doped polysilicon. On the opposite side to the implants, which consists of a heavily doped n-type layer in direct contact with a layer of metal forming an ohmic contact.

Applying a reverse bias voltage, will grow the depletion region and set up an electric field. The electric field will sweep electron-hole pairs created by ionising particles in the depletion region. The movement of the charge carriers will induce a signal at the implants, which is then amplified and shaped by the readout electronics.

Unlike in the bulk where the potential varies uniformly from the p-strip to the backplane, the cut edges of the sensor are at the backplane potential. A voltage drop occurs on the top surface between the p-strip bias ring and the top edges. Typically n-type implants along the top side edges and one or more guard rings are placed between the n implant and p-strip bias ring. The structure makes a well defined field over the top edge surfaces and a continuous potential drop in the high field region.

3.4 Sources of Noise

Sources of noise are present in sensors as well as the readout electronics used to amplify and process the signals they produce. The signal to noise ration (S/N) is the figure of merit for a sensor. Noise should be minimized, whilst signal can only be increased by increasing the sensor thickness. The noise contributing elements are: the input capacitance, C_{in}; the leakage current, i_L, sometimes called the shot noise; and the parallel and series resistances, R_P & R_S. The input capacitance is the most significant and mostly comprises of the inter strip capacitance and the backplane capacitance. Noise is generally expressed as Equivalent Noise Charge (ENC), and is given in the number of electrons contributing to the noise. The total noise is the quadratic sum of the noise contributions.

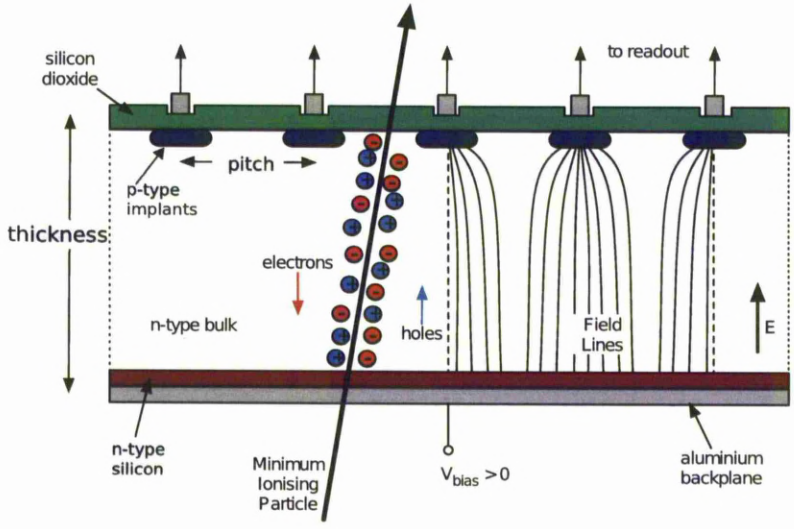

Figure 3.3: An AC coupled p-*in*-n microstrip detector, each p^+ strip has a layer of aluminium running along it, allowing it to be wire bonded to the readout electronics. The aluminium backplane, is in contact with n^+ silicon forming an ohmic contact.

3.5 Energy Loss in Silicon

Heavy charged particles (heavier than the electron), passing through matter primarily interact with nuclei and atomic electrons via elastic scattering and inelastic collisions. The inelastic collisions with atomic electrons are the most important when considering the energy loss of a charged particle. In inelastic collisions a fraction of the total kinetic energy is transferred from the traversing particle to the atom causing excitations or ionisation. If sufficient energy is transferred then the liberated electron can induce secondary ionisation. These high energy electrons are known as δ-electrons or knock-on electrons.

The average energy loss of a charged ionising particle travelling through a medium is given by the Bethe-Bloch equation [3]:

$$-\frac{dE}{dx} = 2\pi N_A r_e^2 m_e c^2 \frac{Z}{A}\frac{z^2}{\beta^2}\left[\ln\left(\frac{2\mathrm{m_e c^2}\beta^2\gamma^2\mathrm{T_{max}}}{\mathrm{I^2}}\right) - 2\beta^2 - \delta(\beta\gamma) - 2\frac{C}{Z}\right] \qquad (3.20)$$

where Z is the atomic number of the absorber, A is the atomic mass of the absorber, z is the charge of the incident particle, $2\pi N_A r_e^2 m_e c^2 = 0.1535$ MeVcm^2/g, with N_A Avogadro's number ($6.022 \times 10^{23}\mathrm{mol}^{-1}$), r_e is the classical electron radius ($= 2.817 \times 10^{-13}$ cm), $m_e c^2$ is the electron rest mass (0.511 MeV), I is the logarithmic mean excitation energy (174 eV), β is the particle speed as a fraction of the speed of light, γ is the Lorentz factor $\left(= \frac{1}{\sqrt{1-\beta^2}}\right)$, δ is the density correction and takes into account the shielding, T_{max} is the maximum kinetic energy, which can be imparted to a free electron in a single collision and C is a shell correction. Figure 3.4(a) shows a plot of the mean energy loss of a particle travelling through various materials at a broad range of momenta (expressed in terms of $\beta\gamma$). There is a dependence on atomic number (Z) of the material, with energy losses decreasing with increasing Z . In the region where $\beta\gamma < 1$, the energy loss due to ionisation depends strongly on the velocity of the traversing particle, decreasing with $1/\beta^2$ until it reaches a minimum at $\beta\gamma \sim 3.5$; giving the minimum of deposited energy in the medium. The energy loss then starts to rise logarithmically with γ as $\beta \to 1$.

The mean energy loss in silicon given by the Bethe-Bloch function is 3.88MeV/cm. For 300 μm of silicon this results in a mean energy loss of 116 keV. The Bethe-Bloch formula only gives the average energy loss per unit length, however it does not account for the fact that each passage through the material is a sum of a series of stochastic

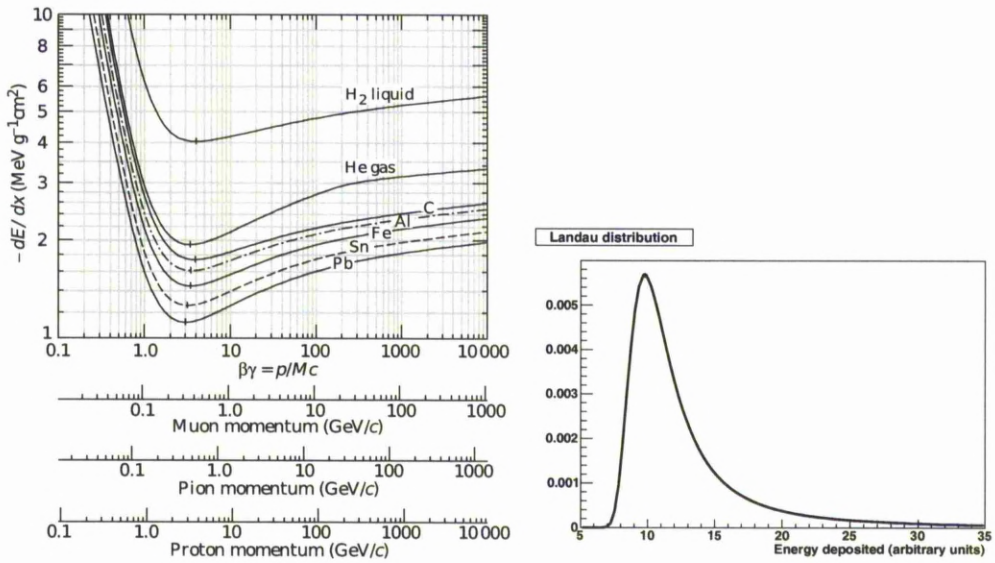

(a) (b)

Figure 3.4: (a) Mean energy loss for a particle travelling through various materials as a function of $\beta\gamma$ as described by the Bethe-Bloch. (b) Sample Landau distribution in arbitrary units.

events. The actual energy loss (ϵ) is distributed around this mean value. The probability distribution giving the actual energy loss of a charged particle in a thin absorber of thickness d, is the Landau function [11];

$$f_L(\epsilon, d) = \frac{\phi(\lambda)}{\xi} = \frac{1}{\pi\xi}\int_0^\infty e^{-u(\lambda+lnu)} sin(\pi u) du \tag{3.21}$$

where ϵ is the energy loss, and ξ is proportional to d and depends on material properties and particle velocity. ϕ (λ), is the probability density of λ. λ is dimensionless and depends on the energy loss ϵ. A typical Landau curve is plotted in Figure 3.4(b). The asymmetric long tail towards the energy deposits is due to the δ-electrons. The peak of the Landau gives the Most Probable Value (MPV) for a MIP passing through the silicon. The MPV of a Landau distribution is approximately 30% lower than the mean given by the Bethe-Bloch equation. This gives the most probable energy loss for 300 μm of Si a value of 0.7 $\times$ 116keV= 81keV. In silicon, the average energy required to liberate 1 electron-hole pair is 3.6eV. Hence, the most probable number of charges for 300 μm is 22500e. If we take an arbitrary noise value of 1000e, this would give a signal-to-noise (S/N) of 22.5.

3.6 Position Resolution

The resolution of a sensor is determined by its strip pitch, where pitch is the geometric separation between strips. As a particle passes through the sensor, a cloud of ionised particles is created. If the strip pitch is greater than the size of the charge cloud, then all the charge is collected on one strip. For this case the track position is given by the strip position and, the standard deviation of a single strip cluster, and hence, the resolution is given by:

$$\sigma = \sqrt{\langle x^2 \rangle - \langle x \rangle} = \sqrt{\int_0^1 x^2 dx - \left(\int_0^1 x dx \right)^2} \tag{3.22}$$

$$\sigma = \frac{1}{\sqrt{12}} \tag{3.23}$$

where unit pitch is assumed. This is known as binary resolution. More accurate position information can be obtained when charge is shared across strips. Figure 3.5 shows a particle passing through a sensor and the charge collected on a single strip. On the right hand side the charge is shared over two strips, for a charge sharing hit the resolution is always better than binary. The track position can be calculated by interpolation between the two strips. A simple way to do this is by a charge weighting average

$$t_{pos} = \frac{\sum_i Q_i d_i}{\sum_i Q_i} \tag{3.24}$$

Where Q_i is the charge on a strip, d_i is the strip position and i denotes a sum over the cluster's strips. This assumes that the charge division between the two strips is linear.

3.7 Radiation Damage in Silicon

The high luminosity at the LHC will create a high particle density environment at the interaction points of the experiments. The high luminosity will benefit the physics

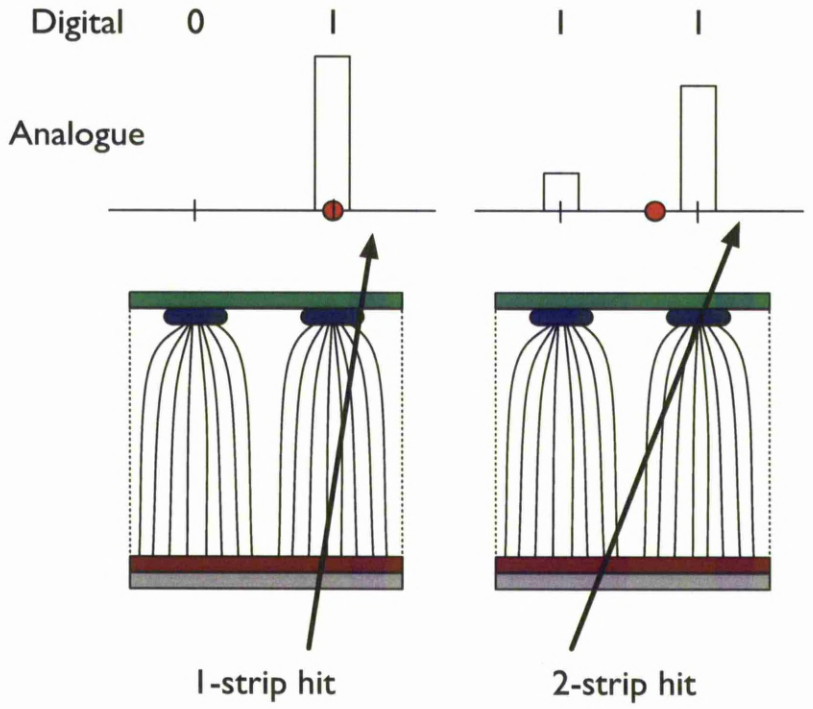

Figure 3.5: Position reconstruction for 1 strip and 2 strip cluster. The red circle indicates the cluster reconstruction position. Tracks that share charge across more than one strip give better than binary resolution.

programmes of the experiments, but will create a challenge in operating the detectors in such harsh radiation environments. The detectors that will be affected the greatest will be those that are closest to the interaction point; in all of the LHC experiments this is the silicon tracking detectors. Understanding radiation damage in silicon is critical for operating the silicon tracking detectors at the LHC, and is an area of R&D. The main effects of radiation damage are: (i) an increase in the leakage current;(ii) a change of effective dopant concentration N_{eff}; (iii) and a decrease in the charge collected.

This section gives a brief description of the mechanisms of radiation damage in silicon, and the effects it has on the performance of silicon sensors.

3.7.1 Damage Mechanisms

Surface Damage

Surface damage is caused by ionising radiation passing through the silicon detector and damaging the surface oxide. The radiation can produce electron-hole pairs at the surface, the electron-hole pairs can recombine but it is possible that the more mobile electrons escape under the influence of electric fields in the oxide leaving behind the holes. The holes become trapped in the silicon oxide, and contribute to a fixed positive oxide charge [12]. Also, ionising radiation causes the introduction of new states in the band gap at the silicon-silicon dioxide interface. The new states can be occupied by electrons or holes depending on the potential distribution in the interface, this also contributes to the oxide charge [13].

Surface damage introduced by the ionising radiation can be controlled by design and manufacturing precautions. The amount of surface damage depends on the quality and thickness of the oxide, and the energy of the ionising radiation. Surface damage causes concentrations of charge leading to electric fields at the strip oxide implant boundaries, causing the sensor to breakdown.

Bulk Damage

A more limiting factor on sensor performance is the radiation induced displacement damage in the bulk of the sensor. Since the characteristics of sensor depletion regions depend primarily on the bulk properties of the sensor, lattice defects in the bulk can have a significant impact on the sensor performance, while displacement in the silicon surface can usually be neglected.

Bulk damage depends on non-ionising energy loss and alters the electrical properties of the crystal. When an incoming particle with sufficient energy impinges on a silicon atom and displaces it from its lattice site, a Primary Knock on Atom (PKA) is produced. A minimum energy of ~ 15 eV is required for this displacement to occur. The effect of knocking atoms out of their lattice sites is the creation of interstitial silicon atoms and vacancies. If the PKA has sufficient recoil energy (> 25 eV) it can move freely through the silicon causing further displacement, causing a cascade. These defects can meet with impurity atoms or other vacancies and interstitials in the silicon and form defects clusters. Along the path of the PKA vacancy interstitial pairs are created known

as Frenkel Pairs. The PKA loses energy and eventually will come to the end of its recoil energy range, where the interaction cross section increases resulting in a region of high density lattice defects known as a terminal cluster. If the initial recoil energy of the PKA was 1-2 eV, a point defect will occur. If the defect clusters are electrically active, they introduce states in the silicon bandgap. These defects alter the properties of the bulk silicon. The initial dopants in the lattice may lose their function as donors or acceptors if they become coupled to radiation induced defects and form defect complexes [14]. Figure 3.6 illustrates some defects in the lattice.

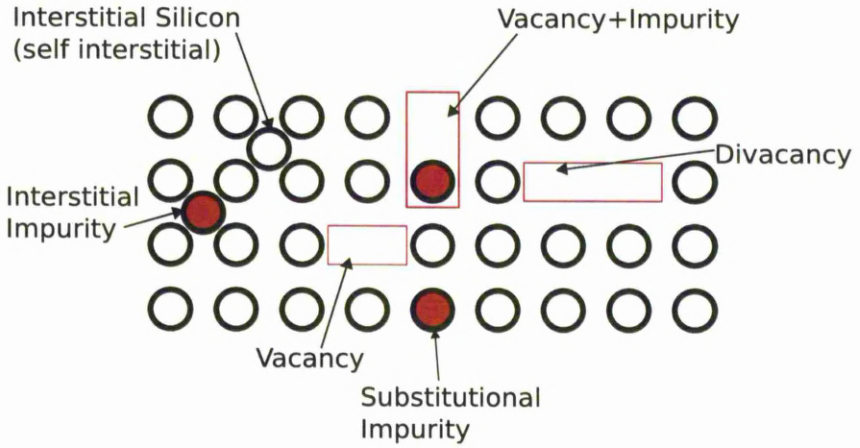

Figure 3.6: Some defects in the silicon crystal lattice.

The defects introduce levels into the band gap, these defect levels give rise to effects which have consequences on the performance of the detector. The effects caused by the defect levels are:(i) generation, causes an increase of the leakage current;(ii) compensation, which causes a change in the effective doping concentration; and (iii) trapping, which changes the collected charge. A brief description of these process is given below and shown diagrammatically in Figure 3.7.

Generation

This is the creation of electron-hole pairs due to the thermal excitation of an electron from the conduction band to the valence band via a level in the band gap. Energy levels formed by defects can act as generation centres where electrons can be promoted to the conduction band simultaneously as holes are released to the valence band. These generation centres are a source of free charge carriers in the space charge region and result in an increase in leakage current. See Figure 3.7(a).

Compensation

Electrically active fixed defects in the space charge region contribute to the effective doping concentration, N_{eff}. Only electrically active contribute towards N_{eff}. These are usually donors in the top half of the bandgap and acceptors in the lower half. Typically donors in the bottom half of the band gap and acceptors in the top half are not ionised. This change in N_{eff} changes the depletion voltage. See Figure 3.7(b).

Trapping

Fixed deep defect levels can act as trapping centres, and have a influence on the charge collection efficiency of the detector. An electron-hole pair may be trapped for a short period of time, which reduces the charge collection efficiency of the detector if the shaping time of the read-out electronics is short compared to the detrapping time of the defect level. Shallow levels do not contribute to charge trapping significantly, due to the fast detrapping time. See Figure 3.7(c)

Annealing

The defects which are the result of radiation damage, are dependent on temperature and time as well as fluence. Warming up radiation damaged sensors, triggers annealing processes. Annealing is the reordering of defects within the silicon lattice due to thermal treatment. The annealing processes can have a beneficial, and an adverse effect on the performance of the sensor after irradiation. The reordering of the defects, has the effect of improving the performance of the radiation damaged device for a short time, this is called beneficial annealing. After the short term beneficial annealing there is a longer term reverse annealing, the reverse annealing results in the deterioration of the detector performance.

NIEL

The radiation damage to silicon sensors depends the type of radiation, and the energy of the radiation. For example charged particles will interact electromagnetically and neutral particles, like neutrons, which result in nuclear collisions. The Non-Ionising Energy Loss (NIEL) hypothesis[15], allows irradiations by different particles and different

energies to be normalised to each other. The bulk radiation damage from particles with different energy and type, is normalised to the 1 MeV neutron equivalent damage (1 MeV n_{eq}). In the NIEL hypothesis bulk radiation damage is a result of only the Non Ionising Energy Loss interactions. The equivalent fluence (Φ_{eq}), is the fluence of 1 MeV neutrons which would have caused the same extent of damage, where fluence is the integrated flux.

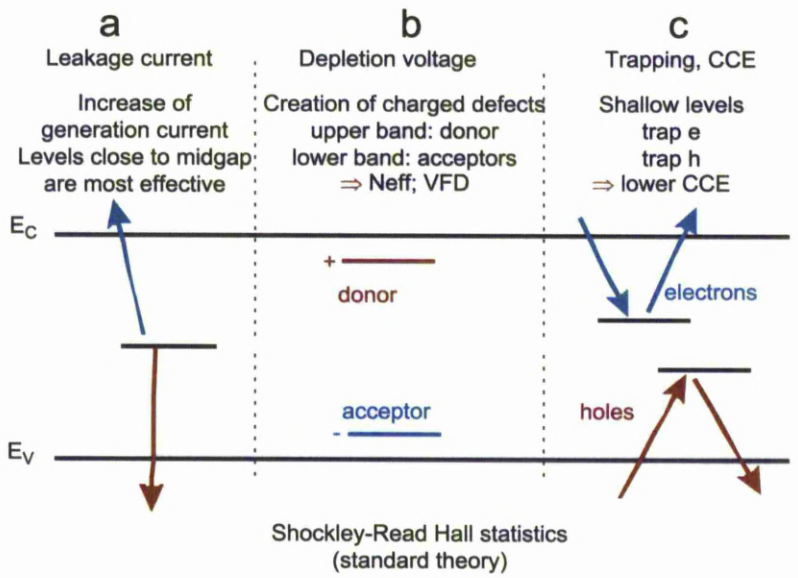

Figure 3.7: The different defect levels and their effects. All the relevant defect levels due to radiation are located in the forbidden energy energy gap.

3.7.2 Detector Performance After Irradiation

Effective Doping Concentration

A parameterisation has been developed to predict the performance of devices given a set of irradiation and thermal conditions, called the Hamburg Model [16][17]. The Hamburg Model provides a successful parameterisation of a wide range of experimental results on the behaviour of silicon detectors as a function of irradiation, temperature and time.

The effective doping concentration N_{eff} has been found to change with irradiation. The N_{eff} of n-type silicon has been found to fit the function [16]:

$$N_{eff} = |N_{eff,0} \exp^{-c\Phi_{eq}} - \beta\Phi_{eq}| \tag{3.25}$$

where $N_{eff,0}$ is the initial dopant concentration, Φ_{eq} is the 1 MeV n_{eq} fluence. β is the generation rate of acceptor like defects and c is the donor removal constant. This parameterisation is only true for sensors after annealing. For n-type silicon, donor removal is said to occur which is represented as an exponential decay of N_{eff} as a function of fluence. Since the depletion voltage is proportional to N_{eff} an initial decrease in the depletion voltage is observed. N_{eff} will approach zero at a given fluence and the material is said to undergo type inversion from n-type to p-type material. With increasing fluence the material becomes more and more p-type and the full depletion voltage increases.

The changes in the effective doping concentration of an irradiated diode when annealed after irradiation can be parameterised into three main components:

$$\Delta N_{eff} = N_{eff,0} - \Delta N_{eff} \tag{3.26}$$

where

$$\Delta N_{eff} = N_A + N_C + N_Y \tag{3.27}$$

where N_A is the beneficial annealing component, N_C is the stable component, with an exponential donor removal term and a linear acceptor creation rate g_C. N_Y is the reverse annealing component. An example of the change in N_{eff} as a function of time is the annealing curve shown in Figure 3.8.

Leakage Current

The change in the leakage current per unit volume of silicon can be parameterised by [16]:

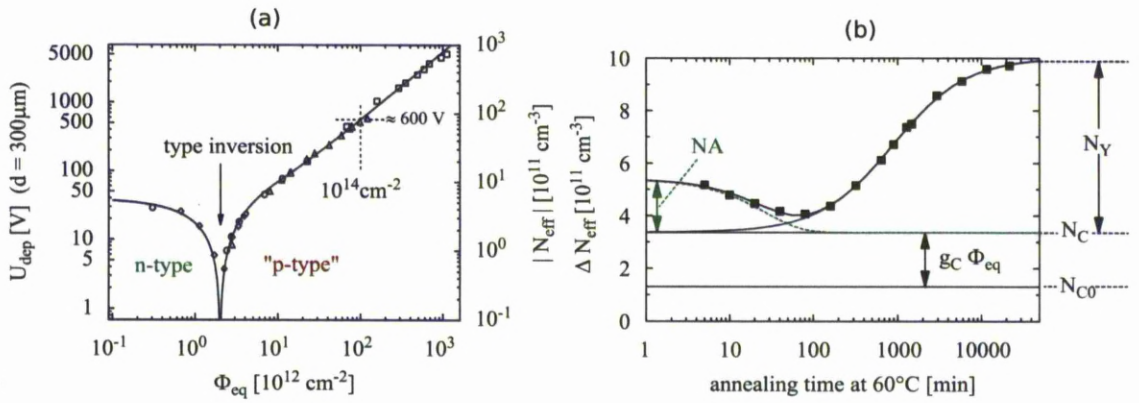

Figure 3.8: (a) N_{eff} and V_{FD} as a function of 1 MeV n_{eq} fluence. Donor removal and the introduction of acceptor like defects causes the n-type bulk to type invert. After type inversion to p-type, N_{eff} increases linearly with fluence.(b) N_{eff} and V_{FD} as a function of annealing time. The short term beneficial annealing component,NA, is proportional to the fluence and leads to a reduction in V_{FD}. This is only true for sensors that have type inverted. For non type inverted sensors the beneficial annealing leads to an increase in V_{FD}. The stable component, N_C, is given by defects that are stable at temperatures up to about 100 °C. The stable component has no time dependence and can not be controlled purely by temperature choice. The last component is called the reverse annealing component and is responsible for the increase in the depletion voltage.

$$\Delta I = I - I_0 = \alpha \Phi_{eq} V \tag{3.28}$$

where Φ_{eq} is the 1 MeV n_{eq} particle fluence, and α is the reverse current damage factor. The reverse current is proportional to the width depletion region, and follows a square root dependence with the reverse bias voltage. The leakage current saturates at voltages above the depletion voltage. The leakage current also shows a strong temperature dependant annealing. Figure 3.9 shows how the leakage current changes with fluence and annealing time. The leakage current starts to drop off after irradiation, this is due to the beneficial annealing, and then saturates to around half its maximum value during exposure. The reverse annealing process is suppressed in the case of the leakage current. The leakage current is a source of shot noise, and even causes the sensors to overheat if not cooled. This is known as thermal runaway.

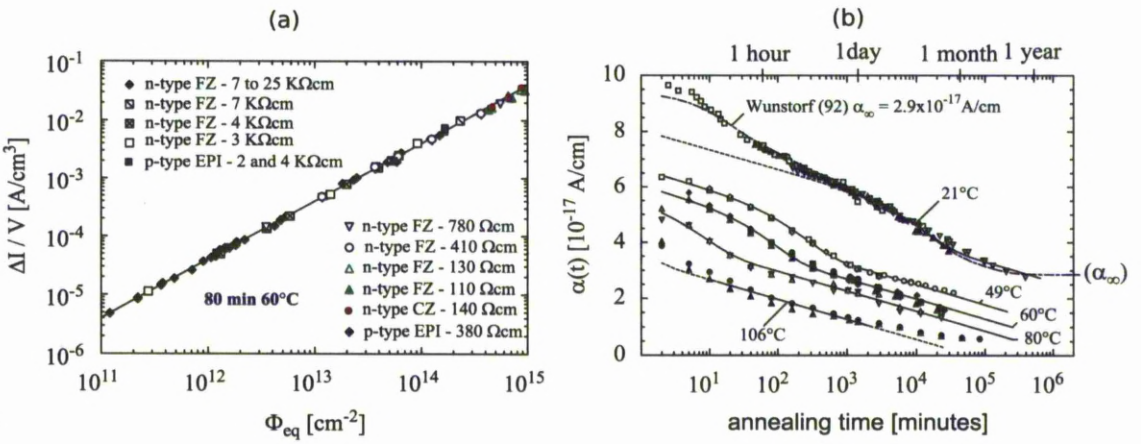

Figure 3.9: The dependence of leakage current with (a) fluence and (b) annealing time.

Charge Trapping

At high fluence charge trapping is the main limiting factor of the detector performance. Charge trapping is characterised by a effective trapping time, τ_{eff} which is the time a carrier can survive before trapping. The inverse effective trapping time depends on the fluence and is given by[18]:

$$\frac{1}{\tau_{eff}} = \beta_{eh}\Phi_{eq} \tag{3.29}$$

where $\frac{1}{\tau_{eff}}$ is the effective trapping probability, and Φ_{eq} is the 1MeV n_{eq} fluence. β_{eh} is a proportionality constant and depends on temperature, and time. β_{eh}, is different for electrons and holes due to their different mobilities, $\beta_h > \beta_e$ which means holes are most likely to get trapped. The trapping probability is proportional to the concentration of trapping centres caused by defects. The degradation of charge collection can be described by:

$$Q(t) = Q_0 \exp^{-t/\tau_{eff}} \tag{3.30}$$

where Q_0 is the original charge, and t is the time.

For Φ_{eq} of 10^{15} n_{eq} cm^{-2} the effective trapping time in a 300 μm sensor is $\sim$2.5 ns which corresponds to a trapping distance of $\sim$200 μm. If the fluence is increased to 10^{16} n_{eq} cm^{-2}, the trapping distance is $\sim$25 μm. This will greatly reduce charge collection efficiency of a sensor since the charges no longer reach the collecting electrodes especially if the readout electronics has fast shaping time.

3.8 Improving Radiation Tolerance

3.8.1 Oxygen Enrichment

Point defects like vacancies (V) or interstitials (Si_i) can move through the lattice and form other defects like a divacancy (V_2) or may anneal by an interstitial silicon atom moving into a lattice vacancy. Impeding the formation of electrically active defect sites has yielded oxygen as an impurity that captures vacancies. Oxygen has been shown to be effective in improving the performance of oxygen enriched sensors with respect to charged particle irradiation. Oxygen enriched sensors that have been irradiated with charged particles have a lower rate of acceptor generation and better annealing performance[16][19]. Neutron irradiated oxygen sensors have the same performance as non-enriched sensors. Oxygen enriched sensors have an advantage where used close to the interaction point when charged particles dominate. Such sensors are utilized at the ATLAS and CMS pixel detectors and the LHCb VELO. Figure 3.10 shows how V_{FD} changes for differently engineered silicon sensors.

3.8.2 n-side Readout

Studies have shown that sensors with n-side readout are considerably more radiation hard than those with the standard *p-in-n* geometry[20][21]. This improvement comes from reading out electrons at the implants. Electrons have longer trapping times, and higher mobility than holes. During annealing trapping times increase for electrons and decrease for holes [18].

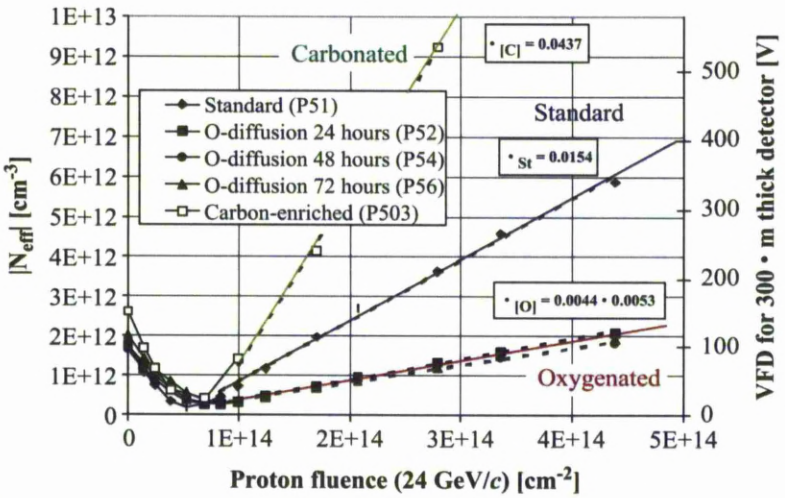

Figure 3.10: The evolution of V_{FD} vs time for differently engineered diodes. The beneficial influence of oxygen and damaging effects of carbon are visible.

n-in-n

Sensors with the *n-in-n* geometry consist of a lightly doped n-type substrate with highly doped n^+ implants, and a p-type backplane. These *n-in-n* sensors, deplete from the implant side after irradiation. This means that they can be operated underdepleted. However, the disadvantage of using an *n-in-n* device is that the readout strips must to be isolated [22]. Strip isolation helps to prevent shorts between neighbouring strips due to conductive channels induced through positive charge trapping at the dielectric bulk interface. The positive charge increases with exposure to radiation and this causes a low resistivity conductive channel at the wafer surface that effectively shorts the segmented strips. There are a number of techniques to isolate the strips, the two examples are: the p-stop technique, and the p-spray technique. The p-stop technique involves introducing implants in between the individual n^+ strips, with the p^+ implants collecting the mobile electrons. The p-spray technique involves applying an overall relatively low dose of p implantation on the entire wafer. This will leave a p^- layer in between the n^+ strips, which will again act to collect the electrons. Also the fabrication of *n-in-n* sensors requires double sided processing, which increases both the complexity and cost of these devices.

n-in-p

Sensors with the *n-in-p* geometry consists of a lightly doped *p*-type substrate with highly doped n^+ implants. The charge collection of *n-in-p* devices, after irradiated has been shown to be far better than *p-in-n* devices [23]. The charge collection of *n-in-p* detectors is also superior to that of oxygenated *p-in-n* devices. This configuration has the advantage that the *p*-type bulk does not undergo type inversion after being subjected to radiation, the bulk becomes more *p*-type with increasing fluence. As a result of the non-inverted bulk, junction migration does not occur in a *n-in-p* diode and the high electric field remains at the readout side of the detector.

3.9 Summary

Silicon microstrip sensors are widely used in high energy physics for tracking and vertex detection. The innermost tracking detectors of all of the LHC experiments are exploiting this technology. The radiation environment at the LHC will be very high, especially at the regions closest to the interaction point. Operating the silicon tracking sensors at the inner regions of the LHC experiments will be challenging due to the harsh radiation environment. Radiation damage degrades the performance of silicon sensors, and understanding how radiation damage changes the performance of the silicon sensors is an important and ongoing task. To this end a number of techniques have been developed to improve the radiation hardness of silicon sensors at the LHC.

Chapter 4

The LHCb Experiment at the Large Hadron Collider

4.1 The LHC

The Large Hadron Collider (LHC)[24] is a proton-proton collider at the European Organisation for Nuclear Research (CERN). The LHC is housed in a 27 km circumference ring, on the Franco-Swiss border close to Geneva, Switzerland. The LHC ring is shown in Figure 4.1. The LHC is designed to collide two counter rotating beams of protons at a centre of mass energy of up to 14 TeV and has a design luminosity of $10^{34}\text{cm}^2\text{s}^{-1}$. Table 4.1 shows the main design parameters of the LHC. The LHC has been designed to search for new physics, and perform precision tests of the Standard Model. There are four collision points at the LHC, each housing an experiment, ATLAS [25], CMS [26], LHCb [27], and ALICE [28]. Two of the experiments are general purpose detectors, ATLAS and CMS, are designed to search for new physics beyond the Standard Model. ALICE is dedicated to heavy ion collisions, which allow the study of quark-gluon plasma. LHCb is a precision experiment designed to study CP violation and rare decays in the B-sector.

Due to difficulties during the planned start up in 2009, the LHC has been running at a lower centre of mass energy of $\sqrt{s}$=7 TeV since 2010. Over the course of 2010 and 2011 the number of bunches increased to over 1000 in each direction and the LHC delivered 36 pb^{-1} to LHCb in 2010. Using a larger number of bunches 304 during 2011, more than 1 fb^{-1} was recorded at LHCb.

Parameter	Value
Circumference	27 km
Proton energy at collision	7 TeV
Centre of mass energy	14 TeV
Circulating beam current	0.58 A
Luminosity	$10^{34}\text{cm}^2\text{s}^{-1}$
Number of bunches	2808
Number of particles per bunch	$1.5\text{x}10^{11}$
Bunch length	7.5 cm
Time between beam crossings	25 ns
Luminosity at LHCb	$2\text{x}10^{32}\text{cm}^2\text{s}^{-1}$
Beam size at LHCb	70 μm
Crossing angle at LHCb	200 μrad

Table 4.1: The main design parameters of the LHC.

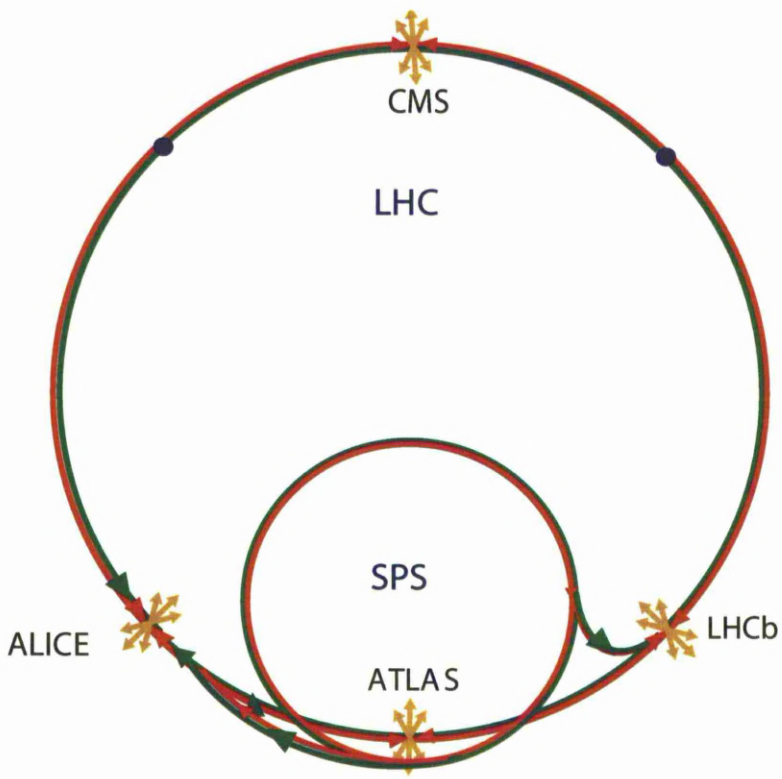

Figure 4.1: The LHC ring.

4.2 B Production at the LHC

The main production mechanisms of $b\bar{b}$ pairs from proton-proton collisions at $\sqrt{s}$=14 TeV are the leading order processes of gluon-gluon fusion (14.4%), and next to leading order process such as flavour excitation (60.3%) and gluon spitting (25%). Production through quark anti-quark annihilation is also possible but makes a small contribution (0.2%) [29][30]. Feynman diagrams of the examples can be seen in Figure 4.2 and Figure 4.3.

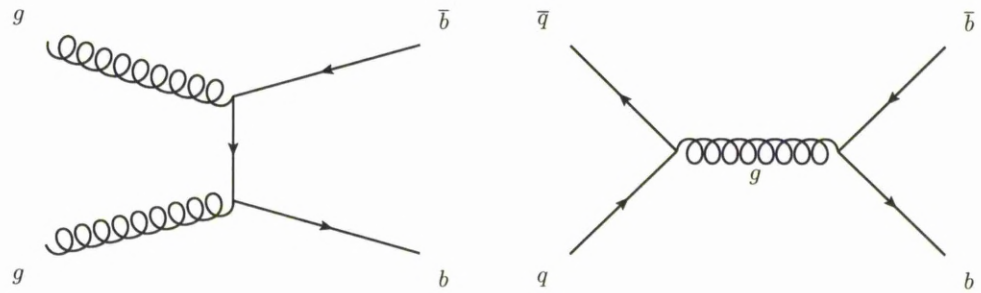

Figure 4.2: Leading order Feynman processes for $b\bar{b}$ production. (a) Gluon fusion. (b) Pair creation from $q\bar{q}$.

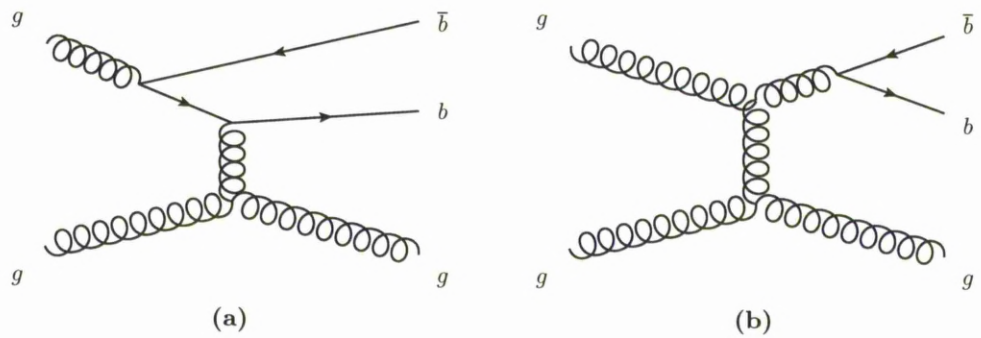

Figure 4.3: Next to leading order Feynman processes for $b\bar{b}$ production. Examples of (a) flavour excitation (b) and gluon splitting are shown.

The partons participating in a pp collision typically have unequal momenta, which boosts the B-system in one of the two beam directions. As a result, the angular distribution of the b and the $\bar{b}$ peaks close to the polar angles $\theta = 0$ and $\theta = \pi$. The predicted angular distributions of produced b-quarks according to a PYTHIA Monte Carlo simulation[31] at LHC energy are shown in Figure 4.4. After production, the

quarks of the $b\bar{b}$ pair hadronise separately and incoherently from each other. The B-system has a typical boost of $\beta\,\gamma$ = 15-20 with respect to the laboratory frame, which results in decay lengths of around 1 cm for the B-mesons. Such decay lengths facilitate the detection of B-mesons and allow observation of many B_s oscillation cycles.

4.3 The LHCb Detector

The main goal of LHCb is to perform precision measurements of B-mesons. The $b\bar{b}$ pairs will be predominantly produced in either the same forward or backwards cone relative to the beam axis, and at high rapidity. This has motivated the angular coverage of the detector and as a result LHCb is a single armed forward spectrometer. LHCb has an acceptance of 10-250 mrad in the horizontal plane and 10-300 mrad in the vertical plane, corresponding to a pseudorapidity range of $1.7 < \eta < 5.3$ and $2.1 < \eta < 5.3$. The detector layout is shown in Figure 4.5. An estimated 10^{12} $b\bar{b}$ pairs at the nominal luminosity will be produced and in the LHCb acceptance each year. LHCb experiment employs a right handed co-ordinate system, with the origin at the interaction point, the z axis along the beam line and the y axis in the vertical direction. The origin is located in the centre of the interaction region.

LHCb will operate with a luminosity of $2\text{x}10^{32}\text{cm}^2\text{s}^{-1}$, this is achieved by defocusing the beam. Reducing the luminosity reduces the average number of interactions per bunch crossing to ~ 1, and ensures a small number of primary vertices per event. This is desirable since it makes it easier to identify the displaced vertices that are a characteristic of B-meson decays. To reduce the number of multiple interactions in one event (pile up events) a dedicated detector, upstream of the interaction point, vetoes bunch crossings with more than one interaction.

The subdetectors of LHCb can be divided into two main classes depending on their tasks. The tracking system consists of the Vertex Locator (VELO), the Tracker Turicensis (TT), and the tracking stations T1-T3. The tracking stations T1-T3 are actually two subdetectors: the Inner Tracker (IT) and the Outer Tracker (OT). The tracking system reconstructs particle trajectories across the detector. By using the curvature of the tracks in conjunction with the known magnetic field provided by the dipole magnet, the momenta of the particles are reconstructed. Moreover, the tracking system provides primary and secondary vertex information. The particle identification (PID) system includes three subdetectors: the Ring Imaging Cherenkov detectors (RICH1 and

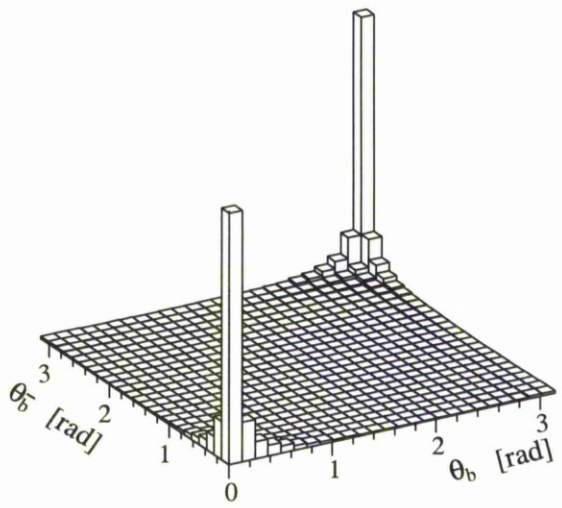

Figure 4.4: The polar angle distribution of the $b\bar{b}$ pairs produced at a centre of mass energy of 14 TeV as generated by the PYTHIA event generator

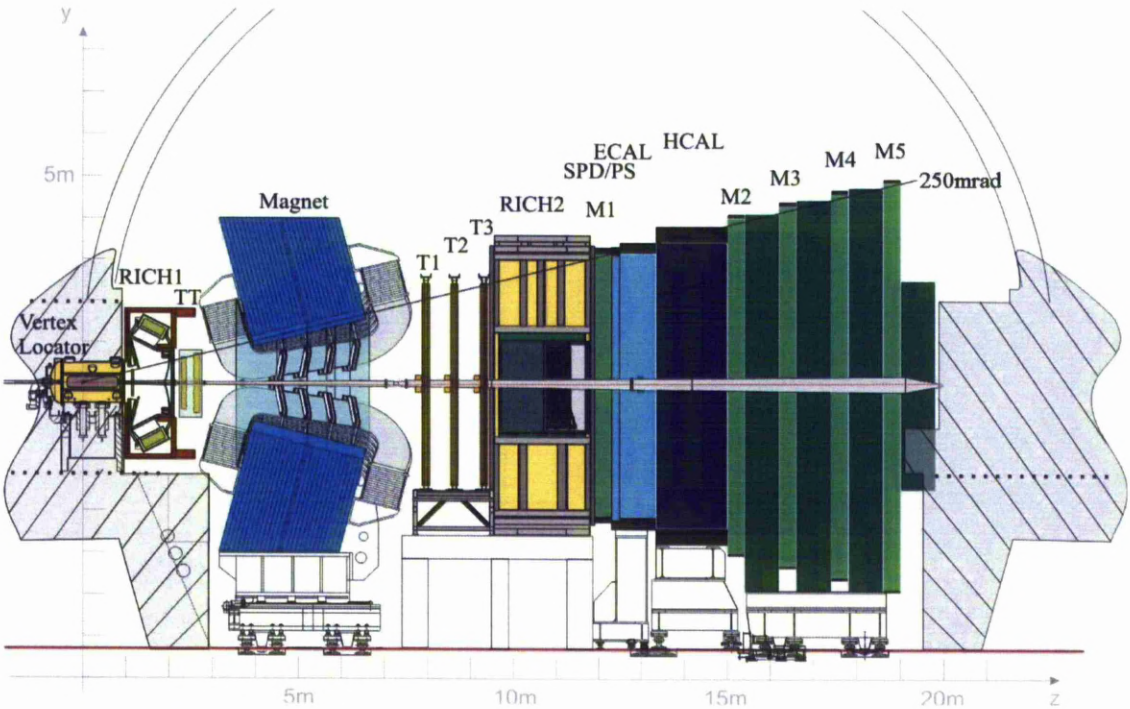

Figure 4.5: A cross section of the LHCb experiment in the y-z plane. The interaction point is located inside the VELO

RICH2) provide K/π separation, the electromagnetic and hadronic calorimeters (SPD, PS, ECAL and HCAL) provide e^-/γ separation and hadron identification. The muon chambers perform muon identification. A short description of the individual subdetectors, the track reconstruction and the particle identification method are given in this chapter.

4.3.1 The Tracking System

Vertex Locator

The Vertex Locator (VELO) [32], is a silicon microstrip detector positioned around the interaction region. The sensors are 300 μm thick *n-in-n* sensors and are arranged in 23 consecutive planes, perpendicular to the beam axis. By the use of two types of strip geometries, the radial and azimuthal coordinates of traversing particles are measured. With its active area beginning at 8.2 mm from the interaction region, the VELO provides precise measurements of track coordinates, which are used to reconstruct the primary vertex as well as displaced secondary vertices that are characteristic of B-meson decays. Two of its stations make up the so-called Pile-up Veto detector. They are used in the first level trigger (L0) to reject bunch crossings with multiple interactions. The VELO detector is described in detail in Chapter 5.

The Silicon Trackers

The Silicon Trackers (ST) are the Tracker Turicensis (TT) [33], and the Inner Tracker (IT) [34]. The TT is positioned before the magnet and the IT is positioned after the magnet. A view of the TT, and IT is shown in Figure 4.6 and Figure 4.7.

The TT is a silicon microstrip detector using 500 μm thick *p-in-n* sensors, arranged in four layers, covering the full LHCb acceptance. The four planar detection layers of the TT are shown in Figure 4.6. The first and the fourth layers have vertical readout strips, measuring hits in the x-axis and are called x layers. The second and the third layers have readout strips rotated by a stereo angle of +5 ° and -5 °, these layers are called u and v layers. The arrangement of the layers (x,u,v,x) with a stereo angle reduces ambiguities between hits. The sensors have a strip pitch of 183 μm, and have a resolution of $\sim 50\mu$m.

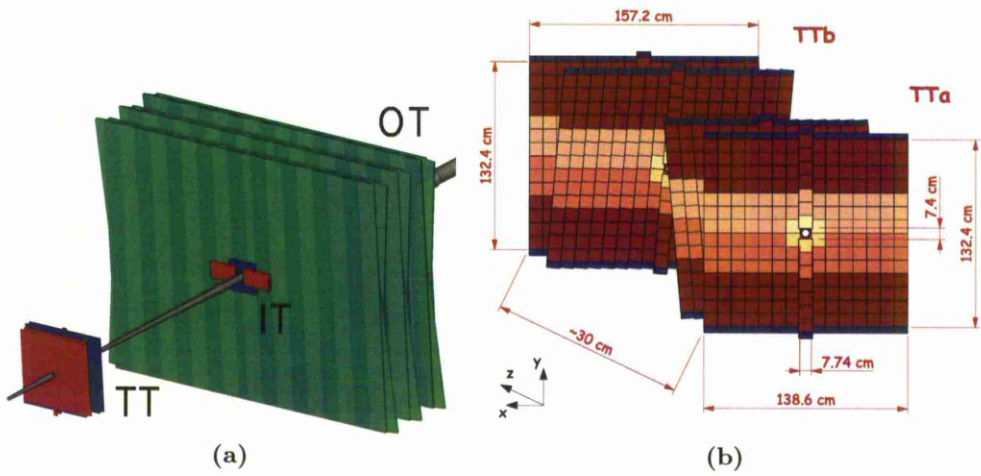

Figure 4.6: (a) A perspective view of the OT, IT and TT.(b) The four layers of the TT. The middle layers (the u and v layers) are rotated by $\pm 5^\circ$ around the x axis, giving the strips a stereo angle.

The Inner Tracker (IT) is a *p-in-n* silicon microstrip detector, with three stations arranged around the beam pipe in the tracking stations T1-T3 where the particle flux is too high to use the straw tube technology of the OT.Each station consists of two planes of one sided silicon microstrip sensors with vertical readout strips, and a further two planes rotated by a stereo angle of $\pm 5^\circ$. The design and dimensions of the x and u layers of the IT are shown in Figure 4.7. The IT layers have the same (x,u,v,x) arrangement as the TT. To satisfy the signal to noise requirements of the experiment, two types of sensors of 320 μm and 410 μm thickness are used. The sensors have a strip pitch of 198 μm giving a resolution of $\sim 50\mu$m. In contrast to the TT, the IT does not cover the full angular acceptance the rest of the acceptance is covered by the Outer Tracker.

Outer Tracker

The Outer Tracker (OT) [35] is a straw-tube detector surrounding the IT tracking stations. It measures drift times in straw tubes to determine the position of a charged particle. To ensure a fast drift time (~ 50 ns) and a resolution of ~ 200 μm, a combination of Argon (70%) and CO_2 (30%) is used. Each station consists of four layers in the same (x,u,v,x) orientation as the ST. The modules that make up an OT layer consist

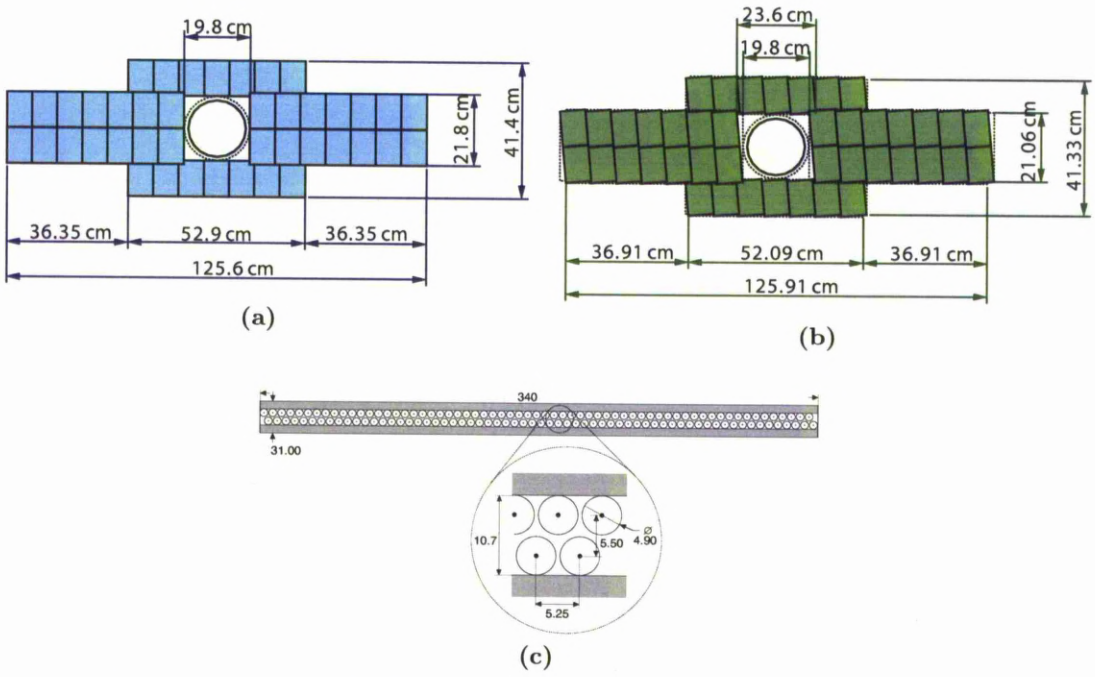

Figure 4.7: (a) The x layers of an IT station. (b) The u layers of an IT station. (c) An OT module illustrating the staggered monolayers, dimensions are in cm.

of two staggered monolayers with 5 mm diameter straw-tubes, illustrated in Figure 4.7. The OT extends to cover the full outer angular acceptances of LHCb.

4.3.2 Track Reconstruction

The trajectories of particles traversing the LHCb detector are reconstructed by combining tracks in the tracking detectors. The tracking algorithms begin by reconstructing tracks in the VELO, to find VELO seed tracks. The VELO seed tracks are reconstructed by matching three dimensional space points known as VELO hits. The VELO hits are created by combining R and Φ clusters, which are fitted to straight lines to hits in at least three VELO modules. Seed tracks are also found in the T stations where the magnetic field is low. Once the track seeds are found they are refitted using a Kalman filter method [36][37].

Five classes of tracks are defined [38] as illustrated in Figure 4.8. The long tracks are reconstructed from measurements in all tracking detectors and have the best momentum resolution. Upstream tracks are typically low momentum tracks that only traverse

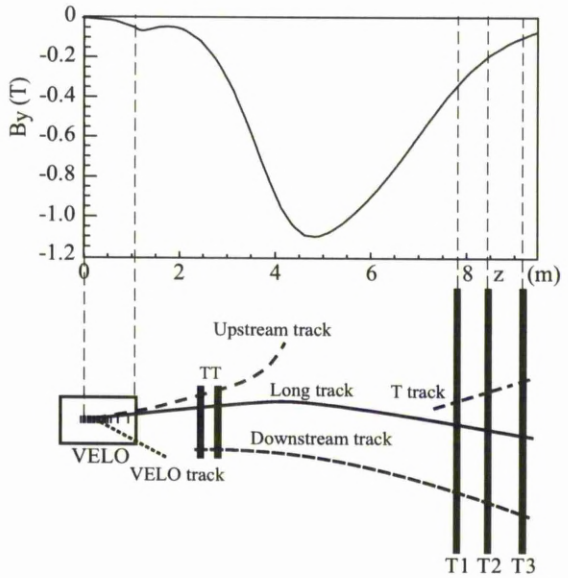

Figure 4.8: The variation in the magnetic field strength between the VeLo and T1-T3 tracking station and an illustration of the five classes of tracks.

the VELO and TT before being bent out of the detector acceptance by the magnetic field. Downstream tracks only traverse the TT and T stations. These are typically decay products of particles decaying outside the VELO acceptance or with insufficient VELO hits to be reconstructed. T tracks are only measured in the T-stations and are typically produced in secondary interactions or are low angle tracks that are bent into the acceptance by the magnetic field. Finally, VELO tracks only have hits in the VELO due to a large or backwards production angle. These VELO tracks are used mainly for primary vertex reconstruction.

4.3.3 Particle Identification

RICH

The identification of hadrons, and in particular the separation of pions and kaons is important for the performance of LHCb. This is particularly important for B decays which have hadronic particles in the final states, allowing differentiation between decays with identical topologies. The Ring Imaging Cherenkov (RICH) [39] detectors are designed for this purpose. LHCb has two RICH detectors, RICH1 is located between the VELO and the TT, RICH2 is located after the OT. Figure 4.9 shows the design of the two

RICH detectors. RICH1 covers the full angular acceptance of LHCb, whereas RICH2 has a reduced angular acceptance but covers the region where high momentum particles are produced. The principle behind the operation of the RICH detectors is the process of Cherenkov radiation. Cherenkov light is produced when charged particles traverse a medium with a speed greater than that of the speed of light in that medium. The polar angle θ_c at which the Cherenkov light is emitted is given by the relation;

$$cos\theta_c = \frac{1}{n\beta} \tag{4.1}$$

where n is the refractive index of the medium, and $\beta = v/c$, where v is the velocity of the particle and c is the speed of light. The RICH detectors determine the velocity of the particle by measuring the angle θ_c, this information combined with the momentum information from the tracking system allows the mass of any charged particles entering the detector to be measured. The RICH detectors cover a momentum range between 1-100 GeV/c, this is achieved by using three different mediums, called radiators. RICH1 has two radiators aerogel, and C_4F_{10}, and RICH2 has one radiator CF_4. The characteristics of the different radiators used are summarised in Table 4.2, and Figure 4.10 shows the Cherenkov angle as a function of particle momentum for the RICH radiators.

Radiator	n	θ_{max} (mrads)	Momentum range (Gev/c)
Aerogel	1.03	242	1-15
C_4F_{10}	1.0014	53	10-60
CF_4	1.0005	32	15-100

Table 4.2: A summary of the RICH radiator characteristics, θ_{max} occurs when $\beta = 1$.

The Cherenkov light, is reflected out of the detector acceptance by the use of spherical and flat mirrors, and focused onto Hybrid Photon Detectors (HPDs). In the HPDs, the incident photons are converted into photoelectrons which are detected by an array of 1024, 500 μm $\times$ 500 μm large silicon pixels. The measurements in the HPDs are combined to reconstruct rings, the radii of which are measures of the Cherenkov emission angles of the traversing particles.

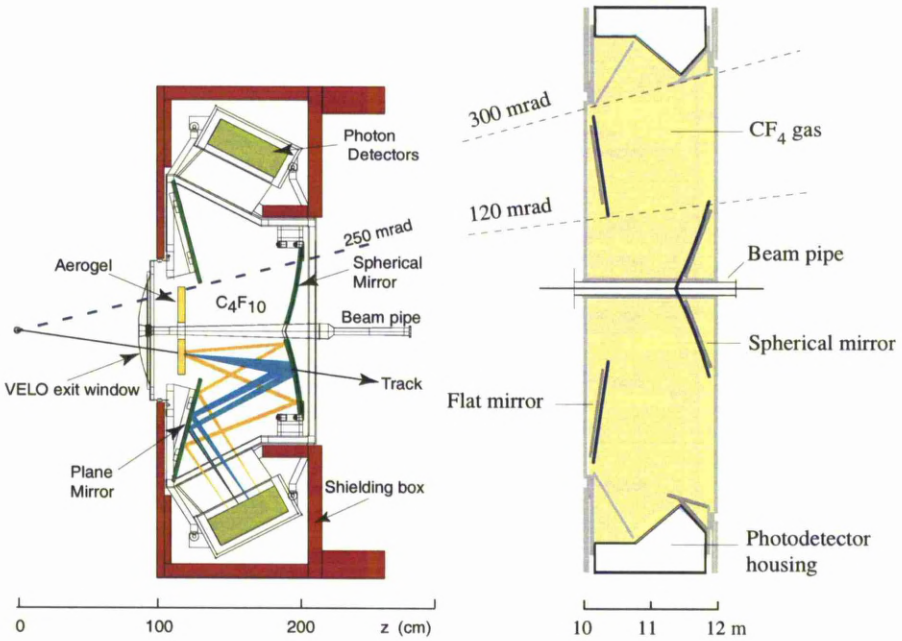

Figure 4.9: Side view of RICH1 (left) and RICH2 (right).

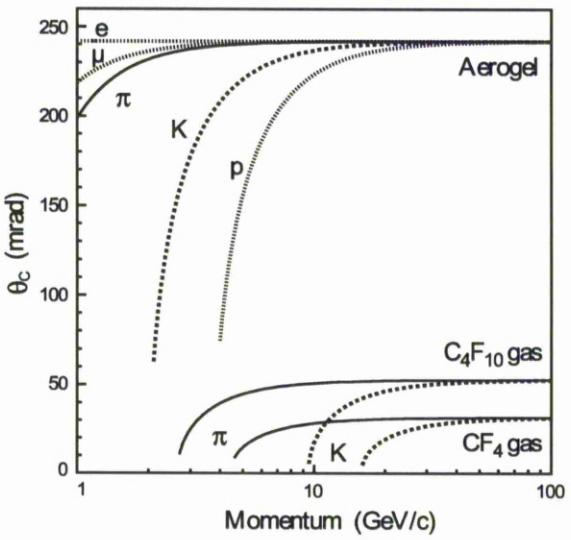

Figure 4.10: Cherenkov angle as a function of momentum for different particles and radiators.

Calorimeters

The four calorimeters [40]are located between the muon stations M1 and M2. These are the electromagnetic calorimeter (ECAL), the hadron calorimeter (HCAL), the preshower detector (PS) and the scintillator pad detector (SPD). They are designed for particle identification, as well as their primary function of energy and position measurements. The calorimeters provide information to the Level 0 trigger (L0), which relies heavily on their ability to select photon, electron and hadron candidates with high transverse energy (E_T).

The SPD, consists of a 15 mm thick scintillator plane, and is used to differentiate between charged and neutral particles. The PS is a layer of 15 mm thick scintillator pads and is separated from the SPD by a 12 mm thick lead wall known as the lead converter. The PS is used to separate electrons and photons using the topology of electromagnetic showers subsequently measured in the ECAL. The light signals from the SPD and PS are collected via wavelength shifting fibres (WLS), and transmitted to photomultipliers and readout.

Both ECAL and HCAL work with a similar principle, incident particles interact with the absorber material (lead in HCAL and iron in ECAL) and create a shower of secondary particles. These particles then induce light as they pass through scintillators, which are readout using WLS fibres, and the amount of light collected is proportional to the energy of the incident particle. The ECAL collects the full shower for all electrons and photons and the HCAL absorbs the energy from all the hadrons

The energy resolution for the ECAL [27][41] follows the following relationship:

$$\frac{\sigma(E)}{E} = \frac{\mathrm{a}}{\sqrt{E}} \oplus \mathrm{b} \oplus \frac{\mathrm{c}}{\mathrm{E}} \tag{4.2}$$

where E is expressed in GeV and $\oplus$ means addition in quadrature and $8.5\% < \mathrm{a} < 9.5\%$, b $\sim 0.8\%$ and c is the noise ~ 0.1. For the HCAL [27][42] the resolution is:

$$\frac{\sigma(E)}{E} = \frac{(69 \pm 5)\%}{\sqrt{E}} \oplus (9 \pm 2)\% \tag{4.3}$$

Muon System

The muon system [43]-[44]consists of five stations (M1-M5) of rectangular shape positioned downstream of the RICH2 detector with the calorimeters located between M1 and M2. Two detector technologies are employed; Multi Wire Proportional Chambers (MWPC) and Gas Electron Multipliers (GEM). MWPC detectors are used in every region of all the muon stations except for the innermost region of M1. In this region the expected particle flux is too high and where triple GEM detectors are used instead. Iron absorbers are interleaved between stations M2-M5 and behind M5. They remove hadronic backgrounds and shield the muon detector from particles that have strayed from the LHC beam. The muon system is used in the L0 trigger to select events with muons of high transverse momentum (p_T) and in the high-level trigger (HLT) and offline analysis for muon identification.

4.3.4 Particle Identification methods

The information from the RICH detectors, the calorimeters and the muon system is combined for the identification of charged particles (e,μ,π,K,p). The ECAL, SPD and PS are used to identify neutral particles (π^0,γ). The RICH detector provides most of the information used for PID in LHCb. Other detectors also contribute information to help make the best decision possible. The RICH uses a log likelihood method approach[45], to match the observed pixel hits in the RICH to those expected from reconstructed tracks. The likelihood is maximised by varying the particle hypothesis of each track in turn through electron, muon, pion, kaon, and proton. Using this method, over the full momentum range, an efficiency of about 95% was found for reconstruction of kaons. This produced a misidentification rate to pions of about 5%. Methods have also been developed to find rings without the use of tracks. This provides an alternative method of assessing the performance of the RICH and this is discussed further in [46].

4.3.5 The LHCb Trigger

The role of the trigger is to efficiently select events of interest for analysis. The frequency of visible interactions in LHCb is expected to be 10 MHz, with a rate of only 100 kHz containing $b\bar{b}$ pairs. Approximately 15 % of these $b\bar{b}$ pairs will be suitable for analysis, this is due to the fact that both the B-meson and its decay products have to lie within

the LHCb acceptance. The LHCb experiment employs a three tier triggering system to reduce the selected event rate from 10 MHz to 2 kHz. A flow diagram illustrating the functions of each part of the trigger is shown in Figure 4.11.

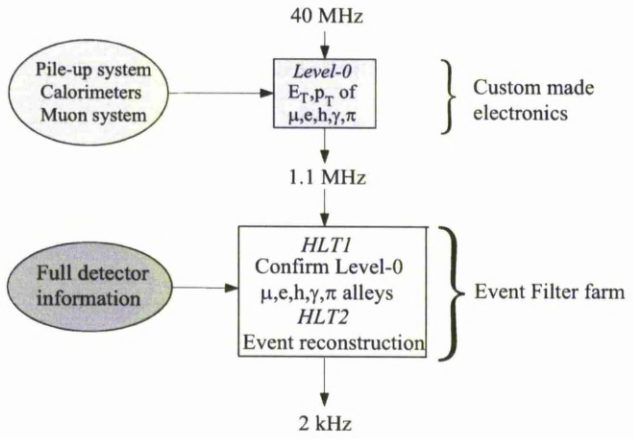

L0 criteria

μ_1	p_T	> 1.3 GeV/c
$\mu_1+\mu_2$	p_T^{total}	> 1.5 GeV/c
h	E_T	> 3.5 GeV
e	E_T	> 2.6 GeV
γ	E_T	> 2.3 GeV
π^0	E_T	> 4.3 GeV

Figure 4.11: Left: Overview of the trigger system. Right: L0 trigger criteria for nominal luminosity

Level-0 Trigger

The Level-0 (L0) trigger [47] operates at 40 MHz synchronous with the LHC clock. It has an input rate of 10MHz at a luminosity of $2x10^{32}cm^{-2}s^{-1}$, and an output rate of 1MHz, which is performed by custom made electronics on the calorimeter, muon and pile up systems.

The Level 0 trigger uses custom electronics to make decisions on the suitability of events. The system has an inbuilt latency of 4μs, after including time of flight of particles, cable delays and front end electronics. This leaves only 2 μs to process and make a decision.This means that the front-end electronics must store 160 events in memory while the L0DU makes a decision.

The pile-up system aims to distinguish between single and multiple interactions. It provides primary vertices candidates along the beam line and a total backward track multiplicity. The calorimeter trigger system looks for particles with large transverse energy (E_T). It also identifies them as electron, photon or hadrons, based on information from the SPD, PS, ECAL and HCAL. The total E_T of the HCAL is used to reject crossings without visible interactions and muons from the halo. The number of SPD cells hit is used to provide a measure of multiplicity. The muon trigger selects the

two muons with the highest p_T from each quadrant, assuming the track is from the interaction point, to estimate the momentum. All this information is then passed to the Level 0 decision unit which combines all the information and provides a decision for all crossings.

High Level Trigger

The High Level Trigger (HLT), is a C++ algorithm that runs on a cluster of 2000 CPUs. It has access to the full event information from all subdetectors and its purpose is to reduce the 1.1 MHz input rate from L0 to a 2 kHz output rate at which events are stored for offline analysis. To meet the time limitations imposed by this requirement, the HLT has two stages, HLT1 and HLT2.

In HLT1 the events are sorted into different "alleys" that each address one of the L0 trigger types. Depending on the L0 trigger type, events may enter multiple trigger alleys. The events are partially reconstructed to such an extent that the majority of the uninteresting events are rejected. The primary vertex position is reconstructed using 2D Rz-tracks in the VELO. The impact parameter of a track with respect to the primary vertex is a powerful discriminator for B events and used in many of the alleys. HLT2, operates at an event rate of approximately 30 kHz. It performs a full reconstruction with information from all subdetectors and makes the final trigger selection.Figure 4.12 illustrates the trigger flow from L0 via HLT1 and HLT2 to storage.

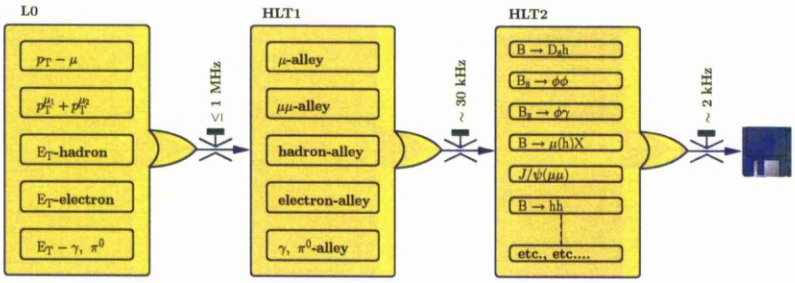

Figure 4.12: Flow diagram of the various sequences in the trigger.

4.4 Summary

LHCb is one of the four experiments at the LHC. It is designed to study CP violation, and rare decays in the B-sector. LHCb is comprised of six subdetectors each providing

tracking information or particle identification. The trigger is used to efficiently select events of interest for analysis, and reduces the event rate from 10MHz to 2kHz. LHCb is now running and taking data, with all of the systems running as expected. The next chapter describes in greater detail the LHCb VELO subdetector, which is the silicon tracking and vertexing detector of LHCb.

Chapter 5

The LHCb Vertex Detector

The Vertex Locator (VELO), is the primary tracking and vertexing detector for LHCb. The VELO provides precise measurements of the track coordinates close to the interaction region. These tracks are used to reconstruct primary vertices, and identify the displaced secondary vertices that are a distinct feature of beauty and charm hadron decays. In addition, the tracks are used to provide accurate measurements of the decay lifetimes of B-hadron and C-hadrons, and to measure the impact parameter of the particles used to tag their flavour. To achieve this, the VELO design is driven by the requirement of high position resolution on the reconstructed track parameters. Due to these requirements the VELO has silicon microstrip sensors that are positioned at a radial distance of 8.2 mm of the LHC beams. This results in the VELO operating in an extreme and non-uniform radiation environment. Radiation hard detector technologies are utilised in the design of the VELO sensors to extend their lifetime.

5.1 Detector Overview

The VELO consists of 21 stations each containing four sensors, arranged in two halves, perpendicular to the beamline covering the full angular acceptance of LHCb. The pile up detector consists of two stations with two sensors each. Each station contains two modules, staggered in z, and mounted opposite to each other in their respective detector halves. The layout is shown in Figure 5.1. Each module contains two silicon sensors that provide r (R-sensors) and ϕ (Φ-sensors) coordinates of the tracks, glued back to back and mounted on a Printed Circuit Board (PCB), called a hybrid, with associated readout electronics. The hybrid is mounted on a carbon fibre pedestal. The stations are placed

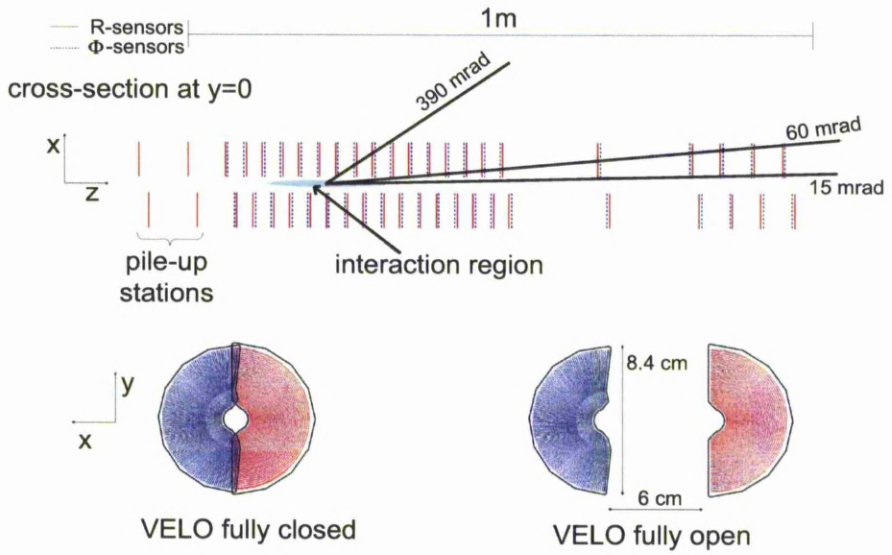

Figure 5.1: A crosssection of the VELO sensors in the xy plane, indicating the angular acceptance and the arrangement of the stations. The drawing below shows a VELO station in the open and closed positions.

at a distance of 7 mm from the beam axis, with the first active strip at a radial distance of 8.2 mm. This is to minimise the track extrapolation distance to the interaction point, which gives an improved impact parameter resolution. The radial distance of the VELO stations from the beam axis is smaller than the aperture required by the LHC during injection. This means that the VELO is required to be retracted by 30 mm during injection. The proximity of the VELO sensors also requires that the VELO is integrated into the LHC vacuum system, and shielded against RF pickup from the beams. To satisfy this requirement the VELO is housed in a secondary vacuum vessel which is shown in Figure 5.2. The vacuum vessel separated the LHC vacuum ($\sim 10^{-9}$mbar) from the VELO vacuum ($\sim 10^{-7}$mbar) with 300 μm thick aluminium boxes (RF boxes). Figure 5.3 shows the RF foils and the module supports and the accompanying RF box. The RF boxes are expected to deform at a differential pressure of 20 mbar, this means that the difference in pressure between the primary and secondary vacuums needs to be constantly monitored. The sensors are mounted in the vacuum vessel in such a way that the sensors overlap in the closed position. The aluminium foil of the RF boxes is corrugated to accommodate the overlapping sensors, this is shown in Figure 5.3.

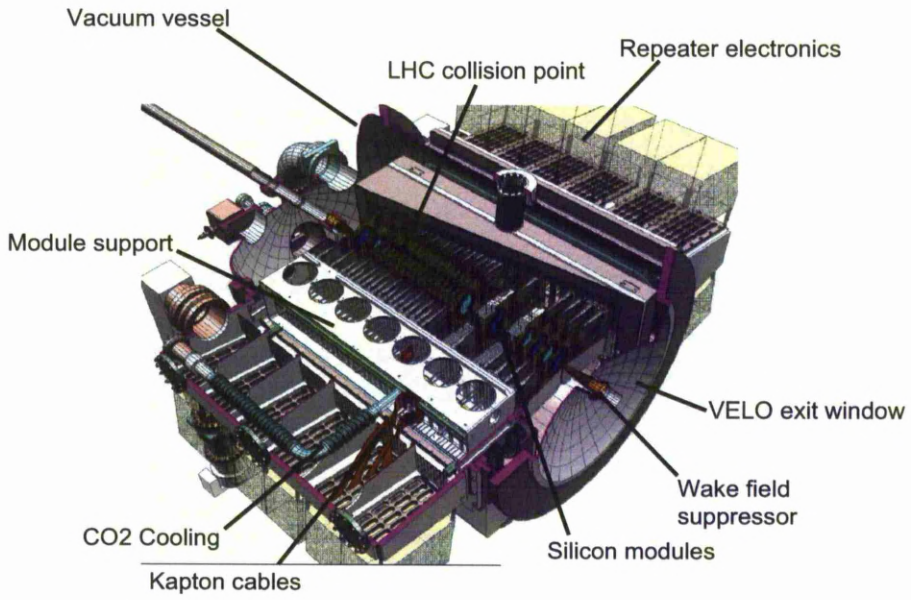

Figure 5.2: The VELO vacuum vessel.

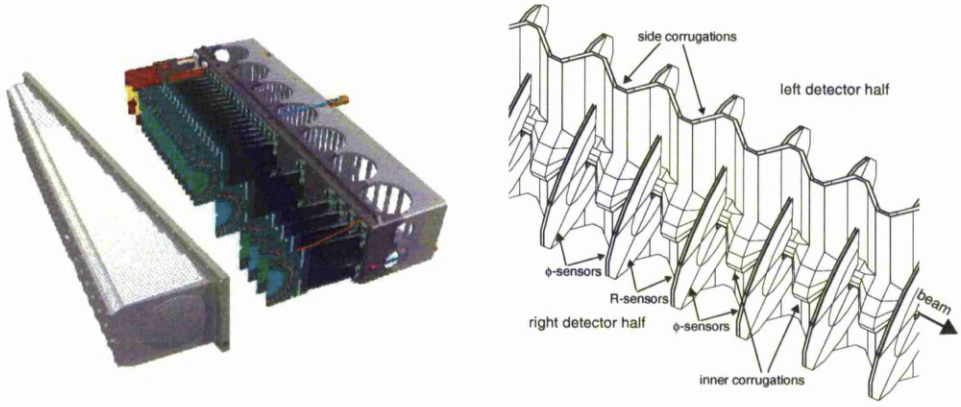

Figure 5.3: Left: The modules in one detector half and the RF box that surrounds it. Right: A zoom in on the inside of the RF foil, with the detector halves in the closed position. The edges of the box are cut away to show the overlap with the staggered opposing half.

The detector is cooled using a two phase CO_2 system [48], that is capable of temperatures between of -5 ° and -10 °C at the sensors. Cooling blocks are screwed onto the modules, that are thermally connected to cooling capillaries which are used to distribute the CO_2. The cooling is required to limit the effects of radiation damage, and to prevent the electronics overheating in the vacuum. To control the annealing of the sensors, they are continuous cooled after irradiation. The aim is to limit the exposure of irradiated sensors to room temperature to less than one week per year.

5.2 Silicon Sensors

The VELO sensors are single sided, 300 μm thick, AC coupled devices. They are biased using 1.8 MΩ polysilicon resistors and have an implanted guard ring structure. They have a semicircular shape covering a 182° angle, including a 2° overlap area with the opposite sensor in the vacuum tanks. Due to the harsh radiation environment at the VELO; the sensors are radiation hard, oxygen enriched *n-in-n* sensors with p-spray strip isolation. Each sensor is read out via 2048 aluminium strips and the signal is routed to the readout chips using a second metal layer. The second metal layer is insulated from the strips by approximately 3 μm of SiO_2. The second metal layer is connected to the first metal layer by wet etched vias. The sensors in one VELO module are manufactured using *n-in-p* diode configuration. The full replacement VELO detector, which has been produced to replace the VELO in case of severe reduction of performance due to radiation damage or beam accidents has been constructed using *n-in-p* silicon sensors.

There are two types of sensors, R-sensors provide radial information, and Φ-sensors measuring the azimuthal angle. The strips in an R-sensor are divided into four segments each having 512 concentric circular strips. Segmenting the R-strips in this way minimizes the occupancy in each strip, and reduces the strip capacitance. The R-strips have pitch of 38 μm at the inner radius of 8.2 mm and the pitch increases with radius to 102 μm at the outer radius of 42 mm. The strips in a Φ-sensor are divided into inner and outer regions, with 683 and 1365 strips respectively. The Φ-strip pitch in the inner region ranges from 38-78 μm, and in the outer strips from 39-97 μm. The Φ-strips are skewed, in the inner region the strips have an angle of $\sim 30°$ to the radial at a radius of 8.2 mm from the beam, the outer strips have an angle of $\sim 10°$ to the radial at a radius of 17.25 mm. The skew of the inner and outer strips in a Φ-sensor is reversed, giving the strip a dog-leg. Modules are placed so that adjacent Φ-sensors have the opposite skew

with respect to each other. This creates a stereo angle between the strips and ensures that adjacent stations are able to distinguish ghost hits from true hits. The layout of the strips on the sensors is shown in Figure 5.4, and Table 5.1 summarises the main characteristics of the VELO sensors.

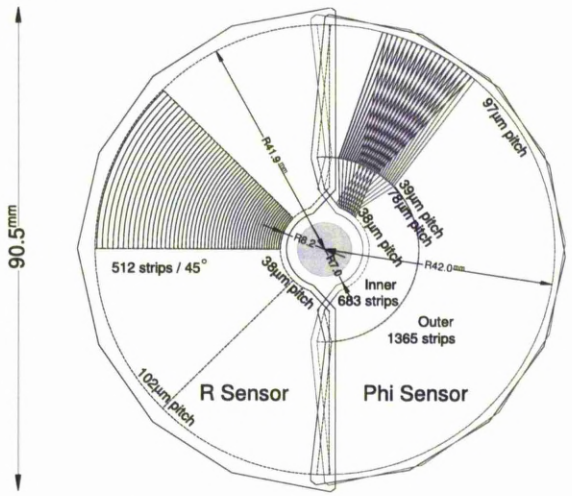

Figure 5.4: A view of the R and Φ sensors in the x-y plane. The R/Φ geometry is illustrated, and for clarity only a portion of the strips are drawn. In the ϕ sensor, the strips on two adjacent sensors is drawn to highlight the stereo angle. The different arrangement of bonding pads leads to a slightly larger radius for R-sensors. The sensitive areas are identical.

5.3 Detector Modules

The main components of a module are, the silicon sensors, the hybrid, and the paddle. The VELO modules [49] hold the sensors in a fixed position relative to the module support, and enable readout and thermal management of the modules. Figure 5.5 shows a diagram of the module components, and a photograph of a completed VELO module.

The hybrid consists of a 1.5 mm substrate made from 400 μm thick thermal pyrolytic graphite (TPG), encased in Carbon Fibre (CF) of thickness 250 μm, on to which two electrical circuits are laminated. The hybrid substrate has a semi circular hole where the sensors are located. The silicon sensors are glued back to back onto the double sided hybrid. Each circuit has 16 front end readout chips that are connected to the sensors by double layer kapton pitch adapters. Pitch adapters are required because the bonding pad pitch on the sensors is different to the pitch of the readout chips. The temperature of the

	R Sensor	ϕ Sensor
Number of Sensors	42 +4 (pile-up)	42
Readout Channels per Sensor	2048	2048
Sensor Thickness	300 μm	300 μm
Depletion Voltage (unirrad)	20-70 V	20-70 V
Smallest Pitch	40 μm	38 μm
Length of Smallest Strip	3.8 μm	5.9 μm
Length of Longest Strip	33.8 μm	24.9 μm
Inner Radius of Active Area	8.2 mm	8.2 mm
Outer Radius of Active Area	42 mm	42 mm
Strip Width	0.4 $\times$ pitch	0.4 $\times$ pitch
Angular Coverage	182°	182°
Stereo Angle	-	10-20°
Average Occupancy	1.1%	Inner: 1.1% Outer 0.7%
Bias Resistor	1.8 MΩ	1.8 MΩ

Table 5.1: Principal characteristics of the VELO sensors.

hybrid can be measured using negative temperature coefficient (NTC) sensors, of which there are two per hybrid. The populated hybrid is glued to the low mass CF paddle; which has Invar feet. The paddle is used to mount the module onto the detector base plate. Invar is used for the feet, because it has a low coefficient of thermal expansion.

5.4 The Beetle Readout Chip

The Beetle is a custom designed radiation hard readout chip used in the VELO [50]. The Beetle is desgined in 0.25μm CMOS integrated circuit technology and can withstand a total radiation dose in excess of 130Mrad. The peak time and sampling rate of the Beetle have been designed to match the LHC bunch crossing rate of 40 MHz, and it can accept a trigger rate of up to 1 MHz. The Beetle can be operated in analogue or binary mode. A schematic diagram of the Beetle is shown in Figure 5.6.

A Beetle chip reads out 128 channels of a VELO sensor, to charge sensitive amplifiers. The charge is converted into a voltage pulse shape which can be adjusted by manipulating the input voltages and currents. The Beetle reference manual [50] defines the

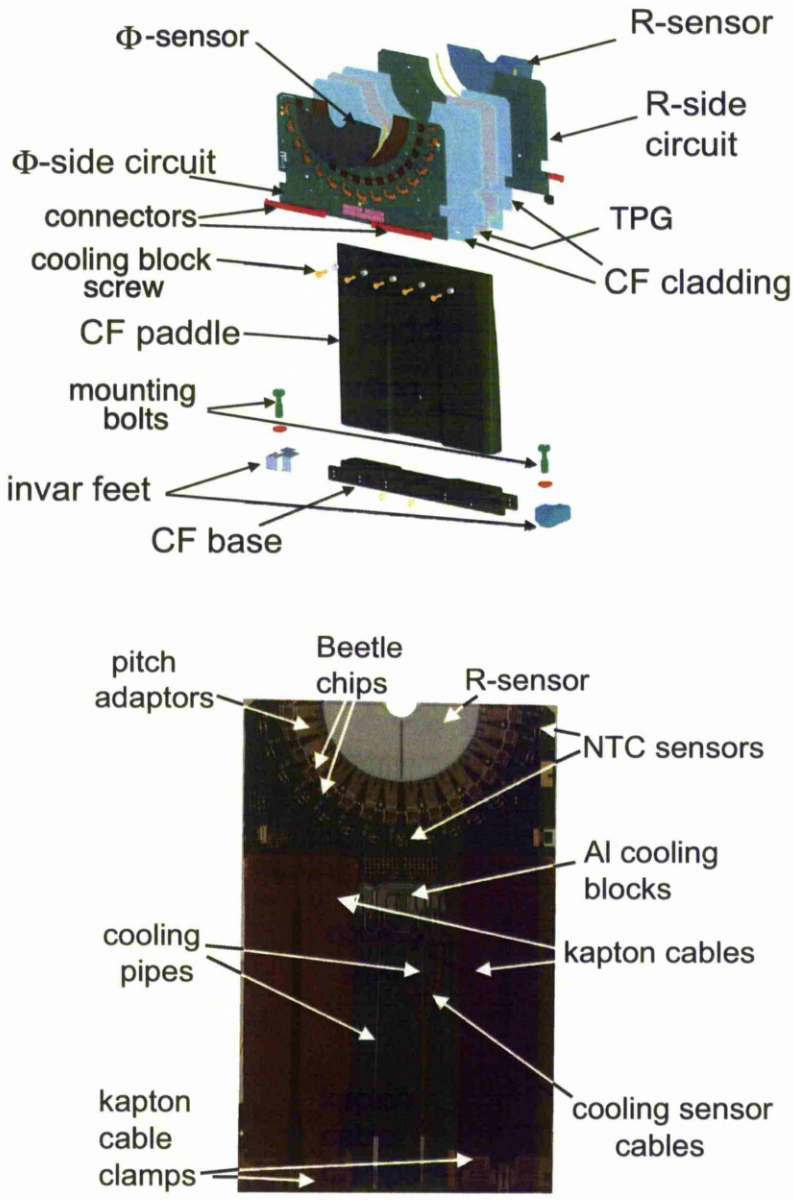

Figure 5.5: Top: Diagram of a VELO module and its components. Bottom: Photograph of a completed VELO module.

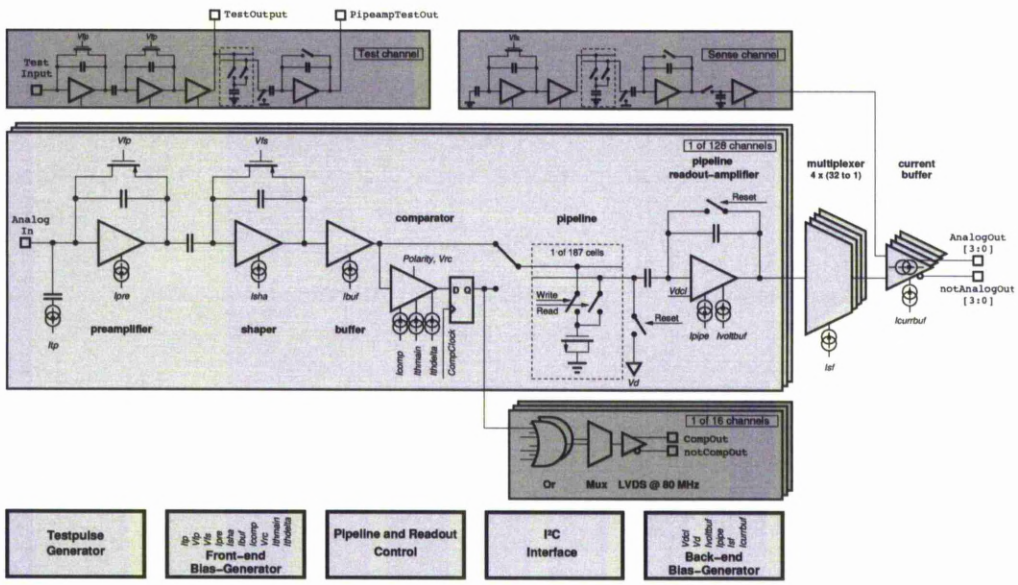

Figure 5.6: A schematic block diagram of the Beetle readout ship.

specific thresholds and defaults for each of these inputs. The equivalent noise charge for the analogue front-end is $497e^{-}$ + 48.3e/pF C_{in}, where C_{in} is the capacitance at the input. The output of the shaper is sent through a buffer which repeats the signal to a comparator. In binary mode the comparator discriminates the signal and sends the digital output over 80MHz low voltage differential signal lines (LVDS). In analogue mode the signals are propagated to the analogue pipeline at 40MHz. The pipeline has 187 cells for storing the signals for a maximum latency of 160 sampling intervals (4μs) and a 16 stage multi-event buffer. The stored signals are read out to a 32-to-1 multiplexer via the pipeline amplifier (pipeamp). A dummy channel is used to compare and subtract common mode effects. Current drivers send the serialised data off-chip. Control signals are read in via an I^2C interface[1] and the bias voltages and set via on-chip Digital-to-Analogue Converters (DAC's). The Beetle can also inject an test charge onto each channel for the purposes of testing and calibration.

The Beetle pulse shape is semi-gaussian as shown in Figure 5.7. The characteristic parameters defining the shape are as follows: (i) The peaking time t_p - the time taken for the pulse to reach its maximum amplitude from its baseline; (ii) the rise time t_r - the time taken from 10% above the baseline to 10% below the peak amplitude (the rise time is often easier to measure than the peak time as it is difficult to measure the exact start of the pulse); (iii) the peak amplitude V_p; and (iv) the remainder (or spillover) R,

[1] Inter-IC or I^2C, a control and power management bus.

the fractional amount of charge left 25ns after the peak (assuming readout samples on the peak). The Beetle is designed to have a maximum rise time of 25ns and a spillover of less than 30%. An undershoot is also shown on the right-hand side of the figure as the pulse dips below its baseline after the peak. This undershoot is strongly affected by the pulse shaping parameters. The time for the pulse to return to its baseline voltage is known as the baseline restoration time, and it determines how quickly consecutive pulses can be read out without grossly interfering with each other.

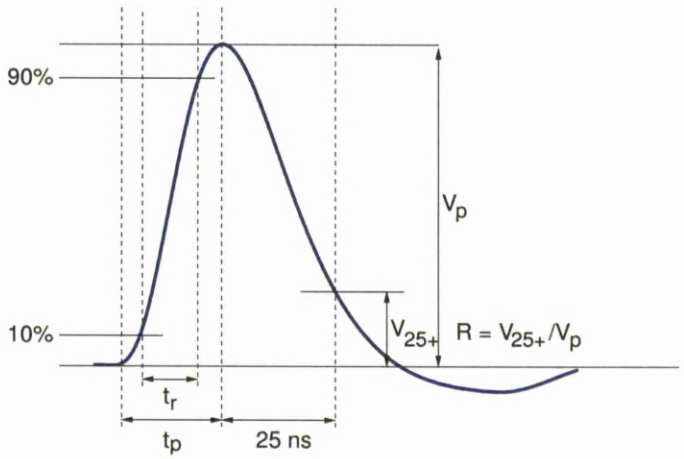

Figure 5.7: Beetle pulseshape.

Each Beetle chip has 128 input channels connected to VELO strips which are sent out on four analogue links when an accept signal is received from the L0 trigger. Each analogue link sends out 32 channels of analogue data this is preceded by four bits of header data. The header data is digital information. The four bits provide information on the status of the front-end chips and encode the pipeline column number (PCN)[2]. The pipeline column number is the position in which the data is stored in the Beetle pipeline that holds the data while waiting for the L0 trigger decision.

5.5 The High Voltage and Low Voltage Systems

The low voltage system (LV) [51], provides low voltage power to the VELO hybrids, and the repeater boards. The system is based on a multi channel power supply system manufactured by CAEN. The power supplies are installed in the counting house, behind

[2]There are 16 header bits in total. 4 bits on each link, and 4 links per Beetle. 8 bits are used to encode the PCN.

the shielding wall. Each module has 12 fully floating channels and can supply four repeater boards. Each channel has its own voltage sense line to permit a correction to be made for any voltage drop across the long distance cables. The repeater boards require three voltages which are supplied over shielded twisted pairs. The LV power supplies interface to the hardware interlock system.

The high voltage system (HV) [52][53] , provides high voltage power supply to the sensors. Due to radiation damage the sensors will operate under a reverse bias of between 100V-500V. The required bias voltage will increase with radiation damage. The biasing scheme ties the n^+ strips to ground, and applies a negative voltage on the backplane. The HV system utilises six power supply modules, manufactured by ISEG, and each module supplies sixteen sensors. The modules are housed in an un-interruptible power supply crate in the counting house. The output of the modules is fed via 37-core cables to a patch panel in the counting house. Long 57-core cables connects the counting house patch panel to another patch panel near to the detector. The high voltage, high voltage guard, and ground are provided to the repeater board of each module by 3-core cables. The HV system supplies an interface to the hardware interlock system.

5.6 The Hardware Interlock System

The VELO is protected with a simple and failsafe hardware interlock system. An overview of its functionality is given in [54]. The interlock system is the last safety mechanism in case of failure. Switching on the low voltage when the VELO is not properly cooled is prevented by this system. The status of the cooling, vacuum, motion and detector front-end systems and the beam conditions monitor (BCM) are combined in an interlock logic unit and fed back to high and low voltage systems and to the motion and cooling system. All input signals are continuously monitored and their status shown on the front panel LEDs. The inputs are fail safe such that any disconnection or power loss will result in a bad status and the interlocks will fire. Any of the inputs may additionally be forced to a good status by internal switches for debugging or override purposes, and this is also indicated on the front panel. The interlock outputs are also fail safe such that cable removal or power failure will result in module power and cooling being removed. The status of the outputs is shown on the front panel and all individual outputs can be overridden by internal switches. Hardware signals are also exchanged between the motion, cooling and vacuum systems. As the VELO cannot be allowed to move in

while the LHC beam is not stable, beam inhibit and beam status signals are exchanged with the BCM and the LHC beam interlock system. Direct signals from the LHC sector valves and the neon injection system are given to the VELO vacuum system to prevent venting, evacuating or neon injection when one of these systems is not ready.

5.7 The VELO Data Acquisition System

5.7.1 Detector Readout

When an ionising particle traverses the VELO sensors, a signal is induced at the electrodes. The analogue signal is routed through the second metal layer to the Beetle chips, which are placed around the edge of the sensor. After the L0 accept signal, the data is transmitted along a short kapton cable connecting the hybrid to a fixed connector. The signal is then sent along a long kapton cable from the connector to the feed through on the vacuum vessel. The signal is then sent to the repeater boards house immediately outside of the VELO tank. A diagram of the VELO DAQ is shown in Figure 5.8.

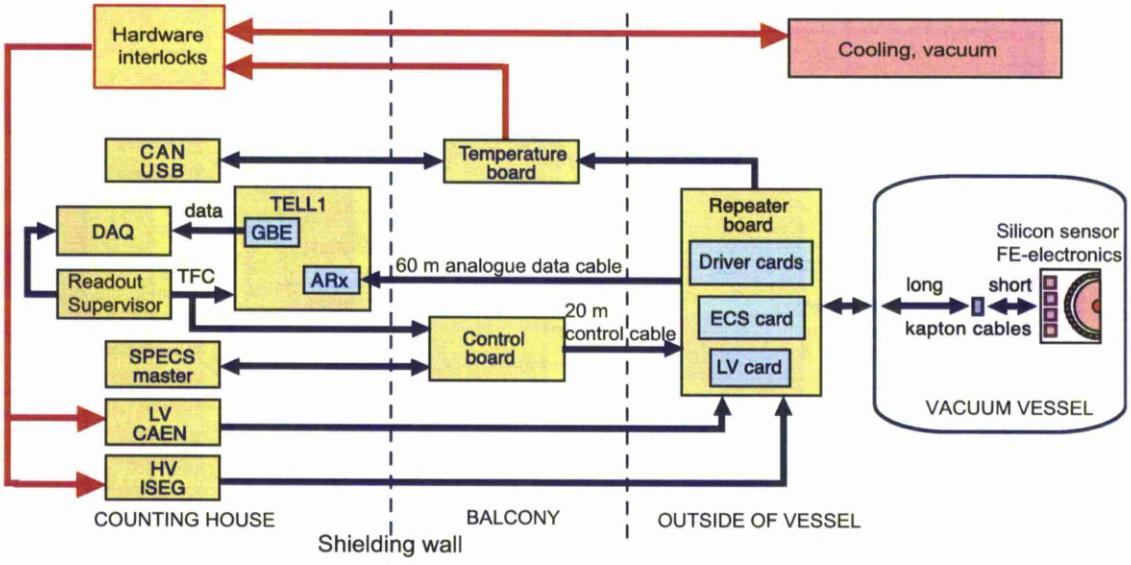

Figure 5.8: The VELO DAQ system.

The repeater boards each contain six cards; one Low Voltage (LV) card, one Experiment Control System (ECS) card and four driver cards. The LV card provides the low voltage supply to the hybrids, driver cards and the ECS card. The driver cards amplify the analogue signal and compensate for any distortions that may occur when the data is

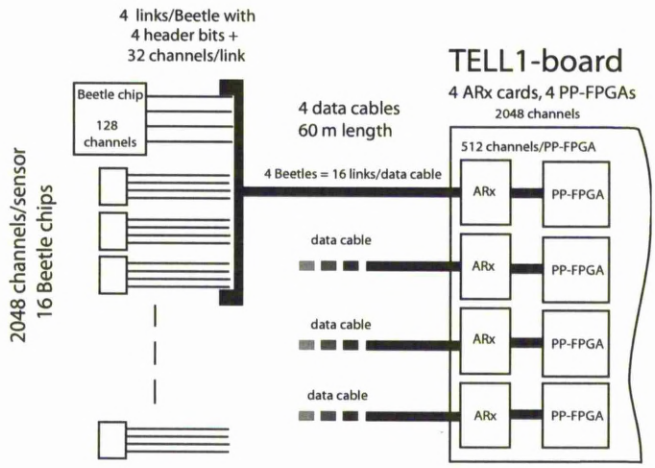

Figure 5.9: The readout chain from a sensor to a TELL1, with the repeater boards omitted.

transmitted via 60 m cables to the TELL1 readout board [55][56]. The ECS card controls and monitors the LV regulators. Figure 5.9 shows the readout chain from a sensor to a TELL1.

In addition to providing an interface to the ECS via a credit card PC (CCPC), the TELL1 board contains four A-Rx cards that digitise the signal. The signal is processed (see Section 5.7.2) before being sent to the High Level Trigger (HLT) via a Gigabit Ethernet (GBE) card. One repeater board and one TELL1 board are required per sensor. The control board receives Timing and Fast Control (TFC) signals via the TTC protocol[3] from the readout supervisor. In addition to this the control board distributes commands via I^2C from the ECS to configurable components (e.g.Beetles, LV). Each control board serves six repeater boards. The temperature of the hybrids and repeater boards is monitored using the temperature boards. The value of the temperature is distributed to the ECS and hardware interlock system. The ECS controls and monitors the HV and LV systems, the cooling, VELO motion, etc. This is commonly known as the slow control, and is developed using PVSS a commercial software package by ETM Professional Control.

[3]Timing, Trigger, and Control system. An LHC wide protocol used to transmit clock and synchronization signals.

5.7.2 The TELL1 Readout Board

The TELL1 is the common readout board used by the LHCb subdetectors, except the RICH. The TELL1 is composed of a motherboard hosting several mezzanine cards and is shown in Figure 5.10. It provides common mode correction, zero suppression and data formatting for the subdetectors. The main processing elements of the TELL1 are four field programmable gate arrays (FPGA), the board provides four connectors to accept two kinds of receiver cards. The analogue receiver card (A-Rx), is for the reception and digitization of analogue signals from the VELO. The optical receiver card (O-Rx) is for the reception of digital signals from the other subdetectors. Due to high radiation levels at the VELO and space restrictions the analogue data is transmitted to the TELL1 and digitised on the A-Rx card. Each TELL1 contains four A-Rx cards, each digitising 16 links from the Beetle chips to 10-bit precision, and sampling the data from four Beetle chips at 40 MHz.

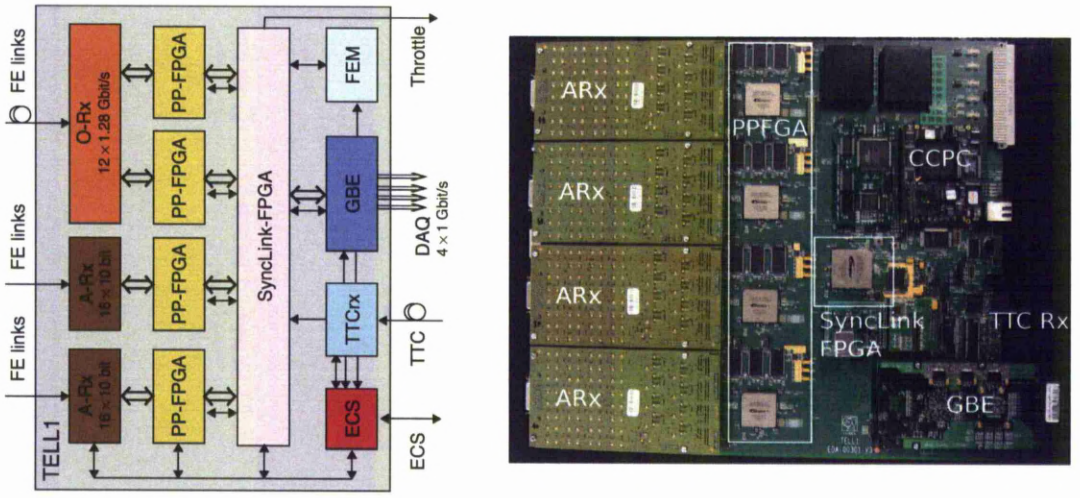

Figure 5.10: Left: A schematic of the components and interfaces for a TELL1. Right: A photograph of a TELL1 board with the main components labelled.

TELL1 Processing

After digitisation the data is sent to a pre-processor FPGA (PP-FPGA), of which there are four per TELL1. The processing steps performed on the TELL1 are shown in Figure 5.11 and the sequence consists of:

Pedestal Subtraction. The 10-bit digitisation in the A-Rx cards converts the analogue value of each Beetle channel to a value in the range 0-1023 ADC counts. The baseline of the digitised output is 512 ADC counts. The data on each of the 2048 readout channels is shifted up or down relative to its neighbouring readout channel. This is due to slightly differing voltage baselines for each channel, as is to be expected, as the electronic readout pathway from the silicon to the ADCs differs from channel to channel. Using the ADC data, these baselines can be calculated by averaging over many noise events. These baseline averages are commonly referred to as pedestals. A pedestal subtraction was performed to normalise the ADC values about 512 ADC counts. The pedestal is calculated as follows: An average of the raw values is calculated for a particular channel over all the events taken, i.e., for channel x, using N events the pedestal is

$$P_x = \frac{1}{N}\sum_{k=1}^{N} A_x^k \tag{5.1}$$

where A_x^k is the raw data in channel x for event k, and P_x is the pedestal value for channel x. The pedestal value is calculated for each channel, and then subtracted from the signal in that channel. A new set of pedestals is calculated for each module. The pedestal value to subtract is either loaded from a database at the beginning of a run or calculated over the first 4096 events.

Beetle Header Crosstalk Correction. There are 36 channels in each analogue link, 4 header bits and 32 Beetle channels. The final two header bits are used to encode the pipeline column number (PCN), which is the position of the event in the Beetle pipeline buffer. Due to crosstalk, a fraction of the signal from the header spills over into the first channel. The header heights are calibrated to be $\sim 30\%$ higher than a MIP. Since, the amount of crosstalk and the pulse height of the header bit is known, this crosstalk can be corrected. Without the Beetle header crosstalk correction, the first channel of each analogue link will be noisy. This function is not enabled during default running conditions[57].

Finite Impulse Response Filter. This is a digital filter which corrects for crosstalk effects in the readout chain. The primary source of crosstalk in the VELO is cable crosstalk, which occurs when the signals are transmitted along the 60 m cables from the vacuum vessel to the counting house. For further details on the filter and its implementation see, [56][58].

Mean Common Mode Correction. Common mode (CM) noise is the noise common to a set of elements on an electrical pathway. The VELO operates in a noisy environment where CM noise can be significant. An example of common mode noise in the VELO sensors is RF pickup from the LHC beams. The first of two common mode algorithms is the mean common mode suppression (MCMS), which corrects for a constant shift. The Beetle chip has 4 output ports each reading out 32 channels, which means 32 channels share a common pathway. The common mode noise is calculated by grouping the channels into blocks of 32 and calculating the mean.

$$C = \frac{1}{32}\sum_{x=1}^{32} B_x \tag{5.2}$$

where C is the common mode noise for a block of 32 channels, and B_x is the data in channel x after each of the previous processing steps. In the pedestal calculation all events are averaged, but the common mode noise changes for each event. Therefore, the common mode noise is calculated for a block of 32 channels on an event by event basis. The algorithm calculates the mean common mode noise of a link with and without clusters and removes the calculated mean from the full link[56][59].

Channel Reordering. Due to the scheme in which the Beetles are bonded to the sensors, scrambling occurs such that consecutive channels are not connected to adjacent sensor strips. The sensors are readout in this order, known as hardware or chip channel order. The reordering algorithm unscrambles the Beetle channel order back into strip order.

Linear Common Mode Correction. The final common mode algorithm is the linear common mode suppression (LCMS), which accounts for a common and slope shift. Due to resource limitations on the PP-FPGA, the algorithm cannot be too complex. The implemented algorithm, is based on a linear fit to the signal in a strip in groups of 32 and is calculated in a event by event basis. The algorithm is described in detail in references[56][59].

Clustering. The final stage of the processing is to form the clusters in the sensors. A cluster is formed by a seed strip if it passes a set threshold. Up to three other strips can be included in the cluster if they pass an inclusion threshold. The thresholds for a seed strip can be set individually depending on the signal to noise ratio of the strip, and the

inclusion threshold is 40% of it. The default thresholds are ~ 10 ADC counts for the seed, and ~ 4 ADC counts for the inclusion [60].

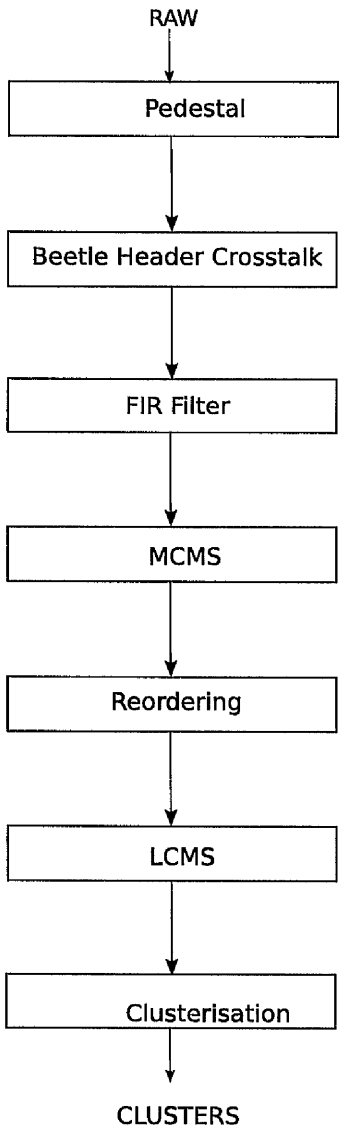

Figure 5.11: A flow diagram of the stages of signal processing in the TELL1.

Once the signal is processed on the PP-FPGAs, it is transferred to the synchronisation and link FPGA (SyncLink FPGA). The SyncLink FPGA distributes synchronisation signals to the PP-FPGAs, which it receives from the TTC-Rx chip. The SyncLink FPGA merges the data fragments from the PP-FPGAs. The data is now said to be zero suppressed (ZS) and is transferred to the gigabit ethernet (GBE) network card, which transfers the data to the HLT.

During normal operations ZS data is sent to the HLT, but it is possible to included a non zero suppressed data bank (NZS). Unlike the ZS data which only contains the clusters, NZS is the full unprocessed data. The processing of NZS data can be performed by a bit perfect emulation of the TELL1, in the VETRA package [61] by the TELL1 emulator. VETRA is the offline analysis and monitoring software platform for the LHCb Vertex Locator, and is part of the LHCb GAUDI software framework[62]. NZS data is widely used in the commissioning and monitoring of the VELO, it is also used in the testbeam analysis in Chapter 6, although in this case the processing is not performed by the TELL1 Emulator. The NZS output of the TELL1 is processed in the testbeam using floating point calculations rather than integer.

5.8 The Pile Up Detector

The Pile-Up system consists of two stations of R-sensors integrated in the VELO detector upstream of the interaction point. The detector is used in the L0 trigger to veto bunch crossings with multiple inelastic interactions. Multiple vertices are detected using a simple histogramming technique. The resulting vertex z-position resolution has been estimated from beam tests to be $\sigma_z = 2.8$ mm. For further details, see [63][64].

The digital signals from the Pile-Up sensors are read out using comparators on the Beetle chips and carried off the hybrid over 80 Mbit s_{-1} copper links and 1.6 Gbit s_{-1} optical links to Vertex Processing Boards where the multiple vertex search algorithm is executed. The result is sent to the L0 electronics where a trigger decision is formed. In parallel, the sensors are read out analogue, similar to the VELO, which adds four upstream R-sensors to the 84 standard VELO sensors.

5.9 Detector Alignment

As mentioned previously in this chapter, the VELO design is driven by the requirement of high spatial resolution. Precise knowledge of the positions of the sensors, i.e. alignment, is key to achieving this. The core of the alignment strategy is a high precision assembly and detailed metrology, however the requirement of the VELO to open during LHC fills introduces the need for a fast track-based software alignment procedure. It is expected that the position of the detector halves will be known within an accuracy of 10

μm through the position measurement of the motion system. The software alignment, presented in reference [65], uses track residuals to determine the relative positions of the sensors in each module, the module alignment within a detector half and also the alignment of the detector halves relative to each other.

The relative alignment of the R-sensors and Φ-sensors uses an iterative fit of the distribution of track residuals across the surface of the silicon sensor. The relative alignment of the 21 VELO modules in one detector half is based on a non-iterative method using a matrix inversion technique to minimise the χ^2 of the fit. The matrix inversion is based on the Millipede algorithm [66].

Two methods are used for the alignment of the detector halves relative to each other. In closed position, the same technique is used as for the module alignment, based on tracks with hits in the small overlap region of the detector halves. The sensor overlap between the halves corresponds to 2% of the active area. When the detector is not in closed position, an alternative method is used where the position of the primary vertex is reconstructed in the two halves separately. The relative alignment between the halves is calculated by comparing the reconstructed vertex position. The alignment of the VELO with respect to the other subdetectors is described in reference [67].

5.10 Radiation Environment

Due to the close proximity of the VELO sensors to the interaction region, the radiation environment that the VELO operates in is very harsh. The expected fluence in the most irradiated area for one year of nominal running is $1.3 \times 10^{14} \mathrm{n}_{eq}/\mathrm{cm}^2$. The expected fluence at the innermost radius with current running conditions is $5 \times 10^{13} \mathrm{n}_{eq}/\mathrm{cm}^2$. The radiation flux is strongly non-uniform and depends on the distance of the VELO station from the interaction region in z, and radius [32]. The dependence of flux as a function of radius is described by

$$\phi = Ar^k \tag{5.3}$$

where r is the radial position of the sensor, A is the fluence at r=1 cm, and α is the radial dependence.The fluence decreases with radial distance from the interaction point with an

approximately $1/r^{1.75}$ dependence. The predicted fluence is assigned an uncertainty of $\sim 8\%$ which is dominated by uncertainties due to particles with no available displacement damage data. The predicted fluence for two VELO sensors is shown in Figure 5.12. The radial dependence of flux means that the radiation damage on the VELO sensors is at its highest where the resolution information of tracks is at its most important; the regions of smaller pitch. The non-uniformity of the radiation damage will lead to the innermost regions of sensors under going type inversion earlier. Also, after severe radiation damage these innermost regions will require a higher bias voltage to make them fully efficient. Understanding the effects of radiation damage on the sensor performance is therefore vital to the experiment. The performance of the VELO is detailed in Chapter 7, and the performance of irradiated VELO sensors is investigated in Chapter 6.

5.11 Commissioning of the VELO DAQ

This section describes the test and tools used during the commissioning of the VELO DAQ. For a complete description of the VELO DAQ commissioning see [68].

5.11.1 Test Tools

A common set of analysis tools was employed during the DAQ commissioning. The collected test data were first processed with dedicated VETRA algorithms, and later analysed with the ROOT package[69]. These tools are described here.

Cable Test

The signal from the repeater boards is sent to the TELL1s by means of 60 m copper cables, with each repeater board connect by 4 cables to a TELL1 board. This makes a total of 352 cables, each containing 16 links. The aim of the cable test was to validate the cable connections. This was done by using the 32 channels of each link to encode a bit pattern using the test pulses of the Beetle chip. The 32 channels of each link are split into blocks of 8 channels, allowing 4 8-bit numbers to be stored. The 8-bit numbers are used to store 2 copies of the link number and hybrid number, two copies are made to make the test more robust against noisy or dead channels. For further robustness the link number is encoded as $2 \times (link + 1)$. The addition of 1 ensures that link 0 also has

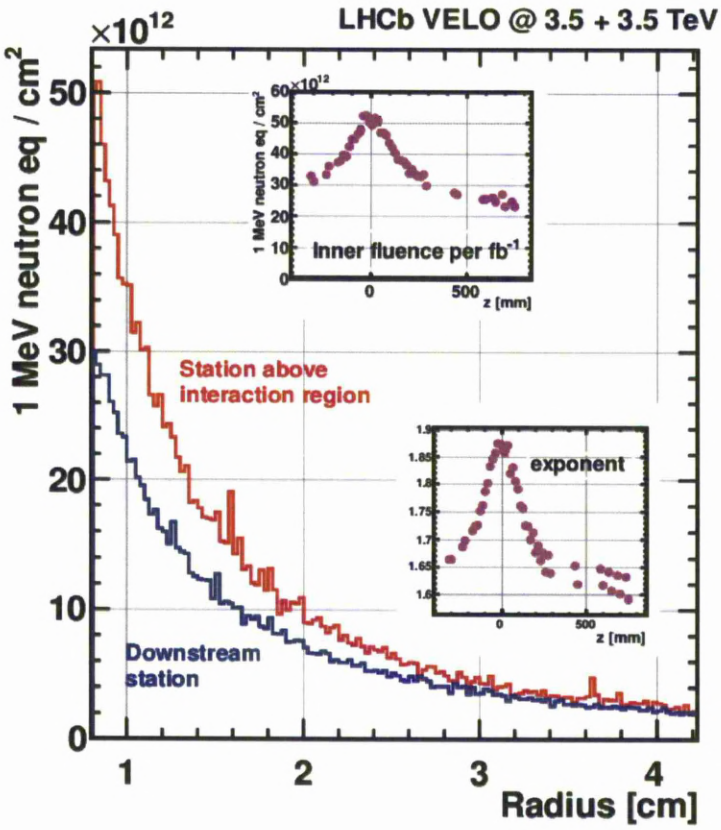

Figure 5.12: Main: The expected total hadron fluence normalized to the damage of 1 MeV neutrons from 1 fb−1 of delivered luminosity vs. radius for two VELO stations. The simulation is of proton-proton collisions at a 7 TeV centre of mass. Top Inset: The expected fluence at the innermost radius of VELO sensor vs. z co-ordinate. The interaction point is at z=0. Bottom Inset: The fitted exponent k for each sensor vs z co-ordinate.

a test pulse, and multiplying by 2 removes the influence of header crosstalk by not using the first channel of each link.

After taking data with the bit patterns present, the 8-bit numbers of each link are then decoded. If the decoded link and hybrid numbers are not in agreement with the number of the link and hybrid that they are decoded from, there is an error in the cabling. Figure 5.13 shows a correlation plot between the read out link (the link number that the analysis software thinks it is reading out) and the encoded link number, for a wrongly cabled and a properly cabled case.

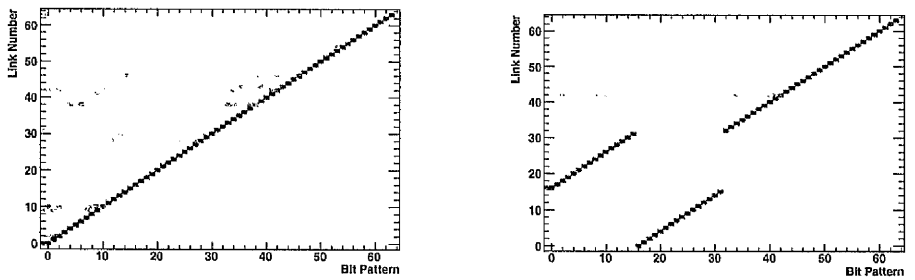

Figure 5.13: An example a correctly cabled TELL1 (left) and a miss cabled TELL1 (right). The miss cabled TELL1 the cables that read out links 0-16 and 17-32 have been swapped. The outliers are due to noise.

Digitisation Delay Scan

One triggered event of a VELO sensor is fully read out through 64 analogue links, that carry 36 analogue voltage levels spaced by 25 ns each. The first 4 levels in this readout block are encoded header bits. The signal travels along the 60 m cables from the hybrid to the A-Rx cards on the TELL1 board. On the receiving end, the A-Rx cards digitise the window of 36 consecutive levels, sampling every 25 ns. This window can be delayed by several clock cycles (25 ns) plus an adjustable fine time with steps 1/16th of a clock cycle, i.e. 1.56 ns. In order to compensate for the time skew in the signals resulting from different cable lengths the sampling time can be adjusted for each analogue link in an A-Rx card. The optimisation procedure consists of roughly aligning the readout of the front-end signals to the digitising window using test pulses injected into a channel. The test pulse is injected for the 16 possible phase settings, and the pulse height is determined at each setting. An automated analysis of the scan data uses test pulses to find the optimal sampling point based on two conditions: the best signal to noise ratio and a minimal cross talk. A plot of the delay scan analysis is shown for the four

A-Rx cards that digitise one sensor in Figure 5.14, the dashed lines indicate the test pulsed region and the optimal sampling time is indicated by the red line. The optimised sampling time of all of the links in all TELL1's is shown in Figure 5.15.

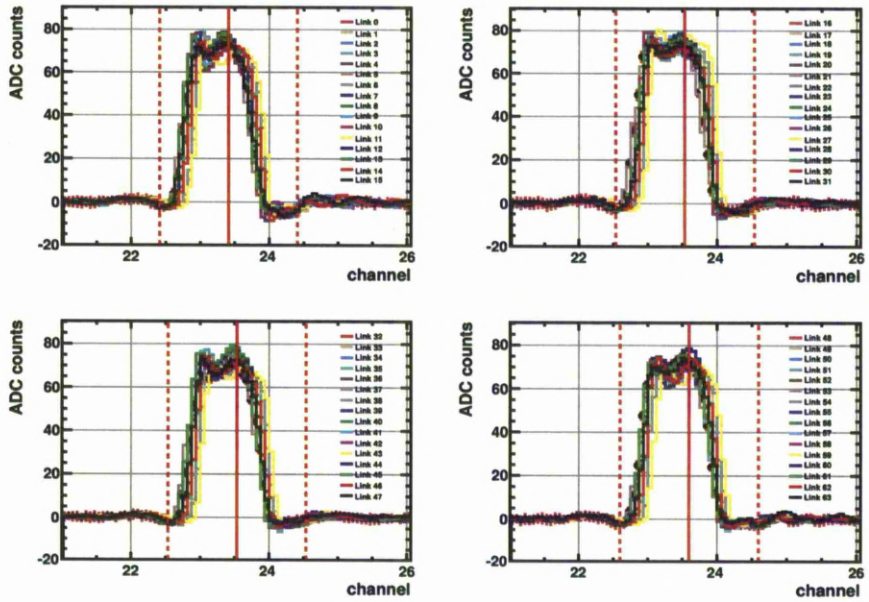

Figure 5.14: An example of the scan over the digitisation phases. In this figure, a whole sensor is shown grouped into 4 plots of 16 analogue links each. The horizontal axis represents the Beetle channel injected with a test pulse. The vertical continuous lines indicate the average sampling point for each group.

Sensor Snapshot

A good way to evaluate the sensor performance, and to find any problems with the sensors is by studying the noise and pedestals of the sensors. During the DAQ commissioning, this was performed by the Sensor Snapshot analysis tool. The noise is calculated using the VeloDataMonitor VETRA algorithm, in which the noise is defined as the RMS of the ADC distribution of a given channel, after pedestal and common mode subtraction. The TELL1 emulator is utilised to calculate and correct for pedestal, and common mode. Due to Beetle header cross talk, the first channel in a link is suppressed.

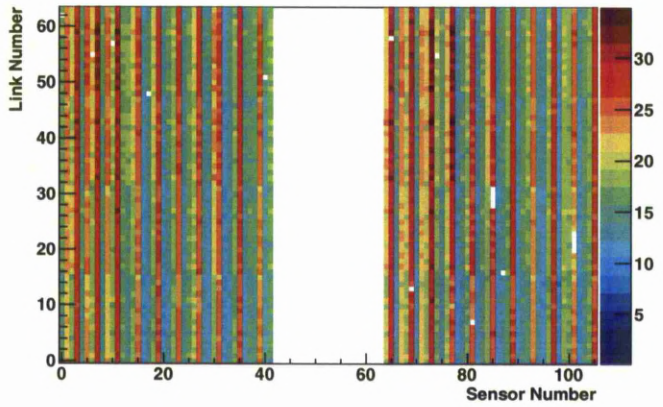

Figure 5.15: A 2D plot of the optimum sampling time of the A-Rx cards for all of the links in all of the TELL1s. Sensors 0-42 are R-sensors and 64-103 are Φ-sensors. The white marks indicate links without a test pulse and when the algorithm did not converge.

5.11.2 DAQ Commissioning

A-Rx Card Testing

As mention earlier in this chapter the A-Rx cards are responsible for the digitisation of the analogue signal from the Beetle chips. Each TELL1 contains four A-Rx cards, and each A-Rx card receives the analogue signal from one Beetle chip. The Beetle output is split into four links, so each A-Rx card contains 16 links. In total, 88 TELL1's are used in the VELO DAQ, and therefore 352 A-Rx cards are required to fully populated them.

Before the A-Rx cards were mounted onto the TELL1 boards the receiving amplifiers were tested. These analogue diagnostic checks were performed to evaluate the electrical properties of the cards; not the analogue to digital conversion. The analogue tests were performed by injecting a square wave into each link and the gain and the amplitude of the output signals were measured. The power consumption for each supply voltage, was also measured. Any A-Rx cards failing these tests was sent for repair.

The A-Rx cards were then mounted onto the TELL1 boards, and their digitisation performance was tested. A continuous sine wave was injected into each link of the A-Rx cards using a function generator. Each TELL1 trigger defines 1 event. The data was then sent to the HLT and an offline analysis was performed using a dedicated VETRA algorithm, and analysed in ROOT.

Analysis and Results

For each link a sine function is fitted to the measure data. The fitted function has four parameters: (i) the amplitude A; (ii) the frequency $f = \frac{\omega}{2\pi}$; (iii) the phase ϕ; (iv)and the offset c. The four fit parameters are then stored to histograms, having one entry per event. The amplitude was chosen so that it is close to the full dynamic range of the ADCs. A frequency of 1 MHz was used as this gives a period of 1 μs, which almost fits the time of the pulse train containing the header and channel information of one link: 36×25 ns= 900 ns. The phase is not interesting since the TELL1 triggers at an arbitrary moment, i.e. the phase changes from event to event. The offset should be close to 512 ADC counts since this is the zero line for the ADC, i.e. no input voltage at the TELL1 (or for real data taking: no signal in a strip) should give a value close to 512 ADC counts. Figure 5.16 shows the digitised and fitted sine waves.

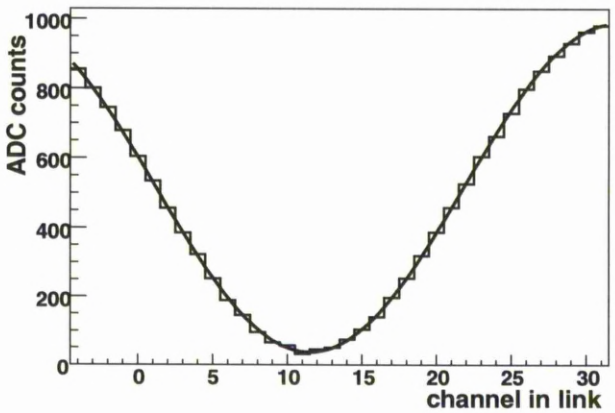

Figure 5.16: The digitised sine wave, with a fitted sine function. The x-axis shows a full analogue link of 32 channels plus the 4 header bits.

As well as the fit parameters other plots were used to judge there performance of the A-Rx cards. The integral of the histograms was used to spot any missing events. The residual between the fit and actual data was calculated for every channel, and plotted.

The ADC occupancy was plotted, which shows how often a certain ADC count appears, i.e. we fill for each event for each channel in the active link the measured value into an histogram ranging from 0 to 1023. If you take into account that the derivative at the maximum and minimum of the sine wave is 0 the minimum (close to 0) and the maximum value (close to 1023) should appear most often in the occupancy plot. The bit occupancy was also plotted, it is in principle the same as the occupancy plot but that the ADC value is in a 10-bit bit pattern and all the bits which are high (i.e. 1)

for this ADC value are plotted. Since we have a symmetric function around 512 we expects that all bits are high with the same probability, giving a flat distribution. If there is a significant deviation this indicates an open/short. This direct correspondence between bits and electronics exists since the ADC has an individual output line for each bit. ADC and bit occupancy plots for faulty and repaired cards are shown in Figure ??.

The A-Rx card testing also found other problems in the readout chain. The majority of these problems were due to the TELL1 boards, mainly PP-FPGA initialisation problems, and corrupted readout banks, and problems with the I^2C communication of the TELL1s.

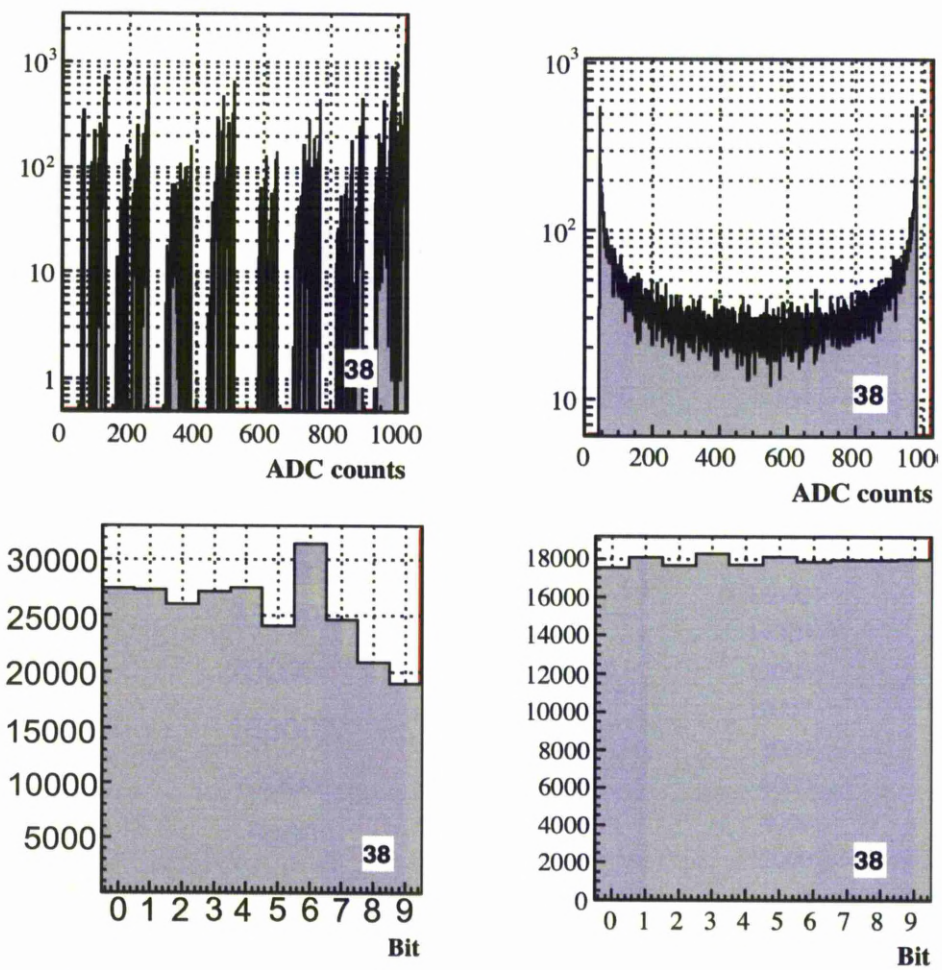

Figure 5.17: Left: The ADC and bit occupancy plots for a link with a short. ADC values are systematically missing in the ADC occupancy plots, and the bit occupancy is not flat. Right: The same plots once the A-Rx card was fixed.

The total number of A-Rx cards tested was 410, with a failure rate of 28%. All the TELL1s were equipped with working A-Rx cards and the major failure modes of the A-Rx cards were discovered. Of the broken A-Rx cards 25 were repaired and used as spares. Table 5.2 summarises of the A-Rx card results.

Failure Mode	Failed TELL1s
Analogue Test	16
Bit Problem	48
No Data in Link	20
High RMS	11
Noisy Link	6
TELL1 Problem	8
Other	8
Total	117

Table 5.2: A summary of the A-Rx card faults.

TELL1 Uniformity Test

In the test of the full readout chain, the uniform behaviour of the TELL1 boards was investigated using a test setup consisting of a dummy module, a repeater board, a control board and a set of one control and four data cables. The dummy module had a fully populated hybrid but no silicon sensor. The main purpose of the test was: (i) to find problematic TELL1s; (ii) to investigate differences in noise contribution between the A-Rx cards. Using the same module and data cables for all TELL1s, a large difference in noise between two TELL1s can be attributed to the A-Rx cards; (iii) to compare the pedestal levels of the A-Rx cards. Large deviations from 512 ADC counts reduce the available dynamic range. Out of the 84 VELO TELL1 boards that were included in the uniformity test, 67 could be read out correctly. The remaining 17, about 20% of the boards, had various problems that prevented data taking and were repaired later. It was found that some of the boards had a problem with the vias[4] which caused them to behave unstably or break when thermally cycled. The test setup was connected to each TELL1 board and 10,096 noise events were recorded. The first 4096 events were

[4]Connections between the different layers of the TELL1 PCB

used for the pedestal calculation and the remaining 6000 for the noise calculation. As the relative RMS error, δ(RMS)/RMS, of the noise can be approximated with $1/\sqrt{2N}$ [3], this renders a precision of 1%, which typically corresponds to 0.02 ADC counts for a VELO sensor. Since the same dummy module and cables were used all of the time, any variations between measurements should come from the TELL1 itself, especially from the A-Rx cards. To spot variations, a reference TELL1 was used for comparison. In practise, five reference TELL1's were used, one for each of the five crates that hold the TELL1's in the counting house. Examples of two raw noise spectra can be seen in Figure 5.18, for a good TELL1, and one with problematic links. The plots show the noise of the TELL1 under test, the noise of the reference TELL1, and the difference between the two. For all well-behaving channels the difference is close to 0. This means that the differences in noise contribution between A-Rx cards are small. The total raw noise contribution is typically in the range 1.5-1.6 ADC counts. To compare the pedestal variations, the pedestal values of each channel in the tested TELL1s are plotted in Figure 5.19. As can be seen, the distribution of pedestal values is narrow (6.5 ADC counts in RMS) compared to the full dynamic range of the ADCs (1024 ADC counts). Out of the 135,168 channels tested, 720 entries (0.5%) are in the overflow and underflow bins. They belong to channels read out with problematic A-Rx cards. With the results from this uniformity test, these problems were spotted and subsequently corrected.

Slice Test

The slice test was performed as a way to test the full readout of every VELO slice. This was done by connecting a repeater board, and a dummy module to each of the 88 TELL1s. The components of the slice test are:

The Cable Test Find wrongly cabled or mislabeled cables.

The Delay scan Adjust the timing of the digitisation on each of the A-Rx cards, to find the optimal timing settings.

The Sensor Snapshot Study the noise and pedestals of each sensor, with and without test pulses.

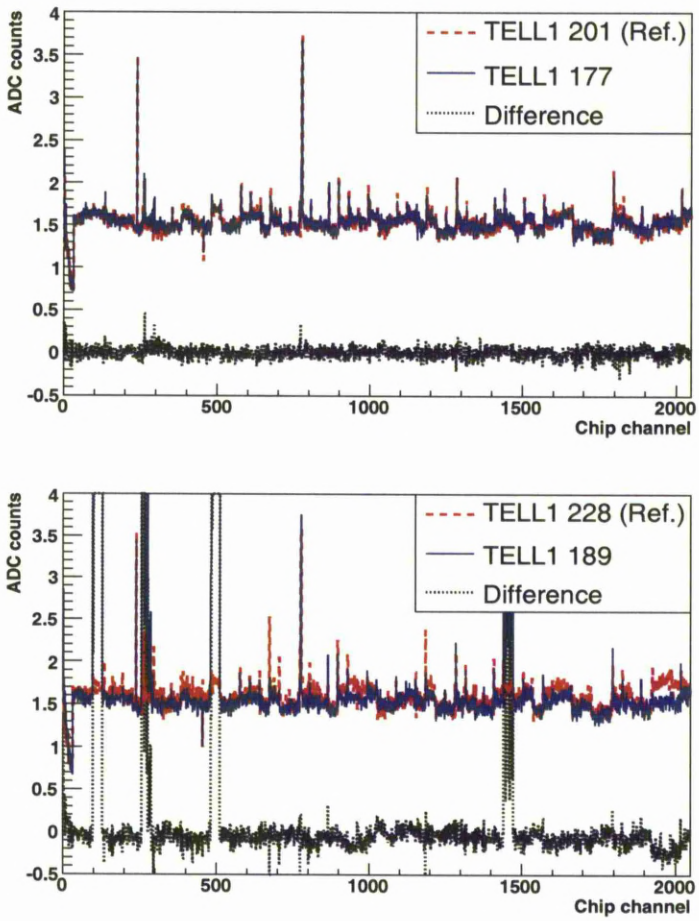

Figure 5.18: Raw noise spectra for a good (top) and a problematic TELL1 (bottom). A reference spectrum (dashed) is subtracted from the noise spectrum (solid) and any problems can be spotted in the resulting curve (dotted).

Results

Of the total 84 slices of the DAQ that were tested 64 showed no problems. Thirteen slices could not be tested; this was mainly due to TELL1 problems. These faulty TELL1s were replaced with spares, and repaired. Seven slices were found to have problematic links, mainly due to problems with A-Rx cards or cables. A summary of the slice test results is shown in Figure 5.20.

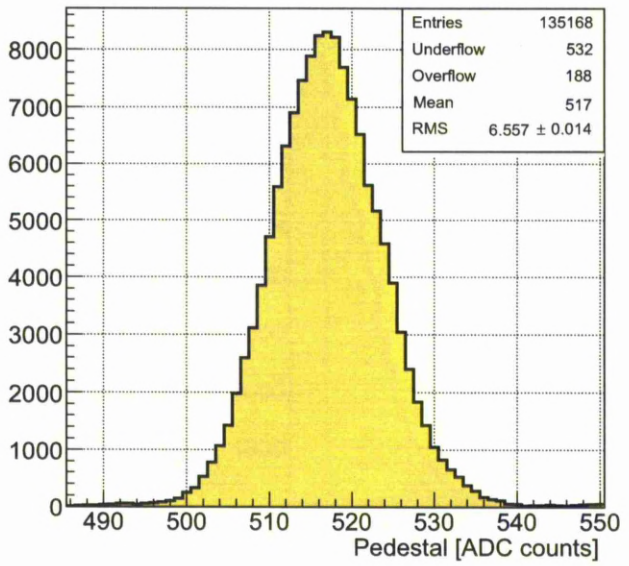

Figure 5.19: Pedestal values of all channels of all TELL1s tested in the uniformity test.

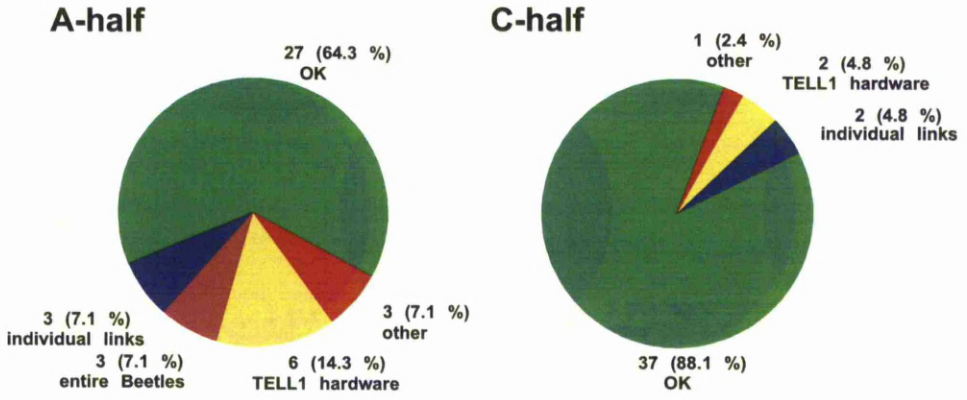

Figure 5.20: A breakdown of the results from the slice test. The faulty TELL1s were replaced with spares and sent for repair. The label "other" includes problems with Beetle configuration (1 slice), TELL1s that cannot see triggers (1 slice), and PVSS communication problems (2 slices).

5.12 Summary

The VELO performs tracking and vertex, for the LHCb experiment. In order to achieve the high spatial resolution required the VELO is very close to the interaction region, which means the VELO must perform in a harsh non-uniform radiation environment. The VELO utilises radiation hard silicon sensors that provide precision track coordinates close to the interaction region. The sensor performance is expected to degrade with time due to radiation damage, and measures have been put into place to track this performance. The commissioning of the VELO electronics chain required a set of software tools to be developed. These tools have proved to be very useful, not only identified faults within the chain, but enabled the major failure modes of the components to be identified. The VELO is now fully operational and the performance of the VELO is described in greater detail in Chapter 7.

Chapter 6

Performance of Irradiated VELO Sensors in Testbeam

6.1 Introduction

As described in Chapter 5, the radiation environment of the VELO is not only very harsh, but also non-uniform. Understanding the effect of this environment on the operation of the VELO sensors is crucial. The effects of radiation damage on silicon sensors are described in Chapter 3. Of particular importance to a precision experiment like LHCb, which relies on precise vertexing and tracking, are the change in the charge collected, and the change in the reconstructed position after irradiation.

To investigate these effects, two non-uniformly irradiated VELO R-sensors, which are sensitive to the radial coordinate, were investigated in a testbeam. Each of the R-sensors utilises a different radiation hard technology, one being an *n-in-p* sensor, and the other an oxygen enriched *n-in-n* sensor. A unirradiated VELO R/Φ module was used during the initial setup of the system. The sensors were irradiated at the IRRAD1 facility at the CERN PS, with a 24 GeV/c proton beam to a fluence between 1.4×10^{13} p/cm^2 and 1.4×10^{15} p/cm^2. Protons constitute the dominant hadron flux in the area where the VELO is located, which is why the sensors were irradiated with a proton beam. The maximum irradiation particle fluence is 0.85×10^{15} n_{eq}/cm^2 which is equivalent to the expected fluence after approximately 6 years of running at the nominal luminosity of 2×10^{32}cm^{-2}s^{-1} at a radius of 8.2 mm from the LHC beam. The irradiation profile is shown in Figure 6.1. There are three regions of irradiation, the aforementioned high fluence region, a low fluence region, and a transition region with varying levels of irradia-

tion. The sensors were then mounted back to back, and glued to a VELO hybrid forming an R/R module. The sensors are positioned in the hybrid such that the high fluence region of one sensor faces the low fluence region of the other sensor. The testbeam took place at the Fermilab MTEST facility, with a 120 GeV proton beam.

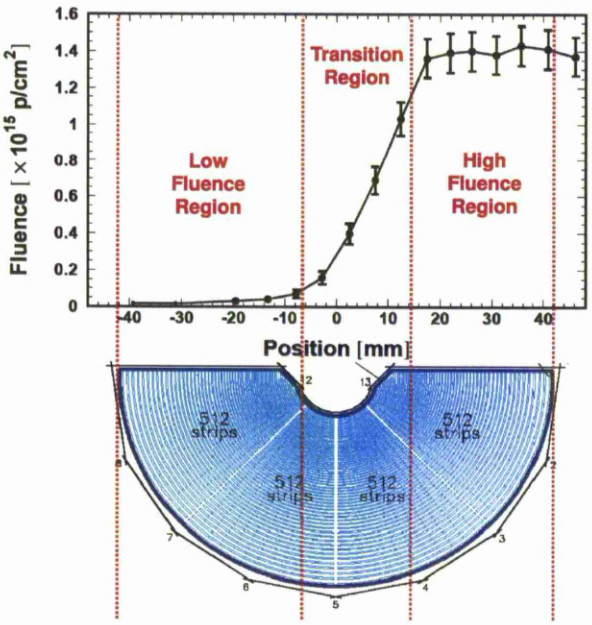

Figure 6.1: The irradiation profile of an R-sensor in the R/R module. The three different regions of irradiation are shown, as well as how these regions map onto an R-sensor.

6.2 Sensor Characterisation

As detailed in Section 3.7, irradiation introduces electrically active defects into the bandgap. These defects affect the sensor characteristics. Two such characteristics that are observed are increases in the leakage current, and the depletion voltage. To evaluate these changes the sensors were characterised before and after irradiation in Liverpool. During transportation from Liverpool to Fermilab, the sensors were not cooled and annealed. The temperatures of the sensors were not monitored so the level of annealing is not known.

6.2.1 Leakage Current

The leakage current in a silicon sensor is a source of shot noise, hence sensors with lower leakage current are expected to have better signal to noise. Radiation damage increases the leakage current and therefore degrades the performance of the sensor. The leakage current was measured prior to and after irradiation, and the expected increase after irradiation is observed. Figure 6.2 (a) shows the current versus voltage curves for the *n-in-n* sensor before and after irradiation. The increase in the leakage current after irradiation is apparent. Figure 6.2 (b) shows a comparison of the leakage current in the *n-in-n* and *n-in-p* sensors after irradiation, the curves for the two sensors are very similar.

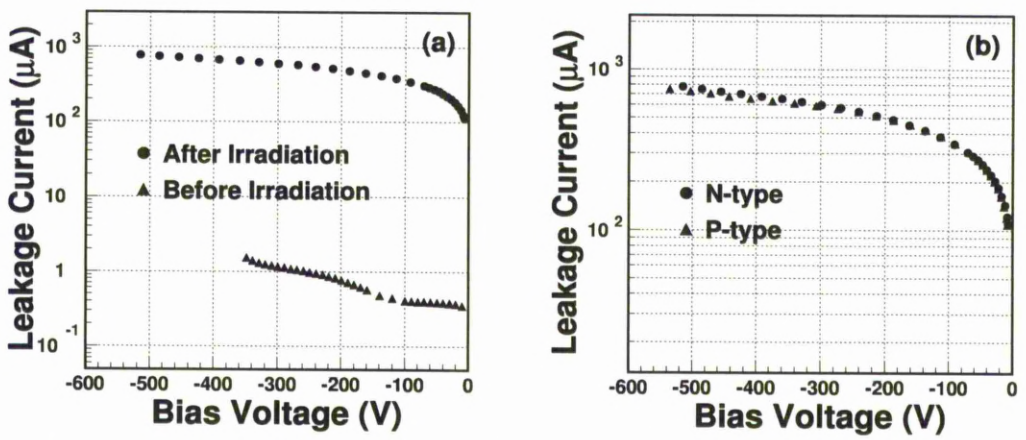

Figure 6.2: (a) The leakage current for the *n-in-n* sensor before and after irradiation a large increase in the current is observed after irradiation. (b) A comparison of the leakage current for both the *n-in-n* and *n-in-p* sensors after irradiation.

6.2.2 Depletion Voltage

The depletion voltage of the sensors was measured using the C-V method (see Chapter 3) before irradiation and were found to be 70V for the *n-in-p* sensor and 50V for the *n-in-n* sensor. The change in the effective doping concentration (N_{eff}), due to irradiation leads to an increase in the depletion voltage of the sensor. Figure 6.3 shows the $1/C^2$ vs V curves for the irradiated sensors before transportation. The curves shows three changes of slope induced by the progressive depletion of the three areas exposed to different levels of irradiation in the sensors. The sensors were biased to 500V and from these curves it is difficult to determine if the sensors are depleted and the curve has reached

a plateau. This is because the sensors were underdepleted Similar *n-in-n* and *n-in-p* VELO R sensors that were irradiated in the same batch were annealed and biased to $\sim$900V. The depletion voltage for these sensors was found to be 560V for the *n-in-n* sensor, and 530V for the *n-in-p* sensor.

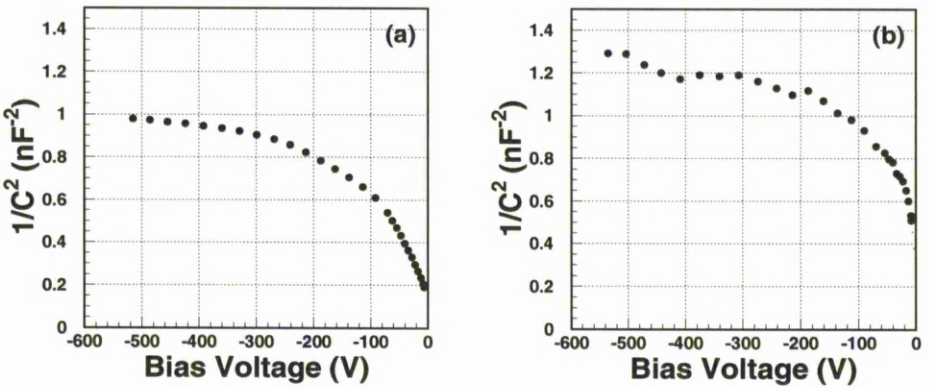

Figure 6.3: The C-V characteristics for (a) the *n-in-p* sensor and (b) the *n-in-n* sensor.

6.3 Setup and Alignment

The R/R module was installed inside a box flushed with N_2, and cooled to a temperature between -10 °C and -15 °C. The N_2 is used to prevent the sensors from icing up. A four station pixel telescope with an aperture of 35 mm $\times$ 35 mm was constructed to provide tracking information. Two pixel stations were placed either side of the R/R module, at a distance of 50 cm. The pixel sensors, and FPIX2 readout ASICS were originally developed for the BTeV experiment [70][71]. The pixel sensors are *n-in-n* sensors with p-stop isolation, and pixel size of $50 \times 400\ \mu m^2$. The pixel sensors have a S/N ratio of $\approx$150, and the resolution is 5-9μm in the narrow dimension of the pixel (50μm) depending on track angle [72]. The pixel sensors are bump bonded onto the FPIX2 chip, with each chip reading out a total of 2816 channels (22 columns $\times$ 128 rows). The FPIX2 chip was not fully functioning and was treated as binary instead of 3bits. One pixel plane comprises of 6 hybrid pixel modules. Pixel rows are oriented alternately in the x and y direction in successive planes. The track projection error at the location of the device under test was found to be $\approx$ 4-8μm depending on track angle and the number of hits[73]. The

setup is shown in Figure 6.4. The module under test was mounted on a support stand that allowed translational movement in the x and y direction, and rotations around the x axis at -4°,4°,8°,12° and 20°. The data discussed in this chapter were taken at 0°, with the R/R module perpendicular to the beam.

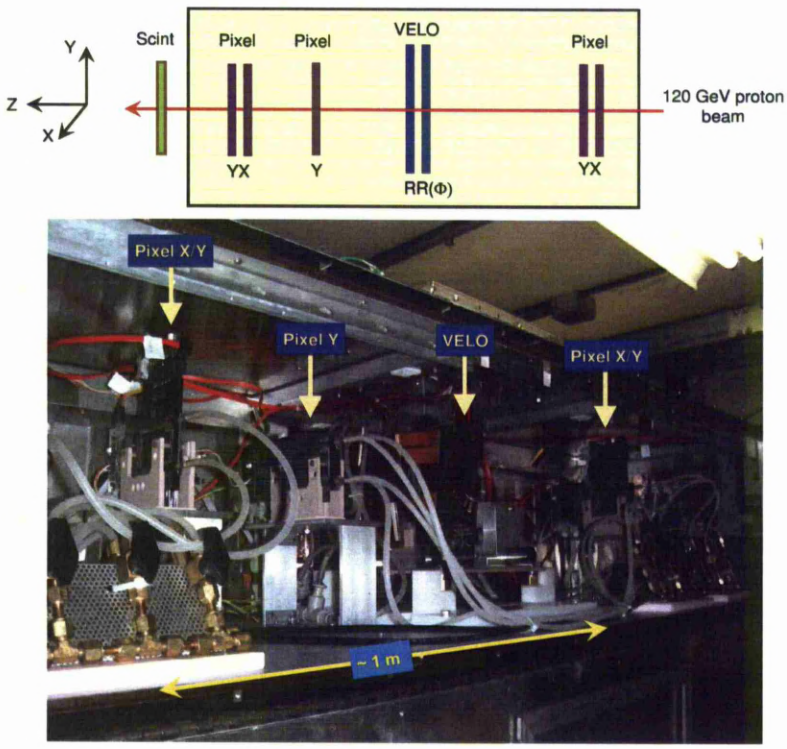

Figure 6.4: The VELO R/R module in the testbeam box. The *n-in-n* sensor is upstream, and the *n-in-p* is downstream. The pixel modules used for tracking are also shown.

The VELO modules were read out with the standard LHCb TELL1 data acquisition boards with an interface board, this allowed them to operate in a standalone mode, without requiring the sophisticated data acquisition system used in the LHCb experiment. The *n-in-n* sensor was read out with the TELL1 labelled 5 (TELL5), and the *n-in-p* was read out with TELL8. The sensors are referred to by the TELL1 used to read them out in parts of this chapter. The pixel system was read out with a dedicated data acquisition system. A scintillator counter read out at both ends provided a trigger signal, synchronising the two independent data acquisition streams. The beam spot radius could be tuned to have a radius ranging between 1 cm and 3 cm. The entire VELO sensors could not be illuminated by the proton beam. Therefore, data was taken

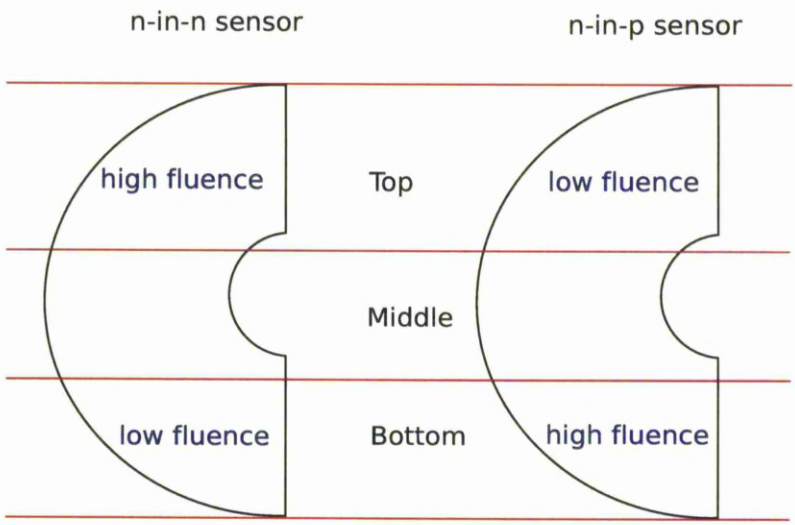

Figure 6.5: The orientation of the R-sensors in the R/R module. The three different beam regions (top, middle, bottom) are shown, as well as which irradiation zone in the sensors is illuminated by the beam in the different beam positions.

in three positions each with the beam illuminating one of the three different regions of irradiation this is shown in Figure 6.5, and summarised in Table 6.1. In the top and bottom positions, the highly irradiated regions of the sensors are on opposite sides. In the middle position, the beam illuminates the transition region where the flux gradients are in opposite directions.

Beam Position	Sensor with High Flux Region	Sensor with Low Flux Region
Top	*n-in-n* (TELL1 5)	*n-in-p* (TELL1 8)
Middle	NA[1]	NA
Bottom	*n-in-p* (TELL1 8)	*n-in-n* (TELL1 5)

Table 6.1: A summary the beam position in the sensors.

The track parameters obtained from the pixel telescope allow the determination of the position at which the beam intersects the VELO module. In order to predict the track impact point; it is important to align the individual detectors in the telescope. We use a right-handed coordinate system, where z corresponds to the beam direction, y is oriented along the vertical direction upward and x is the horizontal axis. The centre of the first pixel station defines the origin. Each plane is defined by three offset

[1]Highest irradiation gradient. The gradients are in opposite directions

parameters dx, dy and dz and three angles (α,β and γ),defining their orientation through three rotations around the x, y, and z axis. The telescope alignment is performed in two distinct stages; first we align the pixel stations, then we align the VELO device under test with respect to the pixel system. An automatic iterative alignment procedure has been developed, performing a global minimization of the χ^2 of the fitted tracks. Additional alignment parameters are needed to define the position of the pixel modules in each sensor plane. As a hardware positioning procedure with a precision of few mm was implemented during assembly, only three additional parameters are needed to locate each module: two translational offsets and one rotation within the plane. For the VELO R/Φ reference module, the clusters are first matched to form 3D space points. Then the alignment with the pixel telescope is performed through minimization of the χ^2 between the 3D points and track projections. For the R/R module, the parameter of rotation around the local z axis (ϕ) is determined less precisely as no measurement is available, however the results presented are not sensitive to this alignment parameter. In total, 5 different sets of pixel alignment parameters, and 12 sets of VELO alignment parameters are determined, with dedicated data samples.

6.4 Beetle Issues

During the testbeam, the Beetle front end chips for the VELO were operated with analogue and digital power supply values lower than the nominal. This was due to resistive losses along the cable delivering the power supply to the VELO sensors. This had direct impact on the gain and noise performance of the sensors. The header signal is proportional to the analogue power supply of the Beetle. We can estimate the difference between the bias voltage applied and the nominal values by comparing the Beetle header signals in nominal running conditions and during the test beam. The header signal was $\approx$ 45 % lower than nominal in the testbeam, implying that the Beetles were under biased by $\approx$ 45 %. The test pulse calibration feature of the Beetle allows a charge programmed to be 22,500 e^- to be injected. The charge is expected to correspond to $\approx$37 ADC counts, but as a result of the low gain in the front end electronics the most probable charge collected from a test pulse is measured to be $\approx$16 ADC counts. The mean common mode corrected noise for an R-sensor in the VELO is expected to be $\approx$2 ADC counts, but the measured mean for the *n-in-n* and *n-in-p* sensors in the testbeam was $\approx$0.9 ADC counts. This affected the seed and inclusion thresholds for the clustering in the sensors. The former determines the minimum ADC value required to form a

cluster, and the latter determines whether adjacent strips are included in the cluster. A seed threshold of 4 ADC count and an inclusion threshold of 2 ADC counts (equivalent to about 2 noise standard deviations) are the default settings used accordingly.

6.5 Charge Collection Efficiency at Different Irradiation Levels

An important factor in the operation on the VELO is knowledge of the evolution of the charge collection efficiency of the sensors, as a function of accumulated flux. The charge collection efficiency is monitored in the VELO, which is described later in Section 7.2.2, and understanding how it changes after a flux equivalent to 6 years of running in the irradiated VELO sensors will give us an indication of the expected lifetime of the VELO sensors.

In order to estimate the charge collection efficiency of the irradiated sensor, only VELO clusters that are matched to a pixel track are used. The radial distance between the projected position of a pixel track intersecting the VELO sensor, and the measured position in the VELO sensor is required to be $\pm$ 200μm. The hitmap shown in Figure 6.6 shows the density of tracks in both the *n-in-n* and *n-in-p* sensors. The *n-in-n* and *n-in-p* sensors are R-sensors, so they are only sensitive in the radial direction, the hitmap is derived using the transverse coordinates of the matching tracks from the pixel telescope.

The charge cluster distributions are fitted with a Landau convoluted with a Gaussian, and the most probable value of the charge collected (MPV) is extracted from the fit. Figure 6.7 shows representative fitted Landau curves for the *n-in-n* and *n-in-p* sensors in both the high and low radiation flux zones at a bias voltage of 500 V. Figure 6.8 shows how the most probable charge collected changes with position for both sensors, with the irradiation profile also shown. The correlation between the fluence at which the zone is exposed and the charge collection efficiency is clearly visible. The measured decrease in the Landau peak for the *n-in-n* sensor is $\approx$30% in the area exposed to the highest fluence. The measured drop in the charge collected in similar sensors irradiated to approximately the same level, but without annealing is 50% [74]. The observed improvement in the charge collection of the testbeam sensors is consistent with the expected improvement due to annealing [75]. In the corresponding profile for the *n-in-p* sensor there is a dip in collected charge in the low fluence region. This is due to a dead Beetle readout chip

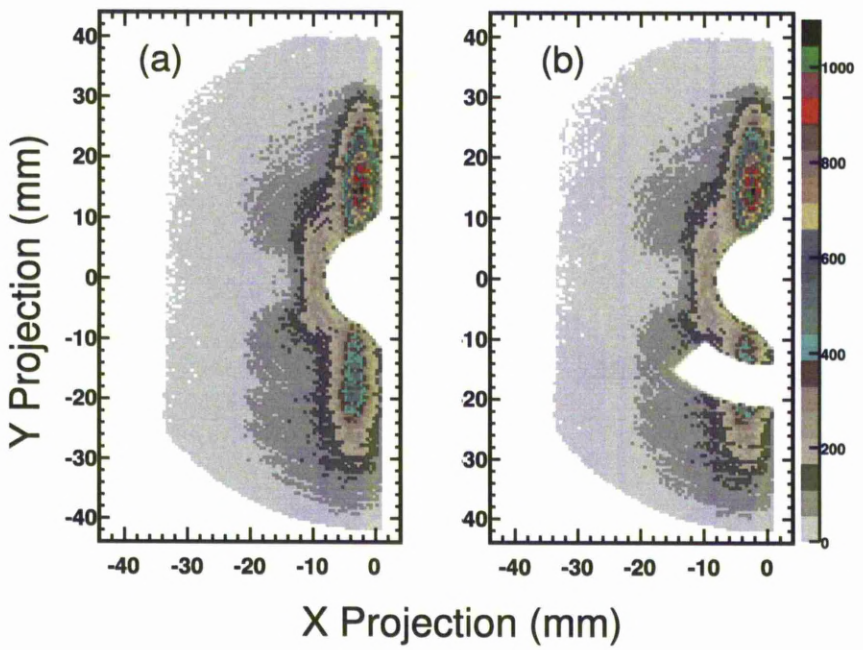

Figure 6.6: The track distribution of the VELO sensors using the transverse coordinates of the tracks fitted from the pixel telescope.(a) the *n-in-n* sensor, (b) the *n-in-p* sensor. The missing region in the *n-in-p* sensor is due to a dead Beetle chip.

in this region. In the *n-in-p* sensor the drop in the charge collection between the low and high irradiation areas is smaller than in the *n-in-n* sensor. At the outer edge of the high fluence region of the *n-in-p* sensor, there is a further drop of the charge collection efficiency compared to the innermost part of the high fluence region which withstood the same amount of radiation. The irradiation profile is flat in this region, so this dip is unexpected. It is unlikely that the irradiation profile is wrong. This trend is seen for different bias voltages, and may be attributable to the voltage settings used in the testbeam, and the response of the Beetle chips as mention in Section 6.4.

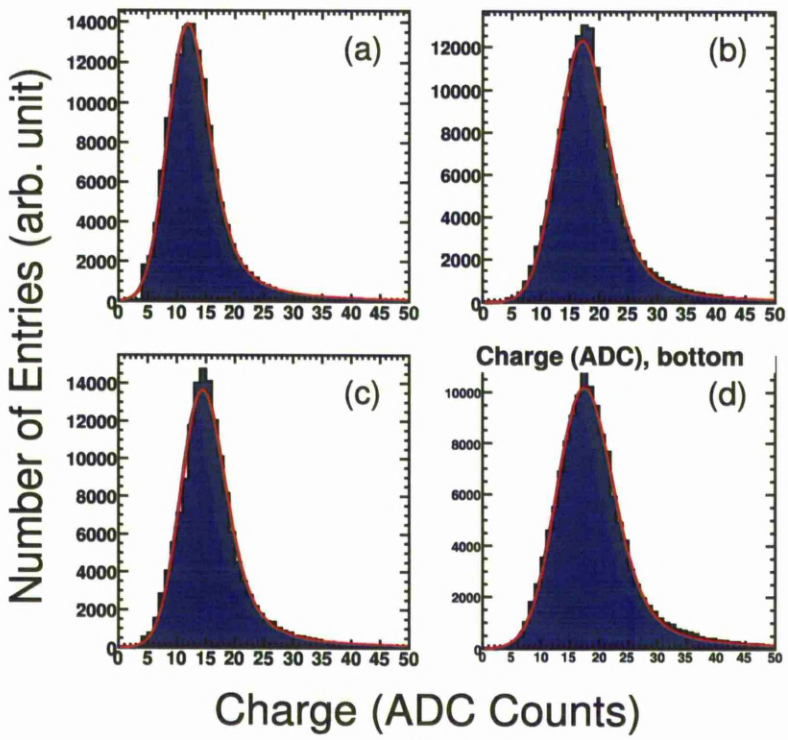

Figure 6.7: The collected charge distributions for the R-sensors in the different irradiation regions. (a) *n-in-n* sensor in the high fluence region.(b) *n-in-n* sensor in the low fluence region.(c) *n-in-p* sensor in the high fluence region. (d) *n-in-p* sensor in the low fluence region.

In order to further characterise the charge collection properties of these two devices after irradiation, we studied the dependence of the charge collection on the bias voltage applied to the sensors, up to the maximum voltage that could be applied while maintaining stable operation of 500V. Figure 6.9 shows the MPV as a function of bias voltage at high, and low levels of irradiation for both sensors. The depletion voltage before irradiation for the *n-in-n* sensor was 50V, and 70V for the *n-in-p* sensor. In Figure 6.9,

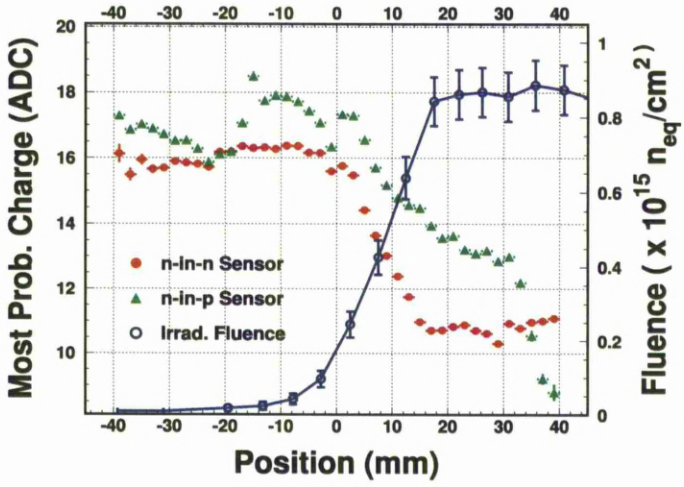

Figure 6.8: The correlation between the MPV of the collected charge and the irradiation profile at 500V. Both sensors show a correlation between dose and collected charge.

at low irradiation both sensors are depleted at the depletion voltages before irradiation. The charge collected in both sensors is flat after the depletion voltage is reached, as expected. In the regions exposed to the highest level of irradiation, the collected charge increases with the applied voltage as expected.

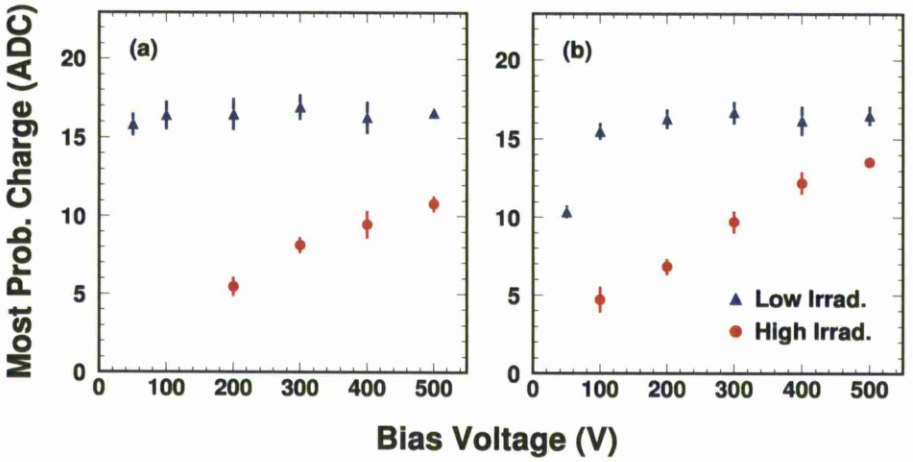

Figure 6.9: The collected charge vs bias voltage for (a) the *n-in-n* sensor and (b) the *n-in-p* sensor.

6.6 Cluster Finding Efficiency

The pixel telescope had a much smaller dead time than the VELO readout. Thus, in order to determine the hit efficiency one VELO sensor is used as a reference. We define as reference tracks pixel tracks associated with a hit in the reference sensor and we check that a matching hit is found in the sensor-under-test within $\pm$ 200 μm in radial separation and in the same sector as the reference sensor. Figure 6.10 shows the measured distributions for the *n-in-n* and *n-in-p* sensors at 500V. The small dip in efficiency at $\approx$15 mm for the *n-in-n* sensor is unexpected, and is so far not understood. The dip may be caused by the underbiased Beetle chips. At high irradiation the decrease in efficiency is largely accounted for by the loss in charge collection efficiency and consequent lower signal to noise ratio, as shown in Figure 6.11, which shows the correlation between efficiency and most probable value of the collected charge.

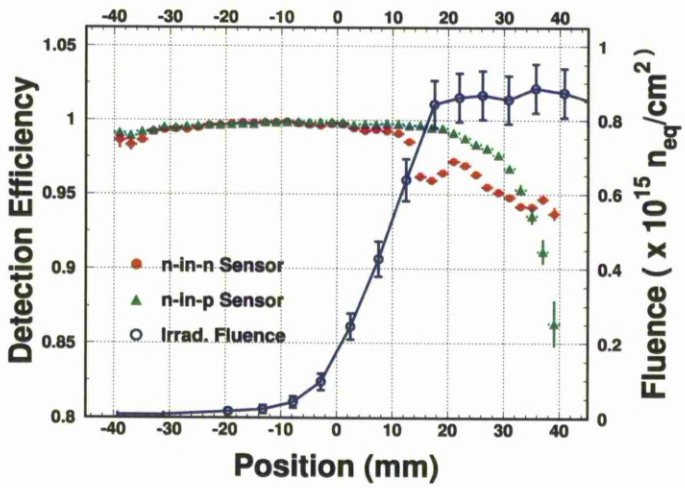

Figure 6.10: The cluster finding efficiency of the VELO sensors as a function of irradiation. The region with a dead Beetle chip in the *n-in-p* sensor has been masked out.

6.7 Effect of the Transverse Electric Field on Cluster Reconstruction Position

High irradiation gradients, that are the result of non-uniform irradiation can modify the electric field in silicon sensors. This can introduce a transverse component of the electric field (E_{tran}), which can lead to systematic shifts in the cluster reconstruction position [76]. The shifts in the cluster centroids can degrade the resolution of the sensors, which has

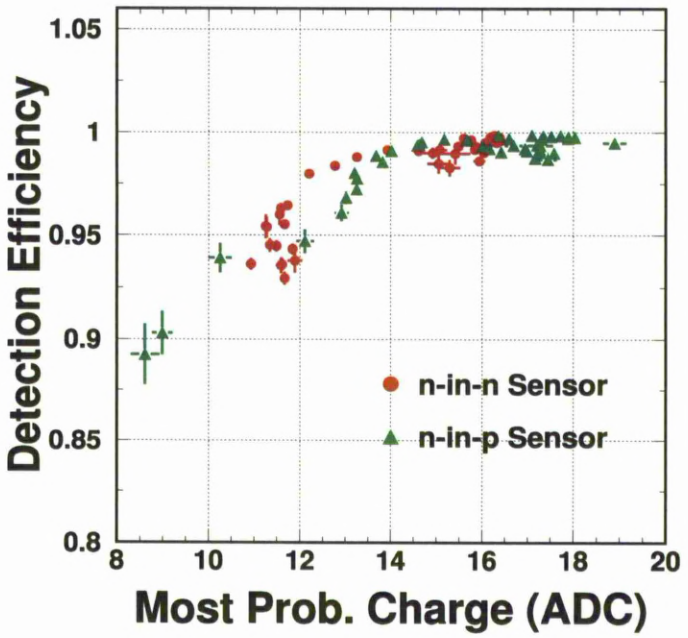

Figure 6.11: The cluster finding efficiency vs MPV.

obvious repercussions on the tracking performance of a vertex detector. Understanding the effect of E_{tran} is important due to the highly non-uniform radiation flux in the region of the VELO sensors at LHCb. To operate the VELO in these conditions we need to understand the effect of E_{tran} in the cluster reconstruction position, if any, in order to compensate for it.

6.7.1 Analysis

Data was taken at 500V, the sensors at this bias voltage are under depleted but this was the highest achievable bias at the testbeam,in all three beam positions in Table 6.1. In the top and bottom positions the high flux region of one sensor is adjacent to the low irradiation flux region of the other sensor. In the middle position, the beam illuminates the transition region. The transition region has the highest radiation flux gradient in the sensors, and as such is expected to have the largest shift in the cluster reconstruction position due to E_{tran}. The radiation flux gradients of the sensors in the middle position are in opposite directions.

The data processing used in this analysis implements floating point calculations for the common mode and pedestal subtraction. This is done to eliminate the truncation of

the raw strip charges caused by integerisation. Since the absolute silicon performance is under investigation this is preferred to using the VETRA emulator which utilises integer calculations. The processing algorithm used follows the same sequence as the standard TELL1 emulator in VETRA, except Linear Common Correction (LCMS) is not implemented.

The thresholds used are 4 ADCs for a seed strip and 2 ADCs for an inclusion strip. To minimise the number of noise clusters (strips with noise values above the cluster thresholds) cuts were performed on the total charge in a cluster (adc sum). For 1 strip clusters this increases the seed threshold to 6 ADCs. But, for multiple strip clusters the seed threshold remains the same. This allows you to suppress noise without losing efficiency for multiple strip clusters by setting the seed threshold too high. The cluster thresholds and cuts are summarised in Table 6.2. The values for the cuts on adc sum were chosen by plotting the charge collection distributions for 1, 2 and 3 strip clusters separately and cutting above the noise tail.

Threshold	ADC value
Seed	4
Inclusion	2
ADC Sum 1 Strip	6
ADC Sum 2 Strip	12
ADC Sum 3 Strip	30

Table 6.2: A table summarising the cluster thresholds and the cuts on adc sum of the clusters.

The cluster reconstruction positions are calculated using the weighted mean algorithm in Section 3.6, and VELO hits are matched with pixel tracks within a radial distance of 50 μm. As the effect of E_{tran} is to shift the cluster reconstruction position with respect to its true position, the track residual distribution (Δ_{track}) can be used to study this effect. The track residual (Δ_{track}) is the difference between the cluster reconstruction position in the VELO sensor (R_{velo}) and the cluster position predicted from a track using the pixel telescope (R_{track}),

$$\Delta^i_{track} = R^i_{velo} - R^i_{track} \tag{6.1}$$

Where i denotes the sensor. The Δ_{resid} distribution is defined as the difference between track residuals (Δ_{track}) in the sensors,

$$\Delta_{resid} = \Delta^5_{track} - \Delta^8_{track} = (R^5_{velo} - R^5_{track}) - (R^8_{velo} - R^8_{track}) \tag{6.2}$$

Any systematic shifts in the mean of the Δ_{resid} distribution are expected to be due to E_{tran}.

In this analysis there is a condition of 2 strip clusters in both sensors (2v2). The 2v2 clusters are used because they give better cluster reconstruction position resolution, due to charge sharing between strips. This allows for the cluster centroid to be calculated by interpolation using the charge on the two strips in the cluster. Since we are investigating very subtle shifts in the mean residuals, 2v2 clusters are the best solution because they give the best sensitivity.

A Gaussian function is fitted to the Δ_{resid} distribution for the three beam positions, and the fitted mean value is extracted. These plots are shown in Figure 6.12. The mean residual for each of the beam positions is shown in Table 6.3.

Beam Region	Mean Residual (μm)
Top	4.9 ± 0.4
Middle	2.5 ± 0.4
Bottom	3.3 ± 0.8

Table 6.3: The fitted mean value of the Δ_{resid} distribution in the different beam regions.

This simple analysis should in principle give a straightforward and unambiguous estimate of the magnitude of the shifts in the cluster reconstruction position due to E_{tran}. However there is also a further complication added by the read out electronics which tends to skew the reconstructed cluster position. This effect is called crosstalk. To understand the mean residuals estimated above we have to understand crosstalk in the sensors.

The system used to readout the VELO was used in a previous testbeam [77], and was found to be affected by crosstalk. Crosstalk is the process by which the signal in a readout channel spreads into adjacent channels. The Beetle chips on the VELO hybrids

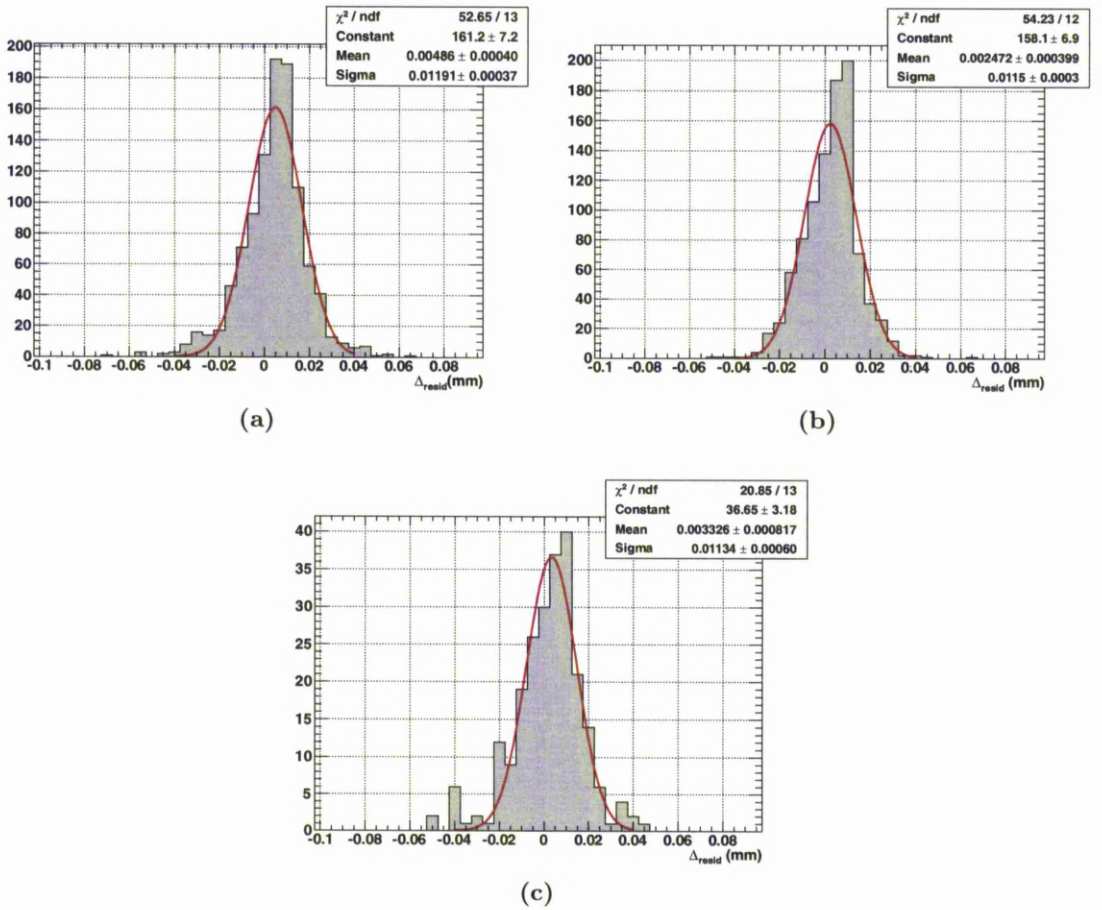

Figure 6.12: Δ_{resid} for the three data taking positions (a) top, (b) middle and (c) bottom. The histograms are fitted with a Gaussian distribution and the mean is extracted to give the shift in Δ_{resid}. The shifts are shown in Table 6.3.

readout the data in 25 ns time bins, however if crosstalk is present this signal can spill over into adjacent readout bins. This is illustrated in Figure 6.13 (a), the solid square represents a signal unaffected by crosstalk and is confined to readout bin t. The dashed line represents a signal with crosstalk present, it spills over into the adjacent readout bins; t+1 and t-1. The crosstalk in the VELO electronics chain at LHCb, is accounted for by cable compensation in the driver cards. At the testbeam, shorter cables were used and so the frequency based cable compensation could not be utilised.

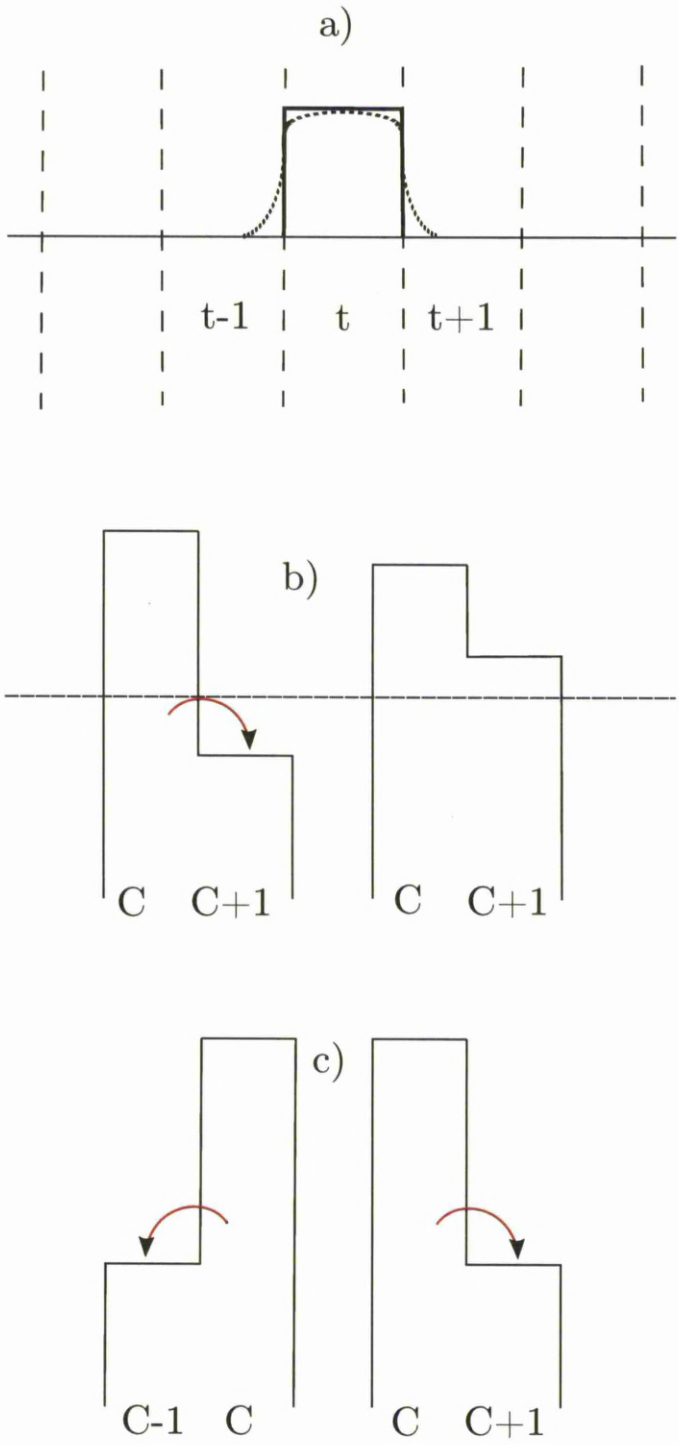

Figure 6.13: a) An unaffected signal is confined to a single 25 ns readout bin. A signal with crosstalk spills some signal into adjacent readout bins. b) The crosstalk from a seed channel can push an adjacent channel above the inclusion threshold. c) When the seed channel is earlier in readout order the crosstalk is said to be forwards. When the seed channel is later in readout order the crosstalk is said to be backwards.

The readout scheme of an R-sensor by the Beetle chips is shown in Figure 6.14. The sensor is spit into four quadrants of 512 channels, and then each quadrant is split in two sections of 128 and 384 channels. The quadrants are readout sequentially in chip channel order, with each subsection of a quadrant readout in an opposite direction. The R/R module has two R-sensors glued back to back, so each sensor is read out in the opposite direction to the other sensor. This readout crosstalk can shift charge from a seed channel onto a neighbouring channel. It is possible for the crosstalk to push the neighbouring channel above the cluster inclusion threshold, thereby causing a one strip cluster to become a two strip cluster. This is shown diagrammatically in Figure 6.13 (b), where the dotted line represents the inclusion threshold. This can shift the cluster reconstruction positions in the sensors and bias the residuals. In the of case 2v2 clusters, crosstalk can shift the charge across the channels, the cluster centroid will change since it is computed using the weighted mean of the charge in the two channels. A distinction is made between whether the crosstalk is forwards or backwards. If the seed strip is earlier in readout, the charge ratio is said to be positive, since any crosstalk would be in the forwards direction. If the seed channel is later in readout the crosstalk is said to be backwards, this is shown in Figure 6.13.

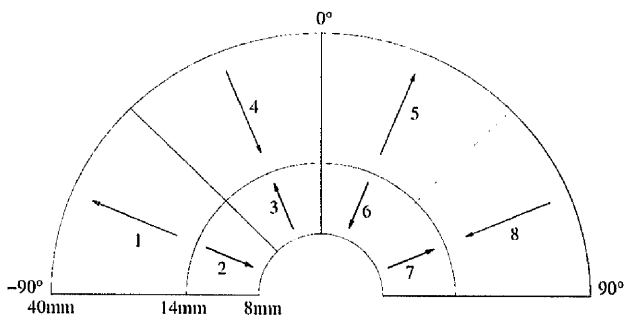

Figure 6.14: The readout scheme for an R-sensor.

A confirmation of the presence of crosstalk can be shown by plotting the charge ratio of two strip clusters. If crosstalk is not present, the ratio of the charge in a seed strip to the charge in an inclusion strip will be symmetric. If crosstalk is present it will shift charge mainly in the same direction as the readout, and the ratio will be asymmetric. If the forwards and backwards crosstalk is equal, then the ratio will also be symmetric. The charge of the individual strips is calculated in adc counts, and the ratio is given by;

$$adc\ ratio = \frac{adc_{high}}{adc_{low}} \tag{6.3}$$

This ratio is calculated for all 2 strip clusters, that are read out by the same Beetle. Clusters where the strips cross a boundary between Beetles are excluded. A plot of the cluster charge ratio for two strip clusters in the *n-in-n* sensor is shown in Figure 6.15. The forwards and backwards distributions are similar. This would suggest that crosstalk is not present in this sensor. For the *n-in-p* sensor, the charge ratio distributions are shown in Figure 6.16, and evidence for crosstalk can be seen. Therefore, the shift in the mean residual could be due to either crosstalk, E_{tran}, or both.

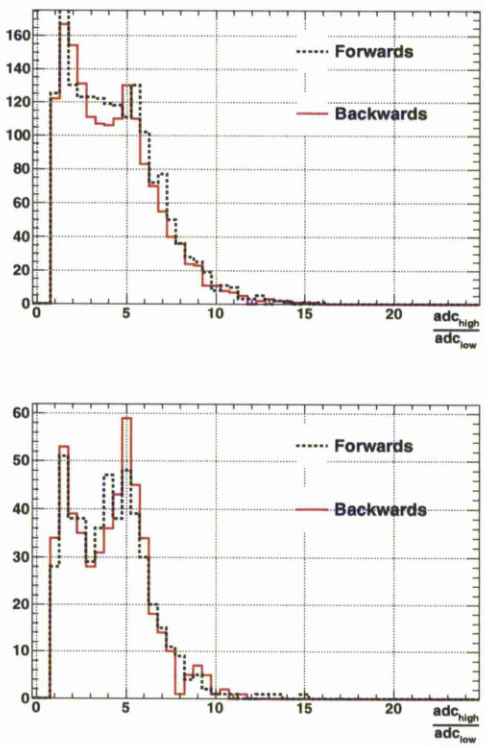

Figure 6.15: The cluster charge ratios for the *n-in-n* sensor in the top and bottom positions.

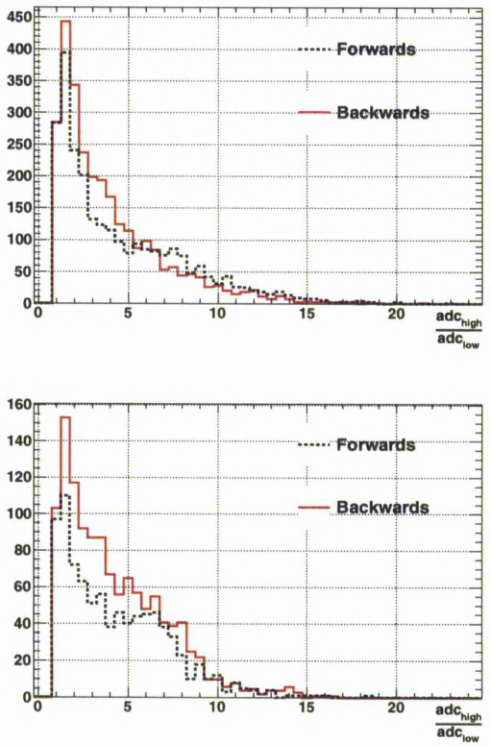

Figure 6.16: The cluster charge ratios for the *n-in-p* sensor in the top and bottom positions.

6.7.2 Results and Discussion

The cause of E_{tran} is a gradient in radiation flux, and since the dose in the top and bottom regions are flat, any shift in the mean residuals in these regions can be solely attributed to crosstalk. In the region of high flux gradient we have maximum sensitivity to E_{tran} in the sensors. The shift in the mean residual,(δ_{μ}) is the sum of the shift due to crosstalk and the shift due to irradiation,

$$\delta_{\mu} =< \delta_{xtalk} > + < \delta_{E_T>} \tag{6.4}$$

We can estimate the cross talk using a data-driven method. We average the shift in the top and bottom region (crosstalk only regions) as an estimate of the crosstalk in the high gradient region,

$$< \delta_{xtalk} >= \frac{\delta_{xtalk\ top} + \delta_{xtalk\ bottom}}{2} \tag{6.5}$$

using the values for the mean residual in Table 6.3 gives the average shift due to crosstalk as,

$$< \delta_{xtalk} >= 4.0\ \mu m\ \pm\ 0.45\ \mu m \tag{6.6}$$

Thus in the high field region, we estimate the shift as being our observed shift minus our crosstalk estimate,

$$< \delta_{E_T} >= \delta_{\mu} - < \delta_{xtalk} > \tag{6.7}$$

and our estimated shift due to E_{tran} is,

$$< \delta_{E_T} >= 2.5 - 4.0 = -1.5\ \mu m\ \pm\ 0.6\ \mu m \tag{6.8}$$

The result shows that contribution to the mean shift in the relative cluster centroids due to E_{tran} is of the order of 1 μm, and comparable to a study using VELO Φ sensors which found the shift in cluster reconstruction position due to E_{tran} to be less than 2 μm [76]. The shift in the relative cluster position due to crosstalk seems larger than that caused by E_{tran}.

6.8 Resolution Of Irradiated Sensors

Knowing that we do not have significant systematic shifts in the cluster reconstruction position due to distortions in the electric field (E_{tran}), we can estimate the resolutions of the irradiated sensors. However, because the effect of alignment on the mean residuals using the pixel telescope is not known, the resolution will be estimated independent of

the pixel system. The spatial resolution of a sensor, is expressed as the uncertainty in the reconstructed position of a cluster. The effects of radiation damage will cause the resolution of the sensors to degrade. Understanding the amount of degradation in the spatial resolution due to radiation damage is vital. This is especially important at the innermost region of the VELO sensors, where the strip pitch is at its smallest (40 μm) and consequently the resolution is expected to be at its best. The innermost region is also is expected to undergo the highest levels of radiation damage.

The aim of this analysis is to estimate the resolution in the high radiation flux region of both the *n-in-n* and *n-in-p* sensors. We attempt to estimate this independent of the pixel system in a unique method that largely depends on the excellent sensor-to-sensor alignment of the R/R module at production. This novel method also takes advantage of the fact that in the R/R module the high radiation flux region of one sensor is adjacent to the low irradiation flux (effectively unirradiated) region of the other sensor; allowing the cluster reconstruction position in the low flux sensor to be used as a reference. In the top position, the *n-in-p* sensor is the reference, and in the bottom position the *n-in-n* sensor is the reference sensor. Using this method the performance of the sensors, after the equivalent of 6 years of nominal running can be evaluated. This method also enables the performance of the different sensors to be compared.

6.8.1 Analysis

The data was taken at 500V, with normal incidence tracks and the beam in the top and bottom positions. The cluster thresholds used are the same as those used previously and summarised in Table 6.2. For a hit to be registered in the irradiated sensor, it is required to be within a radial distance of 50 μm of a hit in the unirradiated sensor, and in the same sector. The cluster reconstruction position is calculated in both sensors using the weighted mean method. The VELO residual (Δ_{velo}) is defined as the difference between a cluster centre in the VELO sensors;

$$\Delta_{velo} = R_u - R_i \tag{6.9}$$

where u denotes the unirradiated sensor, and i the irradiated sensor. Due to the excellent sensor-to-sensor alignment of the R/R module ($\sim$3 μm), the Δ_{velo} distribution results

in a δ function at 0 when one strip clusters are used. This rules out using all clusters, 1v1, 2v1, and 1v2 clusters. Therefore, 2v2 clusters are used in this analysis. The Δ_{velo} distribution is fitted with a Gaussian function and the resolution of the sensor can be extracted from the width of the fit. The width of the fitted Gaussian is the sum of the resolution of the unirradiated sensor (σ_u) and the irradiated sensor (σ_i) added in quadrature;

$$\sigma_{fit} = \sqrt{\sigma_u^2 + \sigma_i^2} \tag{6.10}$$

If an assumption is made that the resolution of the sensors are similar ($\sigma_u \simeq \sigma_i$), the resolution of the irradiated sensor would be;

$$\sigma_i \sim \frac{\sigma_{fit}}{\sqrt{2}} \tag{6.11}$$

But we know this is not the case, because of radiation damage. If the difference in resolution between the two sensors (δ) is assumed to be small $\mathcal{O}(30\%)$; [1]

$$\sigma_i = \sigma_u + \delta\sigma_u \tag{6.12}$$

Substituting back into equation (6.10) gives;

$$\sigma_f = \sqrt{(1 + (1+\delta)^2)}\sigma_u = \sqrt{(2 + 2\delta + \delta^2)}\sigma_u \tag{6.13}$$

neglecting δ^2 since it is small gives;

$$\sigma_f \sim \sqrt{2(1+\delta)} \times \sigma_u \sim \sqrt{2} \times (1 + \frac{\delta}{2}) \times \sigma_u \tag{6.14}$$

[1] Since charge collection after irradiation drops by $\sim$30%, then the resolution of the irradiated sensor being 30% worse is reasonable.

Assuming δ is known the resolution of the unirradiated sensor can be estimated as;

$$\sigma_u \sim \frac{\sigma_m}{\sqrt{2}} \frac{1}{(1+\frac{\delta}{2})} \sim \frac{\sigma_m}{\sqrt{2}}(1-\frac{\delta}{2}) \tag{6.15}$$

and the resolution of the irradiated sensor can be estimated as;

$$\sigma_i = (1+\delta)\sigma_u \sim \frac{\sigma_m}{\sqrt{2}}(1+\frac{\delta}{2}) \tag{6.16}$$

In the case where the two sensors are assumed to have the same resolution, we would systematically measure the resolution of the unirradiated (irradiated) sensor to be too high (low) by a factor of $\frac{\delta}{2}$. Starting with the assumption that the unirradiated sensors have the same resolution, we can test the hypothesis that the irradiated *n-in-n* and *n-in-p* sensors have the same behaviour after irradiation. We can do this by comparing the resolution of the irradiated *n-in-n* sensor (top position) and the irradiated *n-in-p* sensor (bottom position), using equation (6.11). If the resolution of one sensor is a lot worse after irradiation, then the resolution will be radically different.

6.8.2 Results and Discussion

The estimated sensor resolution is plotted against strip pitch for each of the beam positions, shown in Figure 6.17 and Figure 6.18. The plots also include a dashed line indicating binary resolution of $\sigma = pitch/\sqrt{12}$. A linear fit to the data points give a parameterisation of the sensor resolution as a function of pitch, these summarised are in Table 6.4.

Beam Region	Irradiated Sensor	Parameterisation	Resolution at 40 μm
Top	*n-in-n*	$5.36+0.09 \times (pitch - 40)\mu m$	5.36 ± 0.40 μm
Bottom	*n-in-p*	$4.42+0.16 \times (pitch - 40)\mu m$	4.42 ± 1.60 μm

Table 6.4: A table summarising the results for the resolution in the top and bottom positions.

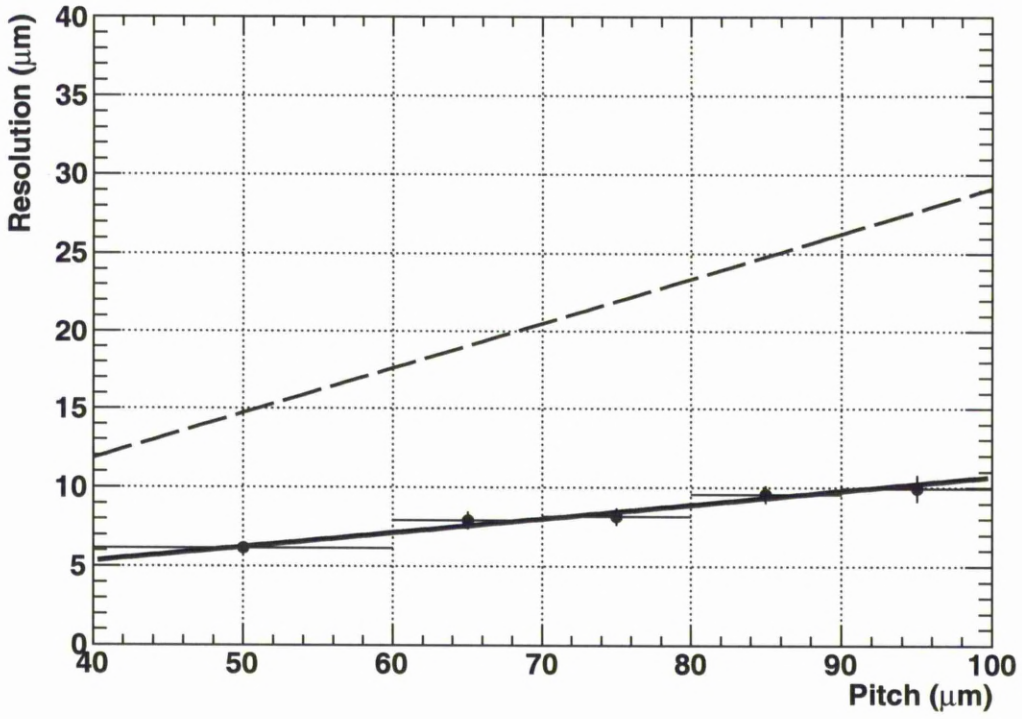

Figure 6.17: Resolution vs pitch in the top beam position. Due to low statistics, the data in pitch region 40-50 μm and 50-60 μm have been combined. The dotted line indicates binary resolution.

The results show that the estimated resolution of the irradiated *n-in-n* sensor at a pitch of 40 μm is 5.36 $\pm$0.40 μm, and the resolution of the *n-in-p* sensor in the same conditions is shown to be 4.42 $\pm$1.60 μm. The results also show that the estimated resolution is better than binary resolution of $\frac{40}{\sqrt{12}} = 11.5\mu m$. This is expected since only hits with two strip clusters in both sensors (2v2) are used.

Since the results of the sensor resolution after irradiation are obtained using 2v2 clusters, to allow comparison with the results obtained without the condition of 2v2 clusters, an estimation of the total resolution can be made. This is done by weighting the resolution due to binary cluster by the fraction of binary clusters, and weighting the resolution due to charge sharing by the fraction of two strip clusters and is given by;

$$\sigma_{tot}^2 = \sigma_1^2 f_1 + \sigma_2^2 f_2 \tag{6.17}$$

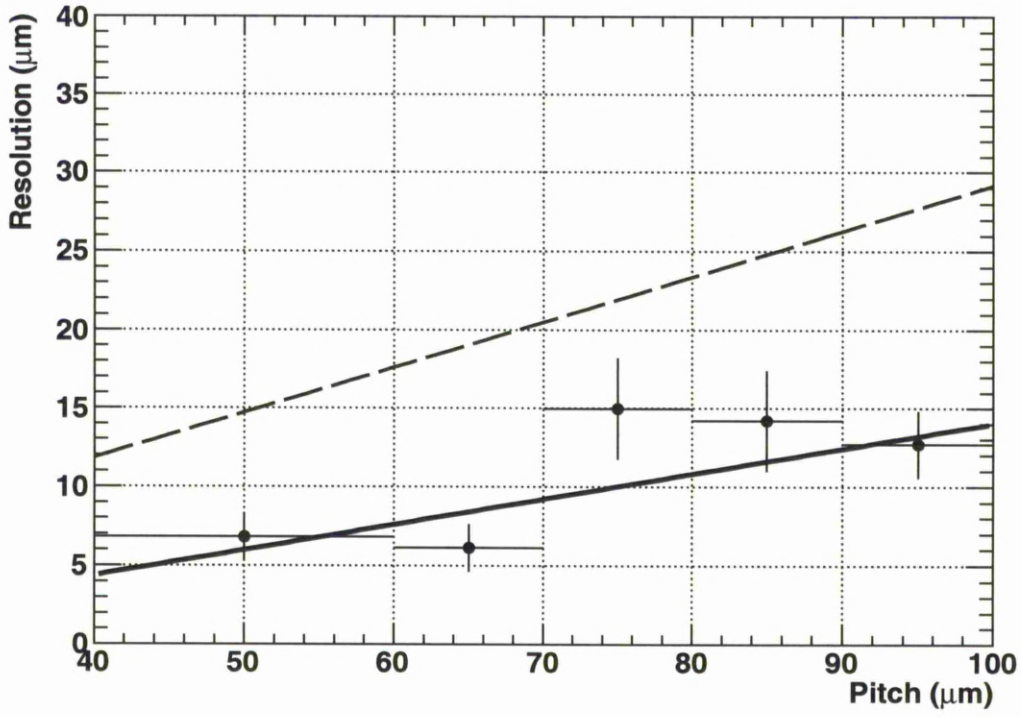

Figure 6.18: Resolution vs pitch in the bottom beam position. Due to low statistics, the data in pitch region 40-50 μm and 50-60 μm have been combined. The dotted line indicates binary resolution.

where σ_1 is the resolution due to one strip clusters, and σ_2 is the resolution due to two strip cluster. The fraction of one strip cluster is f_1, and the fraction of two strip clusters is f_2. In the testbeam data used for this study 70% of clusters are binary and 30% are due to charge sharing. We can make an estimation of the total resolution at a pitch of 40 μm for the *n-in-n* sensor as;

$$\sigma_{tot} = \sqrt{0.7 \times \left(\frac{40}{\sqrt{12}}\right)^2 + 0.3 \times 5.36^2} \tag{6.18}$$

$$\sigma_{tot} = 10.1 \pm 0.4 \ \mu m \tag{6.19}$$

The estimation gives a result of 9.9 ± 1.6 μm for the *n-in-p* sensor at a pitch of 40 μm. The estimated resolutions for the *n-in-n* and *n-in-p* sensors are consistent. The estimated total resolution can be compared to the resolution of the VELO sensors at 40 μm pitch measured using the full VELO detector before radiation damage in Figure 6.19. This gives a resolution to be ~ 9 μm at a pitch of 40 μm for tracks with a projected angle between 0-4 °.

The estimated resolutions from charge sharing clusters (2v2) for the irradiated *n-in-n* and *n-in-p* sensors indicate that we are close to the best resolution even after irradiation. The results obtained for the two different sensor technologies are also consistent. The charge sharing resolution can be compares the resolution of the VELO detector with projected angle between 7-11 °. With increased projected angle, the charge sharing increases giving higher resolution. In the full VELO detector we get a resolution of ~ 4 μm, with the higher track angle. The charge sharing resolution in the test beam is consistent with this result even after irradiation.

6.9 Summary

To understand the effects of radiation damage on VELO sensors, a non-uniformly irradiated RR module was investigated in a proton testbeam. The VELO will operate in the harshest radiation environment of all the LHC subdetectors, due to its close proximity to the interaction point. Due to the unique arrangement of the VELO sensors the irradiation will be non-uniform, which can cause a transverse electric field. The transverse electric field can cause a distortion in the cluster reconstruction position, towards the region of higher dose. This shift has been shown to be ≤ 1 μm. The resolution of the irradiated sensors at the innermost pitch has been measured to be ~ 5 μm for the *n-in-n* sensor and ~ 4 μm for the *n-in-p* sensor using charge sharing clusters. An estimation has been made of the total resolution of the sensors and found to be ~ 10 μm for both sensors.

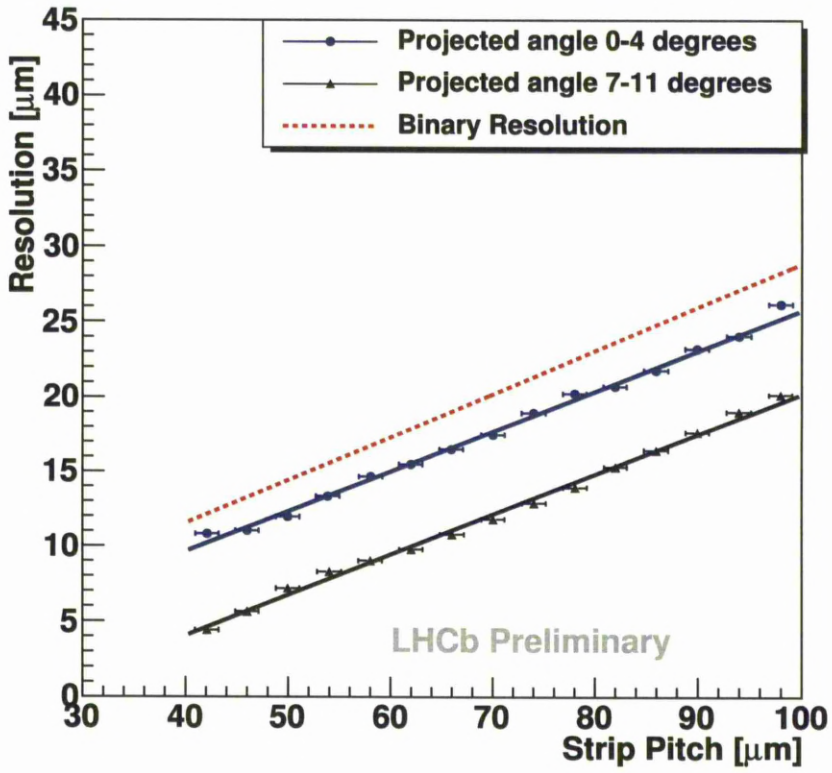

Figure 6.19: Resolution vs pitch for R sensors in the VELO. The red dotted line indicates binary resolution.

Chapter 7

The Performance of the VELO During Operation

7.1 Introduction

LHCb is dedicated to heavy flavour physics at the LHC. Its primary aim is to discover new physics through precision studies of CP-violation and rare decays of beauty and charm hadrons. The VELO provides measurements of track co-ordinates which are used to identify the secondary vertices which are a distinctive feature of B-hadron and C-hadron decays. The detector design is optimised for the physics programme of LHCb, and needed to take into account the following features of the processes studied or searched for:

- **Angular Coverage.** The detector is designed to cover the forward region, and has measured the $b\bar{b}$ cross-section to be $(75.3 \pm 5.4 \pm 13.0)$ μb [78] in the range $2 < \eta < 6$. This represents 27% of the total cross-section (obtained from Pythia [31]), while only covering 1.8% of the solid angle. All tracks inside the nominal LHCb acceptance of 15-300 mrad cross at least three VELO stations.
- **Triggering.** The reconstruction of the primary vertex and the displaced secondary decay vertex of a heavy flavour hadron in the VELO is a key ingredient of the high level trigger which reduces the data from a 1MHz event rate to a few kHz.
- **Efficient and Accurate Track Reconstruction.** The precision of the determination of the track parameters, relying on the VELO cluster determination and

alignment and the momentum determination in the other trackers, has allowed a number of world best mass measurements to be made with early data [79].

- **Displaced Tracks and Vertices.** Excellent vertex resolution is essential to the LHCb physics programme. Most analyses rely heavily on selection cuts on the distance with which tracks approach the primary vertex (impact parameter) and the displaced vertex reconstruction with the VELO to identify the signal channels. The impact parameter resolution was optimised by positioning the VELO sensors as close as permitted by safety consideration to the LHC beam; having a small strip pitch at the innermost of the VELO sensors; and reducing the amount of material traversed by a particle before the first measured hits in the VELO.
- **Proper-time.** The proper-time of a decay is obtained from the measurement of the decay distance in the VELO. This is required for lifetime measurements [80] and, critically, for time dependent measurements in the rapidly oscillating B_s^0-$\overline{B}_s^0$ meson system [81, 82].

This chapter reports on the performance of the LHCb detector over the first period of LHC physics operation up till July 2011. Section 7.2 describes the performance and monitoring of the radiation damage in VELO sensors. Sections 7.3 and 7.4 provide the system performance results, with the former section providing detector performance related results and the latter physics performance related results.

7.2 Radiation Damage Studies

7.2.1 IV Monitoring

IV scans are taken on a weekly basis allowing the monitoring of the currents as a function of time. Trending plots can be generated based on these to display the changes in the currents drawn by the sensors as a function of luminosity delivered to the experiment, annealing periods, and similar other scenarios in which the silicon may be affected. For reference, the trending is done on the current at $150\,V$ as this is past the depletion voltage for all the sensors, and allows the time range presented to be from unirradiated sensors to the latest data. An example of the trending mechanism for a module is shown in Figure 7.1.

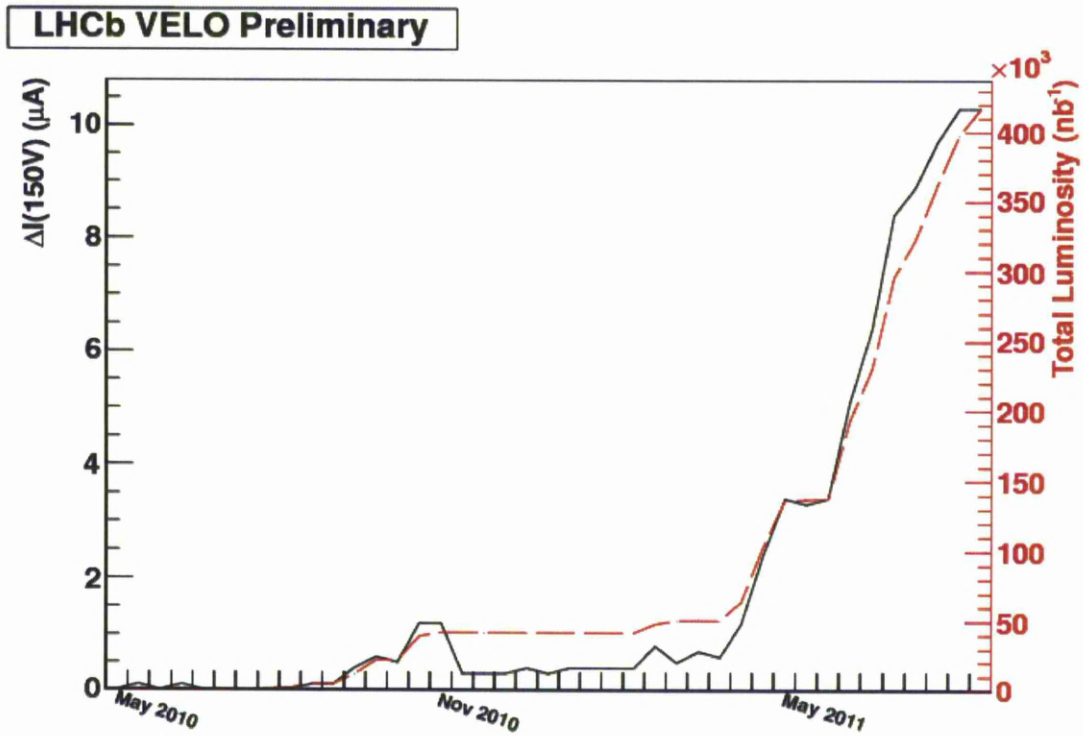

Figure 7.1: An example VELO module (using a p-type sensor) displaying the trending mechanism. The y-axis is the change in current relative to the value in the first time bin. Annealing features for the winter shutdown (around the November 2010 bin) and the chiller tests (May 2011 bin) are present.

There are two distinct bands of sensors in the VELO, corresponding to sensors that are nominally within expectations (in terms of the current drawn) and sensors with high production currents. The two bands of sensors present have behaved very differently over the last $460\,\mathrm{pb}^{-1}$ and they are now beginning to normalize and become dominated by the radiation damage as opposed to any production effects. Annealing features can be observed around the November 2010 and May 2011 data points, corresponding to the winter shutdown (with 49 days at room temperature) and chiller tests for 3 days respectively, giving noticeable annealing effects in the currents as presented in Figure 7.2.

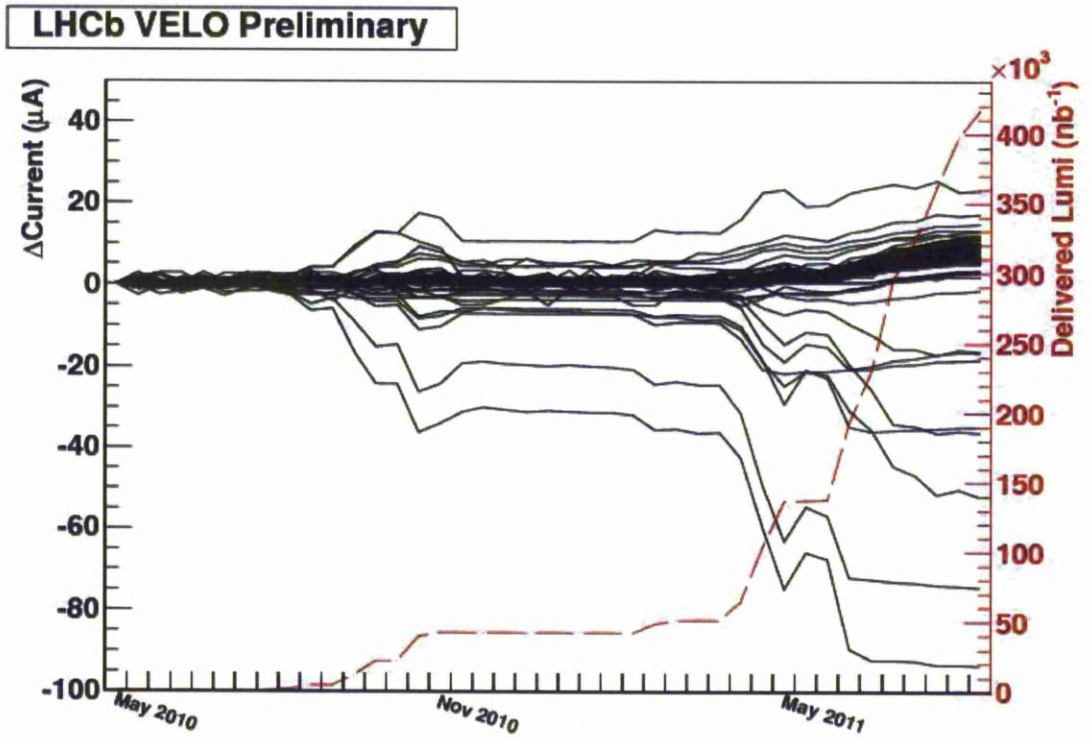

Figure 7.2: A summary of every sensor in the LHCb VELO. The vast majority are within expectations entirely, only showing notable recent current rises with the recent large increases in radiation damage, and a few sensors show significant negative change in currents with radiation damage, these correspond to the high production current sensors.

7.2.2 Charge Collection Efficiency

The nominal operational voltage of the VELO sensors is 150 V. For the CCE analysis, collision data is recorded with every fifth module operated at a voltage ranging between 0 and 150 V. The remaining modules are maintained at the nominal 150 V bias. Sensors with variable voltage are referred to as 'test' sensors. The test sensors are removed from the reconstruction algorithms such that only hits from the 150 V operated sensors are used to reconstruct particle tracks. A track is extrapolated to a coordinate on the test sensor and the set of five strips nearest to this coordinate are searched for deposited charge. This provides unbiased information on the amount of charge deposited by the particle as a function of bias voltage. At each bias voltage the pedestal subtracted ADC distribution is fitted using a Gaussian convoluted with a Landau function. This is used to determine the Most Probable Value (MPV) of the ADC distribution. At large bias

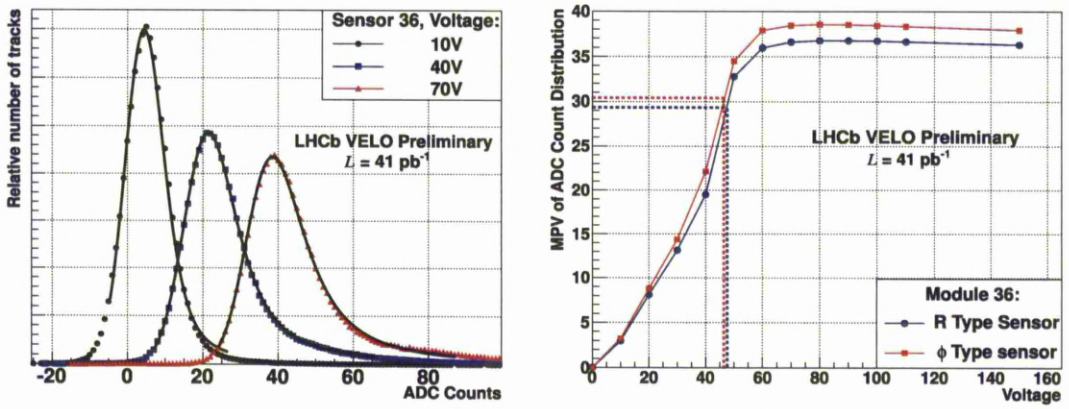

Figure 7.3: Left: Three example collected charge distributions for sensor 36 with the result of the fit to each distribution overlaid. **Right:** MPV value of charge distributions as a function of applied voltage for sensors 36 and 100 (module 36). The dashed lines mark the EDV for each sensor.

voltages the MPV of the ADC distribution reaches a plateau. The EDV is defined as the voltage at which the MPV of a sensor is equal to 80% of the plateau ADC value, as shown in Figure 7.3. The threshold of 80% was chosen as it gives closest agreement with depletion voltages determined from CV measurements.

Between April 2010 and October 2011 five dedicated CCE scans were taken, corresponding to delivered luminosities of 0, 0.04, 0.43, 0.80 and 1.22 fb^{-1}. The change in EDV with irradiation for an *n-in-n* sensor is shown in Figure 7.4(a). The EDV is found to initially decrease with fluence across all radial regions, as expected. The decrease is largest in the inner radial region of the sensor, consistent with expectations that this region is exposed to higher fluence. The innermost region undergoes an increase in EDV between 0.80 and 122 fb^{-1} of delivered luminosity, indicating that this part of the sensor has type inverted. The *n-in-p* sensors exhibit a decrease in EDV with initial fluence, as shown in Figure 7.4(b). This initial EDV decrease is understood to be caused by oxygen induced removal of boron interstitial acceptor sites, an effect that has been previously observed elsewhere [83][84]. The global change in EDV is determined by combining the data from all of the VELO sensors and shown in Figure 7.5.

The minimum EDV observed for any sensor is $\sim$18 V, indicating that upon reaching this EDV the silicon bulk undergoes type inversion. From this we interpret that the *n-in-n* sensors share a common fluence at which type inversion occurs at approximately (10-15)x10^{12} Mev n_{eq}. The fact that the minimum measured EDV is $\sim$18 V demonstrates

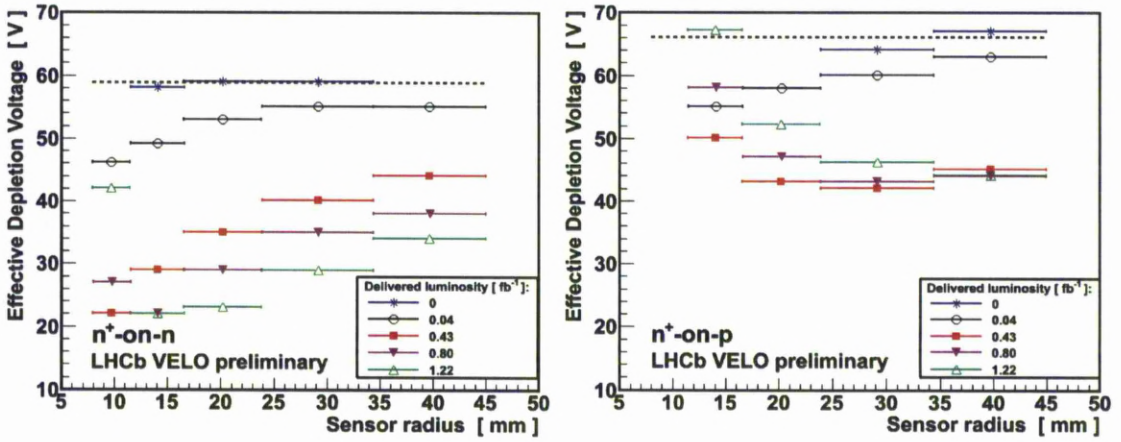

Figure 7.4: Left: The EDV against sensor radius for an *n-in-n* sensor for each of the CCE scan samples. The dashed line shows the mean EDV across all radius regions prior to sensor irradiation, where some 0 fb^{-1} data points are not present due to low statistics. Initial radiation damage results in a decrease in EDV, most significantly in the inner radius regions. Between 0.80 fb^{-1} and 1.22 fb^{-1} the EDV in the innermost radius region increased by 20 V, suggesting that this part of the sensor has type inverted. **Right:** A similar plot for the *n-in-p* sensor. The minimum EDV is 40 V, which is significantly higher than the minimum at 20 V observed for the *n-in-n* sensor.

the limit at which the direct comparison between the EDV and depletion voltage breaks down. The minimal EDV is dictated by the smallest potential difference required to collect charge from the silicon strips, which in turn depends on the shaping time of the electronics. However the true depletion voltage is expected to have decreased to a value closer to 0 V. The behaviour after inversion is found to be independent of the initial EDV of the sensor. The subsequent increase in voltage is approximately linear with further fluence. Figure 7.5 shows the EDV vs fluence for different regions of the sensors, where the dashed box correspond to data from the *n-in-p* sensors.

7.3 Detector Performance

7.3.1 Signal to Noise

The signal induced on at a sensor is amplified and digitised by the Beetle, repeater board, TELL1 readout chain. The function used to estimate the response is a Landau convolved with a Gaussian fitted around the peak region. The most probable value

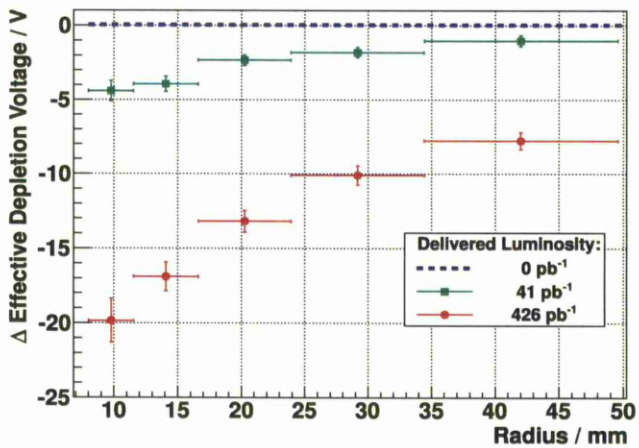

Figure 7.5: The change in EDV with respect to the initial EDV measured prior to radiation exposure, where radius regions have been averaged over all VELO sensors.

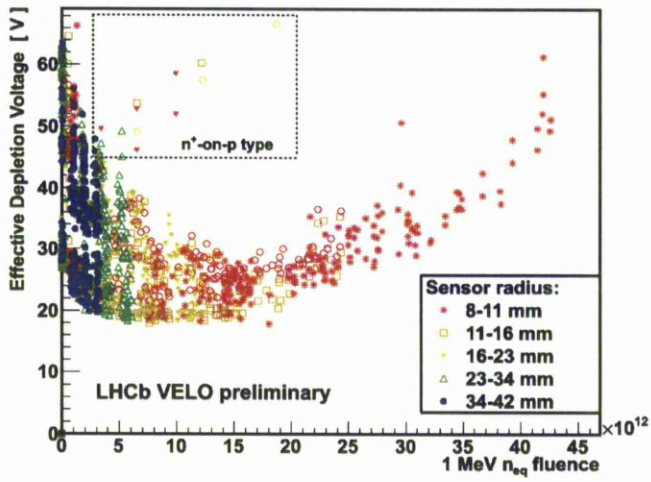

Figure 7.6: The EDV against fluence for different radial regions of VELO sensors. Data from all CCE scans is displayed. For many sensors the inner radius regions have type inverted.

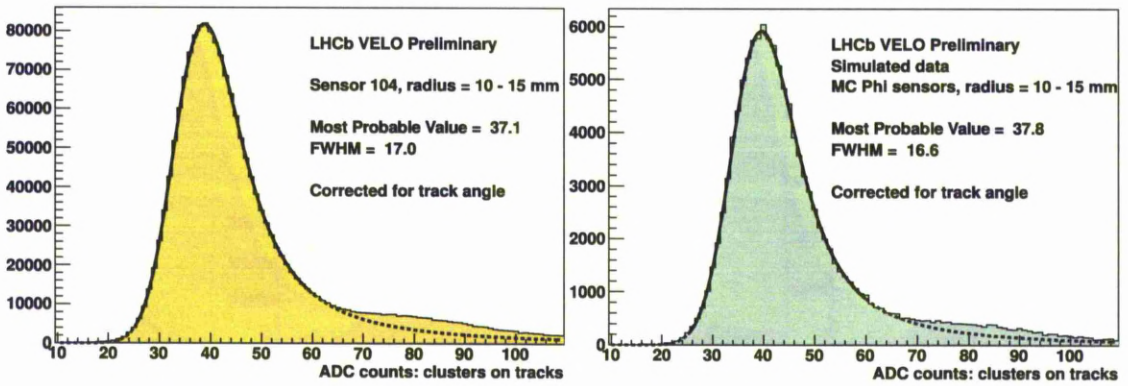

Figure 7.7: Left: Fit to the charge distribution for Sensor 104 (a Φ sensor) for clusters on long tracks with an impact point $10 < r(\text{mm}) < 15$. Right: Same fit for the simulated data in the Φ sensors between $10 < r(\text{mm}) < 15$. In both plots the cluster size is normalized to a track crossing $300\mu m$ of silicon.

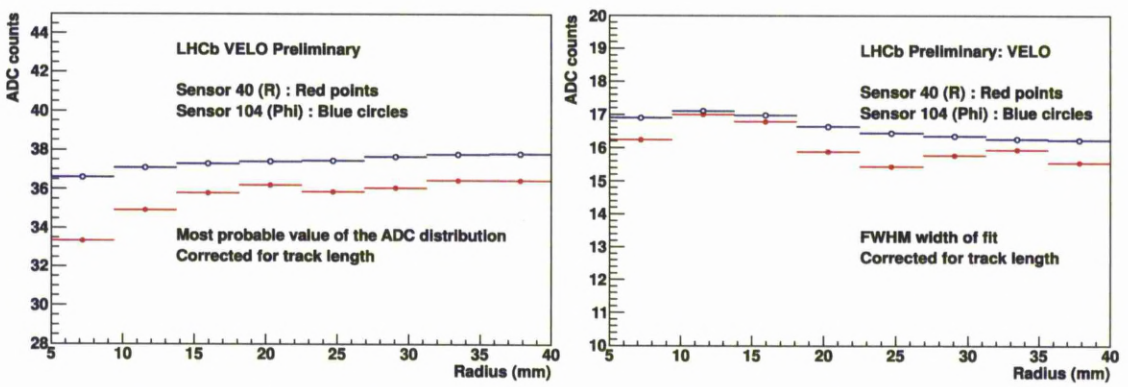

Figure 7.8: The most probable value (left) and full width at half maximum (right) of the fits to sensor 40 (R) and sensor 104, the Φ sensor of the same module, as a function of impact point radius. The cluster sizes were normalized to a track crossing $300\mu m$ of silicon.

(MPV) of the Landau distribution varies as a function of track radius, see Fig. 7.7 for an example of the fit and the values of the fit versus radius are shown in Fig. 7.8. Also shown in Fig. 7.7 is the distribution of ADC counts from LHCb simulated events.

The simulation has been tuned to match the detector response. The GEANT4 [85] simulated energy deposition is distributed amongst the strips crossed by the cluster and the strip noise is added before a digitization is applied. A global scaling is applied to normalize the peak between data and simulation with a correction for the variation in signal size with radius, the FWHM comes out almost the same as well and does not require any additional smearing of the detector response.

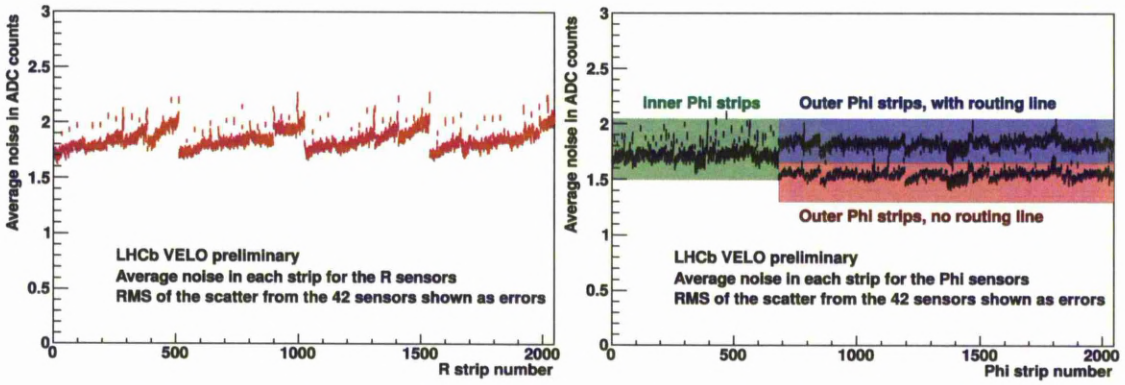

Figure 7.9: Noise in ADC counts averaged across the 42 installed R (left) and Φ (right) sensors, with the error bars indicating the RMS of the distribution.

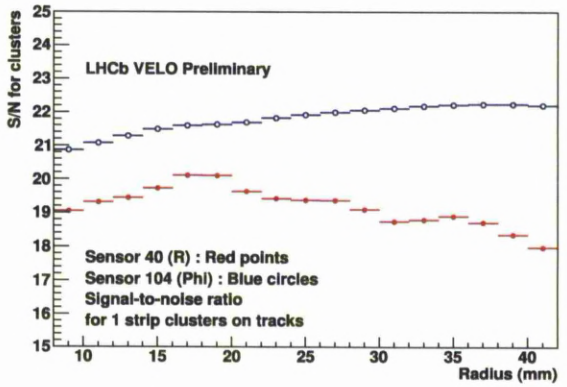

Figure 7.10: Signal to noise ratio from the MPV of the signal for single strip clusters on tracks divided by the noise of that strip. Shown are the S/N values for sensor 40 (R) and sensor 104, the Φ sensor of the same module, as a function of impact point radius.

The noise measured in the sensors is a function of the strip capacitance and gets larger with radius for the R sensors. The Φ sensor has two zones and the strips are equal sizes in each, however in the outer strips every alternate strip is under the routing line for an inner strip so the capacitance is larger. See Fig. 7.9 for the measured noise in the detector averaged over all sensors of each type. There is an issue where the digital header information is not fully isolated from the first channel in each analogue readout link of 32 channels, this is visible as higher noise in these channels.

The signal-to-noise ratio varies as both the noise and the signal MPV vary between sensors and within the sensor between strips, see Fig. 7.10.

7.3.2 Resolution

The hit resolution in silicon devices mainly depends on the strip pitch and the projected angle[1] of the track producing the hit. This angle strongly affects the charge sharing between the neighbouring strips. The resolution improves with increasing this angle because the charge spreads over several strips and reaching the optimal resolution when the tracks cross the width of one strip when traversing the sensor. Above the optimal angle the resolution begins to deteriorate because the signal over noise level on individual strips may drop below threshold due to the large numbers of strips. For the VELO the optimal projected angle varies between about 7° for 40 μm pitch strips and about 18° for 100 μm pitch strips.

The hit resolution is determined by the hit residuals evaluated using the LHCb Kalman filter track fit including the correction for multiple scattering and energy loss accordingly with the track momentum. The residual is defined by the distance between the hit measurement[2] and the extrapolated point to that sensor of the fitted track including the hit measurement. Using the point for which the residual is being determined in the track fit gives rise to a bias in the residual. This has been corrected to evaluate the hit resolution.

The resolution has been determined as function of the strip pitch and of the projected angle. For each bin, the resolution has been determined from the sigma of a Gaussian fit to the distribution of the corrected residuals. The resolution is evaluated using long tracks for which the momentum measurement is available. The following track selection is applied:

- $\chi^2_{track}/\text{ndof} < 5$ to reject the ghosts track and bad quality track. Only 0.2 per mille of tracks are rejected with this cut.
- Hits number between 10 and 30 (corresponding to 5 and 15 space points) to exclude ghost tracks and halo particles affected by a large multiple scattering effect.
- Minimum momentum of 10 GeV/c to reject tracks with a not negligible multiple scattering effect.
- Maximum momentum of 5 TeV/c to avoid unreal tracks.

[1]The projected angle is the angle between the track and the strip in the plane perpendicular to the sensor.

[2]The hit position is given by the weighted mean of the strip positions, where the weight is defined by the charge collected by each strip.

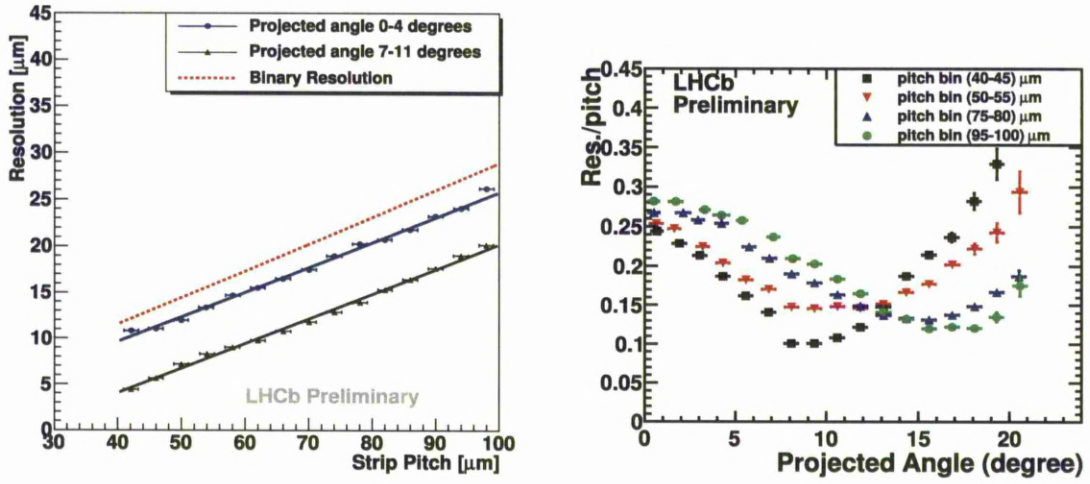

Figure 7.11: The VELO resolution for the R sensors as a function of the readout pitch compared with binary resolution (on the left), and as function of the projected angle for four different strip pitches (on the right).

The hit resolution has a linear dependence with the strip pitch in projected angle bins, as shown in Fig. 7.11. The hit resolution at small projected angles, almost perpendicular to the sensor, has a resolution near to the binary one. A significantly better resolution is measured for large projected angles for which the charge sharing between adjacent strips is optimal. The hit resolution as function of the projected angle is shown in Fig. 7.11 and the fraction of one and two strip cluster as function of the projected angle and strip pitch is shown in Fig. 7.12. The best hit precision of about 4 μm was measured for an optimal angle of 8 degrees and a pitch of 40 μm.

The resolution has been extracted using a simple weighted pulse height algorithm for the reconstruction of the cluster position. Additional development of the clustering algorithm is expected to further improve the precision.

7.3.3 Cluster Finding Efficiency

The performance of individual VELO sensors at a particular bias voltage is expected to vary dramatically over the lifetime of the detector. It is vital that each sensor is regularly monitored to ensure that optimal operational parameters are employed. Section 7.2.2 described the special datasets collected to measure sensor radiation damage. This data has been further analysed to measure the clustering efficiency of the detector.

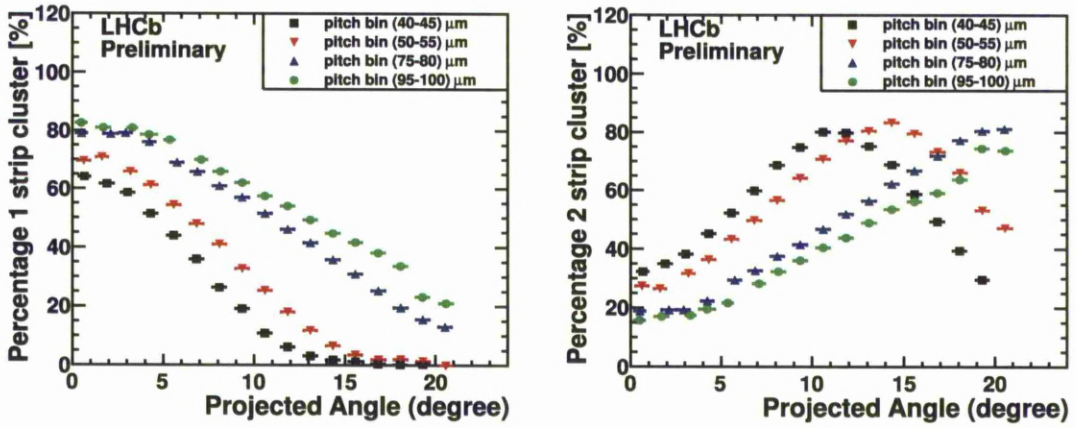

Figure 7.12: The percentage of one (on the left) and two (on the right) strip clusters and as function of the projected angle for four different strip pitches.

The method described in section 7.2.2 was developed to investigate how the most probable value of the charge distributed by a particle varies with sensor bias voltage. This method has also been used to measure the cluster finding efficiency (CFE) of a test sensor. Particle tracks reconstructed using clusters on sensors to either side of the test sensor are extrapolated to a position on the test sensor. If a cluster is located at this extrapolated position then it is assumed to be associated to the particle responsible for the original track. The fraction of tracks for which a cluster is found is defined at the CFE.

Cluster formation depends on the thresholds defined in the cluster making algorithms, which in turn are determined by the experimental signal to noise tolerance. Various track quality selection cuts are applied to reduce the inefficiency attributed due to poor track extrapolation. To measure the intrinsic efficiency of the detector, bad strips are ignored. The CFE for each sensor before significant irradiation is shown by Fig. 7.13. The mean CFE across all sensors with bad strips included and excluded is $99.40\%^{+0.60\%}_{-0.87\%}$ and $99.89\%^{+0.11\%}_{-0.17\%}$, respectively.

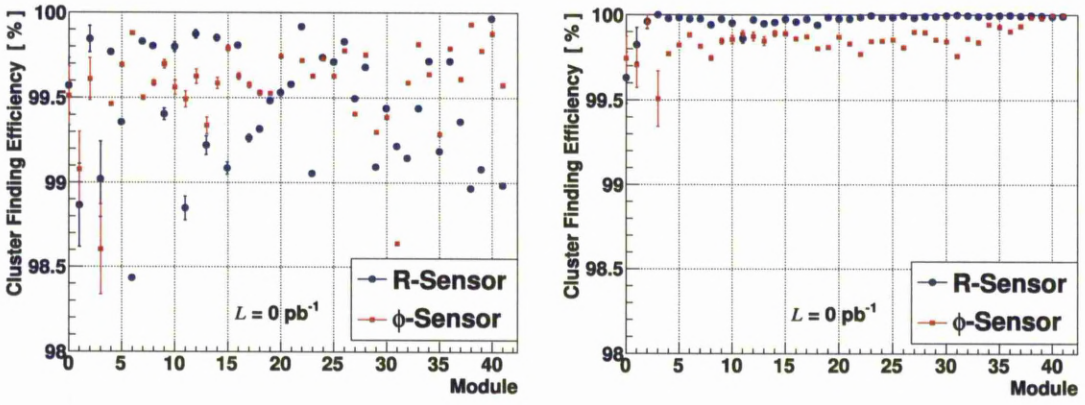

Figure 7.13: The cluster finding collection efficiency for each sensor with all strips (**left**) and also for when identified bad strips are excluded (**right**). The Φ-type sensors have a lower efficiency than the R-type sensors due to the less efficient boundary between the inner and outer Φ-type sensor regions.

7.4 Physics Performance

7.4.1 Impact Parameter

The impact parameter (IP) of a track is defined as the distance between it and the primary vertex at its point of closest approach to the primary vertex. The daughters of a long lived particle, such as the B and D mesons studied in many LHCb analyses, are produced at the decay vertex of their mother, which is generally displaced from the primary vertex. Tracks made by such daughters therefore tend to have larger IPs than those made by particles produced at the primary vertex. Consequently, cuts on IP and IP χ^2 are very effective at excluding prompt backgrounds, and maximising the signal content of a data set. It is thus of great importance for an experiment like LHCb to be able to measure IPs to a high precision, and to have a good understanding of the effects contributing to the resolution of IP measurements.

IP resolutions are governed by three main factors: multiple scattering of particles by the detector material; the resolution on the position of hits in the detector from which tracks are reconstructed; and the distance it is required to extrapolate a track between its first hit in the detector and the interaction point [86]. The angle of deflection of particles, with momentum p, passing through a block of material, of width x and with radiation length X_0, follows a Gaussian distribution with width [87].

$$\sigma_\theta = \frac{0.0136}{p}\sqrt{x/X_0}[1 + 0.038\ln(x/X_0)], \tag{7.1}$$

for p in GeV. When extrapolated over a distance Δ_{01} between the first hit on a track and the primary vertex, this leads to a contribution to the IP resolution of

$$\sigma^2_{IP,MS} = \Delta^2_{01}\sigma^2_\theta. \tag{7.2}$$

If the resolution on the first and second hits on the track are σ_1 and σ_2, and the distance between the primary vertex and the second hit is Δ_{02}, the contribution to the IP resolution from the detector resolution is given by [86]

$$\sigma^2_{IP,hit} = \frac{\Delta^2_{02}\sigma^2_1 + \Delta^2_{01}\sigma^2_2}{(\Delta_{02} - \Delta_{01})^2}. \tag{7.3}$$

Thus, the total IP resolution is given by

$$\begin{aligned}
\sigma^2_{IP} &= \sigma^2_{IP,MS} + \sigma^2_{IP,hit} \\
&= \left(\frac{0.0136}{p}\sqrt{x/X_0}[1 + 0.038\ln(x/X_0)]\right)^2 \Delta^2_{01} + \frac{\Delta^2_{02}\sigma^2_1 + \Delta^2_{01}\sigma^2_2}{(\Delta_{02} - \Delta_{01})^2} \\
&= \left(\frac{0.0136}{p_T}\sqrt{x/X_0}[1 + 0.038\ln(x/X_0)]\right)^2 r^2_1 + \frac{\Delta^2_{02}\sigma^2_1 + \Delta^2_{01}\sigma^2_2}{(\Delta_{02} - \Delta_{01})^2},
\end{aligned} \tag{7.4}$$

using $\Delta_{01}/p = r_1/p_T$, where r_1 is the radius of the first hit. This applies to a 1D IP measurement. In 3D geometry an IP has 2 degrees of freedom - 3 as it is a distance in 3D space, minus 1 from the requirement of being taken at the point of closest approach to the PV. The two underlying variables have identical Gaussian distributions with σ given by equation 7.4, and so the measured IP resolution is decoupled into its 1D x and y components. Due to the forward geometry of LHCb the z component is negligible. An IP measurement in 3D space is thus simply the sum in quadrature of its x and y components, $\sqrt{IP^2_x + IP^2_y}$. The mean offset of such a measurement from its true value is given by the resolution on the 1D components multiplied by $\sqrt{\pi/2}$. Parameterising the resolution of IP_x and IP_y as a function of $1/p_T$ one expects identical, roughly linear distributions

with y-intercept dependent on the detector resolution, and gradient proportional to the material budget.

The vast majority of tracks reconstructed at LHCb are made by particles produced at the PV. The measured IP of such tracks is non-zero only due to the measurement resolution. Thus, the IP resolution can be measured by examining the width of the IP_x and IP_y distributions for all tracks. To do this, only good quality 'Long' tracks (tracks reconstructed in both the VELO and the downstream tracking stations, for the best momentum resolution) from events with only one reconstructed primary vertex are used. The primary vertex is required to have at least 25 tracks included in its fit, to minimise the contribution of vertex resolution to the measured IP. Further, the primary vertex is refitted excluding each track in turn before its IP is calculated, so the track has no influence on the primary vertex position. The IP_x and IP_y are then plotted in bins of the variable of interest, such as $1/p_T$, and a single Gaussian fit performed in each bin. The σ of the fitted Gaussian is taken as the resolution.

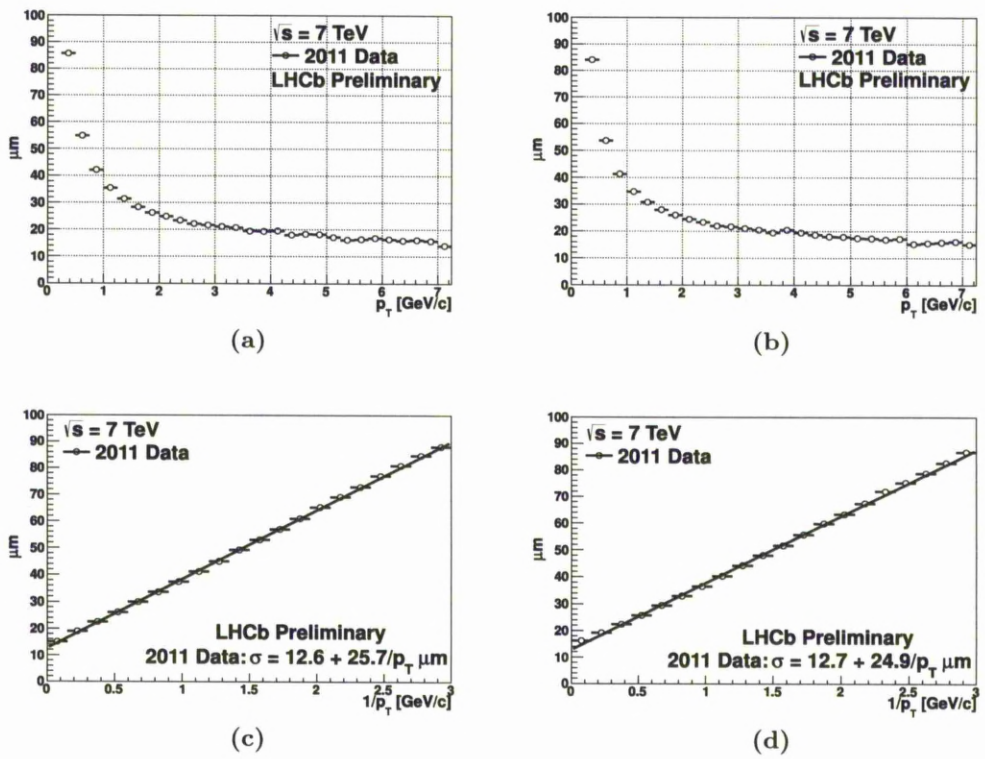

Figure 7.14: (a) IP_x and (b) IP_y resolution as a function of p_T. (c) and (d) show the same as a function of $1/p_T$. Measured on 2011 data.

Figure 7.14 shows the plots of the resolution of IP_x and IP_y against p_T and $1/p_T$. As expected the resolutions of IP_x and IP_y are almost identical. They are asymptotic at high p_T, tending to ~ 13 μm, and depend roughly linearly on $1/p_T$. The performance of the VELO in this respect is excellent, achieving IP resolutions of < 35 μm for particles with $p_T > 1$ GeV.

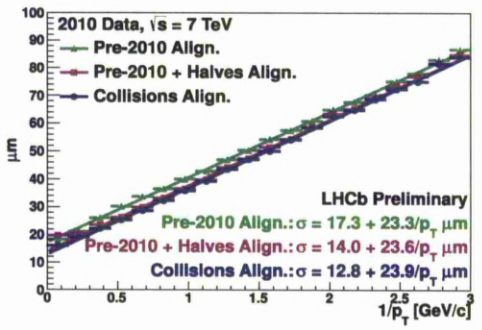

Figure 7.15: IP resolution as a function of $1/p_T$, comparing different qualities of alignment, measured on 2010 data.

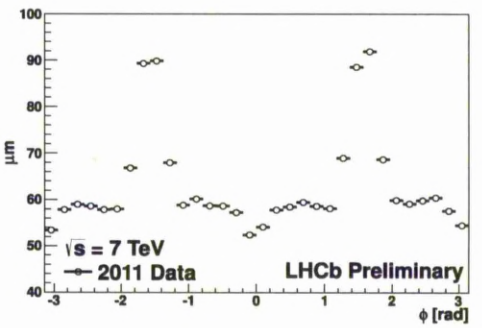

Figure 7.16: IP resolution as a function of azimuthal angle Φ, measured on 2011 data.

To examine the dependence of IP resolutions on detector resolution, the same plot is made using detector alignment data from early in the 2010 data taking period, when the alignment was less well known, as is shown in figure 7.15. The three qualities of alignment compared comprise an alignment determined prior to the 2010 run; the same alignment when the alignment of the VELO halves was re-evaluated using 2010 data; and an alignment in which the module and sensor alignment was also evaluated using 2010 collision data. Poorer alignment means poorer hit resolution, and so, as expected the y-intercept of the IP resolution distribution reduces as the alignment improves, while the gradient remains largely unchanged.

The distribution of material in the VELO is non-uniform, and this also affects IP resolutions. In the region in which the two halves of the VELO overlap the two sides of the aluminium RF foil also overlap, greatly increasing the material density. This can be seen by measuring the IP resolution in bins of the azimuthal angle Φ, as is shown in Figure 7.16. The increase in material is reflected in the increase in IP resolution about $\Phi = \pm\pi/2$, ie in the overlap region.

Thus, it can be seen that the VELO provides exceptionally accurate IP measurements. Further, the IP resolution behaves as expected, with a roughly linear dependence on $1/p_T$,

and clear dependence on both the hit resolution and the distribution of material in the VELO.

7.4.2 Vertex Resolution

LHCb has been designed to study CP violation and rare decays in the B-meson sector. This requires the accurate measurement of decay lifetimes and impact parameters, both for flavour tagging and background rejection. Precise vertex reconstruction is therefore of fundamental importance, in order to resolve production and decay vertices.

The primary vertex resolution is strongly correlated to the number of tracks used to reconstruct the vertex (the track multiplicity), and so is parametrised as a function of this variable. The analysis is performed on an event by event basis. The principle is to reconstruct the same primary vertex twice, and to consider the residual difference between these two points. This is achieved by splitting the track sample of each event into two, and making vertices from each independent set of tracks.

The track splitting is done entirely at random, with no ordering of tracks and no requirement that the same number of tracks are put into each set. The vertex reconstruction is applied to each set of tracks. Vertices are 'matched' between the two sets by requiring that the difference in their z position is < 2 mm.

Then if the number of tracks making a pair of matched vertices is the same, the residual is calculated. Repeating for many events yields a series of residual histograms, giving the positional differences between the vertices in (x, y, z), for varying track multiplicity.

In practice, the number of tracks making a vertex ranges from 5 (the required minimum) to around 100. However, given the track splitting method roughly divides the total number of tracks in two, it is difficult to measure the resolution past 40 tracks. Each residual histogram is fitted with a Gaussian. The resolution for each particular track multiplicity is calculated as the σ of the fitted Gaussian divided by $\sqrt{2}$, as there are two uncorrelated resolution contributions in each residual measurement.

The resolution is fitted with a function which parametrises it in terms N (the track multiplicity):

$$\sigma_{PV} = \frac{A}{N^B} + C \tag{7.5}$$

C can be thought of as the best resolution possible, given multiple scattering. A is a constant multiplier, and B shows the dependence on track multiplicity.

In 2011 data it was found that a 25 track vertex has a resolution in the transverse plane of 13 microns. In z the resolution is 71 microns, see Figure 7.17.

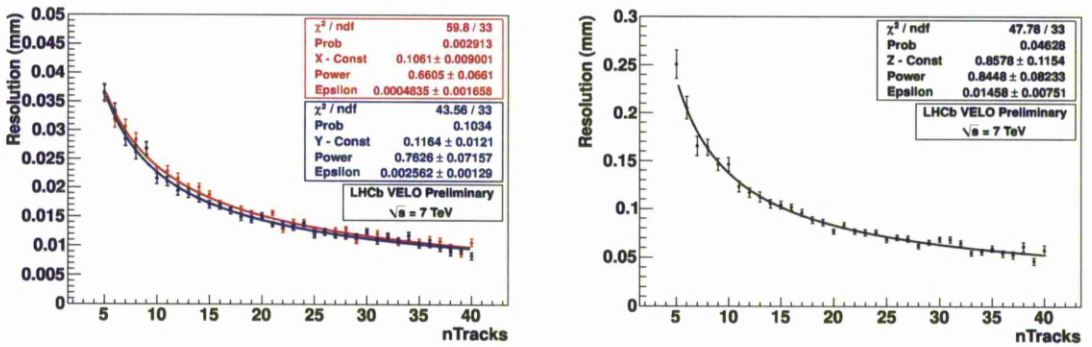

Figure 7.17: Resolution of events with exactly 1PV from 2011 data, as a function of track multiplicity. Left: comparison of x (red) and y (blue) resolution. Right: z resolution.

The same track split method was applied to MC10 Monte Carlo, see Figure 7.18. In the transverse plane, the vertex resolution in Monte Carlo is approximately 2 microns better than in data. The track split method was verified in Monte Carlo using truth information. No significant bias was seen. A summary of all vertex resolution figures can be found in Table 7.1.

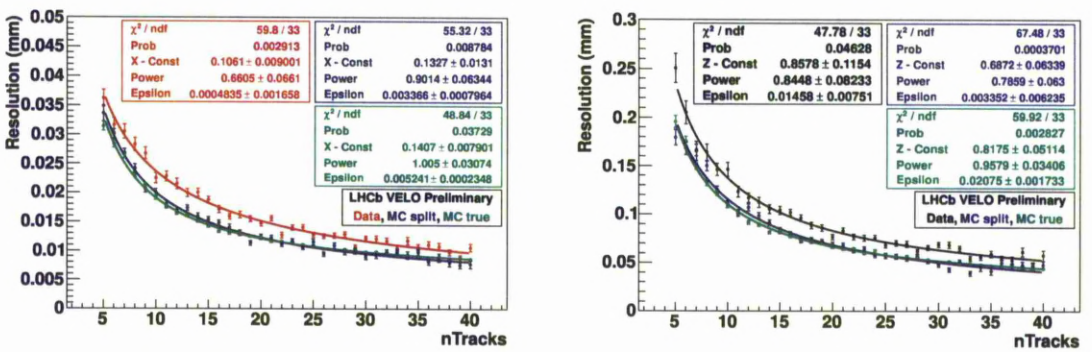

Figure 7.18: Resolution of events with exactly 1PV as a function of track multiplicity. Data is compared with Monte Carlo using the split method (purple) and truth (green).

25 Track Resolution	x	y	z
Data - split	13.1	12.5	71.1
MC - split	10.7	10.9	58.1
MC - truth	10.8	10.8	58.2

Table 7.1: 25 track PV resolutions for data and Monte Carlo using the track split method, and using Monte Carlo truth information.

7.5 Summary

The VELO is fully operational and is performing well. The performance of the sensors was predicted to degrade due to radiation damage, and the effects of radiation damage have been observed in the VELO sensors. Type inversion has been observed in the n-type bulk of the *n-in-n* sensors. The monitoring of the sensor currents, depletion voltages and charge collection efficiencies will be an important part of tracking the performance of the sensors. The resolution of the sensors has been found to be 4 μm at a pitch of 40 μm and angle of 8°. The impact parameter (IP) resolution can be parameterised in the x component to be σ_x =12.6+25.7/p$_T$ μm, and in the y component to be σ_y =12.7+24.9/p$_T$ μm. The primary vertex resolution (PV) has been measured to be $\sim$13 μm in the longitudinal direction for 25 tracks. The accurate determination of the IP is very important for LHCb. The relationship between the IP and the PV for a particle is used in the trigger as cut in many physics analyses.

Chapter 8

Conclusion

The VELO is the principal tracking and vertexing detector for the LHCb experiment. The ability to reconstruct primary and secondary vertices is crucial to the physics performance of LHCb. The majority of physics analyses at LHCb rely on cuts on the distance with which tracks approach the primary vertex (the impact parameter), and the displaced vertex reconstruction with the VELO. To achieve the best possible impact parameter and vertex resolution the VELO is placed as close as possible to the interaction point. This exposes the VELO to high particle flux and requires that the silicon microstrip sensors in the VELO be radiation hard.

The VELO is currently fully functional and performing within expectations. To date $\sim$ 1 fb^{-1} of data has been collected, which corresponds to $\sim$4.5x10^{13} n$_{eq}$ cm^{-2}. The effects of radiation damage on the silicon sensors has been observed. The performance of the detector is expected to start degrading from 2013 onwards. Measures that have been put into place to understand this degradation. The resolution of the sensors has been found to be 4 μm at a pitch of 40 μm and angle of 8°. The impact parameter (IP) resolution can be parameterised in the x component to be σ_x =12.6+25.7/p$_T$ μm, and in the y component to be σ_y =12.7+24.9/p$_T$ μm. The primary vertex resolution (PV) has been measured to be $\sim$13 μm in the longitudinal direction for 25 tracks.

An irradiated VELO RR module with two different sensor technologies, *n-in-n* and *n-in-p* was placed in a proton testbeam. The sensors in the module were irradiated to a flux equivalent to the expected fluence after approximately 6 years of running at nominal conditions at the innermost radius. An analysis on the performance of non-uniformly irradiated VELO sensors, as expected in LHCb has been presented. Analysis has been performed on two parameters that are expected to have large implications on the tracking performance of the VELO. The transverse electric field which could cause

a distortion in the cluster reconstruction position. This shift has been shown to be of the order of 1 μm. The spatial resolution of the irradiated sensors has been estimated at the innermost radius with charge sharing clusters, and shown to be ~ 5 μm for the *n-in-n* sensor and ~ 4 μm for the *n-in-p* sensor. An estimation of the total resolution has also been made and gives a resolution of ~ 10 μm for both sensors. These results are close to expectations and allows LHCb to fulfill its physics potential, with no severe degradation due to the radiation effects in the VELO.

Bibliography

[1] L. J. R. Aitchison and A. J. G. Hey, *Gauge theories in particle physics* (IOP, 2004).

[2] A. Pich, (2007), 0705.4264.

[3] Particle Data Group, J.Beringer *et al.*, Phys. Rev. D **86**, 010001 (2012).

[4] J. H. Christenson, J. W. Cronin, V. L. Fitch, and R. Turlay, Phys. Rev. Lett. **13**, 138 (1964).

[5] J. Kemmer, Nuclear Instruments and Methods **169**, 499 (1980).

[6] B. Zeghbroeck, *Principles of Semiconductor Devices*, Online textbook available at `http://ece-www.colorado.edu/~bart/book`.

[7] H.Spieler, *Semiconductor Detector Systems* (Oxford University Press, 2005).

[8] G. Lutz, *Semiconductor Radiation Detectors* (Springer, 1999).

[9] S. Sze, *Semiconductor Devices* (John Wiley & Sons, 2002).

[10] W. Leo, *Techniques for Nuclear and Particle Physics Experiments* (Springer, 1994).

[11] L. Landau, J. Physics **8**, 201 (1944).

[12] H. Boesch and F. McLean, IEEE Trans. Nucl. Sci. **32**, 3940 (1985).

[13] H. Boesch and T. Taylor, IEEE Trans. Nucl. Sci. **31**, 1273 (1984).

[14] J. Srour *et al.*, IEEE Trans. Nucl. Sci. **50**, 653 (2003).

[15] A. V. Ginneken, *Non Ionising Energy Deposition in Silicon for Radiation Damage Studies* (Fermilab National Accelerator Laboratory, 1989), FERMILAB-FN-522.

[16] M. Moll, *Radiation Damage in Silicon Particle Detectors*, PhD thesis, University of Hamburg, Hamburg, 1999.

[17] G. Lindstrom and others., Nucl. Instr. and Meth. A **466**, 308 (2001).

[18] G. Kramberger *et al.*, Nucl. Instr. and Meth. A **571**, 608 (2007).

[19] G. Casse, *The effect of hadron irradiation on the electrical properties of particle detectors made from various silicon materials*, PhD thesis, Universite Joseph Fourier-Grenoble 1, 1998.

[20] G. Casse, P. Allport, and A. Greenall, Nucl. Instr. and Meth. A **581**, 318 (2007).

[21] G. Casse, P. Allport, and A. Watson, Nucl. Instr. and Meth. A **568**, 46 (2006).

[22] R. H. Richter *et al.*, Nucl. Instr. and Meth. A **377**, 412 (1996).

[23] M. Hanlon, *The Developminet of p-type Silicon Detectors for the High Radiation Regions of the LHC*, PhD thesis, University of Liverpool, Liverpool, 1999.

[24] L. Evans and P. Bryant, JINST **3**, S08001 (2008).

[25] The ATLAS Collaboration, JINST **3**, S08003 (2008).

[26] The CMS Collaboration, JINST **3**, S08004 (2008).

[27] The LHCb Collaboration, JINST **3**, S08005 (2008).

[28] The ALICE Collaboration, JINST **3**, S08002 (2008).

[29] E. Norrbin and T. Sjostrand, The European Physical Journal C-Particles and Fields **17** (2000).

[30] J. van Tilburg, *Track simulation and reconstruction in LHCb*, PhD thesis, VU University, Amsterdam, 2005.

[31] T. Sjostrand, S. Mrenna, and P. Z. Skands, JHEP **0605**, 026 (2006), hep-ph/0603175.

[32] The LHCb Collaboration, *LHCb VELO Technical Design Report* (CERN, Geneva, 2001), CERN/LHCC 2001-011.

[33] The LHCb Collaboration, *LHCb Reoptimized Detector Design and Performance Technical Design Report* (CERN, Geneva, 2003), CERN/LHCC 2003-0301.

[34] The LHCb Collaboration, *LHCb Inner Tracker Technical Design Report* (CERN, Geneva, 2002), CERN/LHCC 2002-029.

[35] The LHCb Collaboration, *LHCb Outer Tracker Technical Design Report* (CERN, Geneva, 2001), CERN/LHCC 2001-024.

[36] R. E. Kalman, Journal of Basic Engineering **82**, 35 (1960).

[37] R. Fruhwirth, Nucl. Instr. and Meth. A **262**, 444 (1987).

[38] E. Rodrigues, *Tracking Definitions* (CERN, Geneva, 2007), LHCb-2007-006.

[39] The LHCb Collaboration, *LHCb RICH Technical Design Report* (CERN, Geneva, 2000), CERN/LHCC 2000-037.

[40] The LHCb Collaboration, *LHCb Calorimeter Technical Design Report* (CERN, Geneva, 2000), CERN/LHCC 2000-036.

[41] A. Arefev *et al.*, CERN Report No. LHCb-2007-149. CERN-LHCb-2007-149, 2008 (unpublished), revised version submitted on 2008-05-15 09:09:53.

[42] C. Coca *et al.*, CERN Report No. LHCb-2000-036, 2000 (unpublished).

[43] The LHCb Collaboration, *LHCb Muon Technical Design Report* (CERN, Geneva, 2001), CERN/LHCC 2001-010.

[44] The LHCb Collaboration, *Second Addendum to the LHCb Muon Technical Design Report* (CERN, Geneva, 2005), CERN/LHCC 2005-012.

[45] R. W. Forty and O. Schneider, CERN Report No. LHCb-98-040, 1998 (unpublished).

[46] R. Muresan, CERN Report No. LHCb-2007-121. CERN-LHCb-2007-121, 2007 (unpublished).

[47] The LHCb Collaboration, *LHCb Trigger Technical Design Report* (CERN, Geneva, 2003), CERN/LHCC 2003-031.

[48] M. van Beuzekom, A. V. Lysebetten, and B. Verlaat, Proceedings of Science (Vertex 2007) **009** (2007).

[49] A. Affolder *et al.*, Nucl. Instr. and Meth. A **583**, 18 (2007).

[50] S. Loecher and M. Schmelling, *The Beetle Reference Manual* (CERN, Geneva, 2006), LHCb-2005-015.

[51] R. Frei, *LV System: Design, Layout Implementation*, Presented at the VELO LV Checkout Meeting 25/03/2008, `http://indico.cern.ch/conferenceDisplay.py?confId=32339`.

[52] B. Rakotomiaramanana, C. Parkes, and L. Eklund, *Characterisation of the VELO High Voltage System* (CERN, Geneva, 2008), LHCb-2008-009.

[53] B. Rakotomiaramanana, C. Parkes, L. Eklund, and S. De Capua, *The VELO High Voltage System Control Software* (CERN, Geneva, 2008), LHCb-2008-009.

[54] M. Ferro-Luzzi, *The VELO Hardware Interlocks* (CERN, Geneva), EDMS Document, `https://edms.cern.ch/document/706629`.

[55] G. Haefeli *et al.*, Nucl. Instrum. Methods Phys. Res., A **560**, 494 (2006).

[56] G. Haefeli, *Contribution to the Development of the Acquisition Electronics for the LHCb Experiment*, PhD thesis, EPFL, Lausanne, 2004.

[57] T. Szumlak and C. Parkes, CERN Report No. LHCb-PUB-2009-006. CERN-LHCb-PUB-2009-006, 2010 (unpublished).

[58] K. Akiba, J. Borel, J. Buytaert, L. Eklund, and M. Gersabeck, *The algorithm for FIR corrections of the VELO analogue links and its performance* (CERN, Geneva, 2007), LHCb-2008-015.

[59] D. Jones, *Common Mode Correction Algorithms for the LHCb VELO* (CERN, Geneva, 2007), LHCb-2007-108.

[60] G. Haefeli and A. Gong, *LHCb VELO and ST Clusterization on TELL1* (CERN, Geneva), EDMS Document, `https://edms.cern.ch/document/690585`.

[61] T. Szumlak and C. Parkes, *Description of the VETRA Project and its Application for the VELO Detector* (CERN, Geneva, 2008), LHCb-2008-022.

[62] G. Barrand *et al.*, Comput. Phys. Commun. **140**, 45 (2001).

[63] N. Zaitsev, *Study of the LHCb Pile-up Trigger and B_s $J/\psi\phi$ decay* , PhD thesis, VU University, Amsterdam, 2000.

[64] M. Zupan and M. Ferro-Luzzi, CERN Report No. LHCb-2003-070, 2003 (unpublished).

[65] S. Viret, C. Parkes, and M. Gersabeck, Nucl.Instrum.Meth. **A596**, 157 (2008), 0807.5067.

[66] V. Blobel and C. Kleinwort, p. URL (2002), hep-ex/0208021.

[67] W. Baldini *et al.*, CERN Report No. LHCb-2006-035. CERN-LHCb-2006-035, 2006

(unpublished).

[68] O. Behrendt *et al.*, CERN Report No. LHCb-INT-2009-004. CERN-LHCb-INT-2009-004, 2009 (unpublished).

[69] R. Brun *et al.*, Proceedings AIHENP **96**, 81 (1997).

[70] S. Kwan, Nucl. Instrum. Methods Phys. Res., A **549**, 60 (2005).

[71] D. C. Christian *et al.*, Nucl. Instrum. Methods Phys. Res., A **549**, 165 (2005).

[72] S. Kwan, Nucl. Instrum. Methods Phys. Res., A **485**, 411 (2002).

[73] J. Wang, PoS(Vertex 2009) **037** (2009).

[74] A. Affolder, P. Allport, and C. G, Nucl. Instrum. Methods Phys. Res., A **604** (2009).

[75] A. Affolder, P. Allport, and C. G, IEEE Transactions on Nuclear Science **506** (2009).

[76] G. Casse *et al.*, *Characterisation of an Inhomogeniously Irradiated Microstrip Detector using a Fine Spot Infrared Laser* (CERN, Geneva, 2001), LHCb-2001-053.

[77] J. Borel, *The Analog Readout of the LHCb Vertex Detector and Study of the Measurement of the B_s Oscillation Frequency*, PhD thesis, EPFL-LPHE, Lausanne, 2008.

[78] LHCb Collaboration, R. Aaij *et al.*, Phys.Lett. **B694**, 209 (2010), 1009.2731.

[79] LHCb Collaboration, R. Aaij *et al.*, LHCb-CONF-2011-027 (2011).

[80] LHCb Collaboration, R. Aaij *et al.*, LHCb-CONF-2011-018 (2011).

[81] LHCb Collaboration, R. Aaij *et al.*, LHCb-CONF-2011-005 (2011).

[82] LHCb Collaboration, R. Aaij *et al.*, LHCb-CONF-2011-006 (2011).

[83] F. Lemeilleur *et al.*, Nuclear Physics B - Proceedings Supplements **32**, 415 (1993).

[84] M. Lozano *et al.*, Nuclear Science, IEEE Transactions on **52**, 1468 (2005).

[85] GEANT4, S. Agostinelli *et al.*, Nucl.Instrum.Meth. **A506**, 250 (2003).

[86] A. Papadelis, *Characterisation and Commissioning of the LHCb VELO detector*, PhD thesis, VU University, Amsterdam, 2009.

[87] S. Eidelman *et al.*, Phys. Let. B **592** (2004).